SENSOR-BASED COLLISION AVOIDANCE FOR INDUSTRIAL ROBOTIC ARMS

By

AMIN AHMADI BIDHENDI, B. ENG.

A Thesis Submitted to
the School of Graduate Studies, McMaster University
in Partial Fulfillment of the Requirements for the Degree
Master of Applied Sciences

MASTER OF APPLIED SCIENCES (2008) McMaster University

Mechanical Engineering Hamilton, Ontario

TITLE: Sensor-based Collision Avoidance for Industrial Robotic Arms

AUTHOR: Amin Ahmadi Bidhendi, B. Eng. (McMaster University)

SUPERVISOR: Professor Gary M. Bone

NUMBER OF PAGES: xii, 155

ABSTRACT

Robotic automation has evolved to be an irreplaceable part of production lines. Orderly operation of the robots is a key factor. Yet robots often have to deal with unpredictable factors including human beings or possible failures that lead to unexpected behaviours. Collision avoidance mechanisms are therefore of outmost importance to prevent injuries and damage. A major challenge in the creation of a dependable collision avoidance system is the sensory system that could cover relevant parts of the robot and capacitive sensors are a promising solution. The burden is to overcome the nonlinearity and other limitations of the capacitive sensors and harness their potential to this end. It is cumbersome to estimate the proximity of surfaces of the robot from its environment (which could include other robots) from the capacitive readings, so a novel sensing approach is proposed in this thesis. For industrial applications where the motions are well-defined, a pre-recorded capacitive signature can be used to monitor for unexpected changes. In this thesis the capacitive signature of one or more robotic arms will be used to predict and prevent collisions in a robotic workcell. A short training cycle is used to create a signature that is used at runtime to monitor the robot operation. Capacitive electrodes are placed on strategic locations on the robot arms and the surrounding environments and a supervisor computer uses the readings to cease the operation in case of any abnormality. This thesis describes the details of generating the signature from the training data and the runtime software. The supervisor computer provides a pause and/or go signal to the robot(s). The native controller of each arm is kept in place and the only change needed is the ability of each controller to pause the arm at command when a collision is detected and continue from this paused state. This approach requires minimum changes to the existing robotic equipments and programmes. These hardware requirements are widely available on existing controllers.

Signature creation is the process of finding the normal pattern of the capacitance readings from all sensors as well as some expected limits allowing for the variations that are to be expected. The algorithms, reasoning, and experimental data are provided throughout the text. The system is tested on a robotic workcell that includes an actively controlled robot and a passive revolute joint. While the algorithm is universal, the suggested hardware has been shown to provide sampling times of down to 20ms, and positional accuracies of ±2mm or better are achieved for the test setup. The thesis also proposes methods to expand the measurement hardware for increased protection and fault tolerance.

Acknowledgements

And here are the last lines of my seven year stay at McMaster, I don't know the what ifs of a different seven but I know that this paper, in its mighty length and with all its weaknesses would have not been the same, would have not been, if it was not for what I owe to the very many people that shaped the last 26 years. I am indebted to them all and that will not change. Most briefly, I will add their initials so I will remember but most sincere are my thanks to them for making it possible so enjoyably:
P.R., E.A.B., S.A.B., N.R., Z.L., C.G., the MSCP, the A.H.H., D.B., N.N., K.R., B.Sz., M.R.A., P.P., K.K., and many others.

It is fitting to acknowledge Professor Doctor Gary Bone, from whom I learned irreplaceable lessons in life, and I know better now. For the eye-opening experience, I will be grateful.

Table of Contents

LIST OF FIGURES

LIST OF TABLES

ABREVIATIONS

ADC	Analogue to Digital Converter
C-Space	Robot Configuration Space
CA	Collision Avoidance
CAD	Computer Aided Design
CAM	Computer Aided Manufacturing
CAPDAC	Capacitive Digital to Analogue Converter
CAS	Collision Avoidance System
CDC	Capacitance to Digital Converter
DAC	Digital to Analogue Converter
FEA	Finite Element Analysis
FEM	Finite Element Modelling
FSM	Finite State Machine
I^2C	Inter-Integrated Circuit
IO	Input/Output
IR	Infrared
LC	Inductor-Capacitor circuit
MoM	Method of Moments
MUX	Multiplexer
PCB	Printed Circuit Board
RC	Resistor-Capacitor
SRS	Supplementary Restraint System
WHAP	Whole Arm Proximity
USB	Universal Serial Bus

CHAPTER 1

Introduction

1.1 Preface

Robotic arms are an integrated part of the modern production line. They provide reliable and repeatable service for numerous tasks. For decades they have been taking on tasks whose tedious or risky nature makes them poorly suited for human labour. The price of this unquestioning willingness is a lack of adaptability. Without the complex sensory systems that human beings are born with, robots cannot be expected to conform to unknown situations. The conventional industrial robots offer limited or no protection against collisions. This makes the arms susceptible to serious damage and creates potential hazard for objects and personnel in their vicinity. With the integration of the robots into an ever-expanding number of areas, the need for effective collision avoidance systems is more and more evident. Whether a robot is autonomous, pre-programmed or tele-operated, efficient collision avoidance could guarantee safety and improve the efficiency. Arguably, this absence of a built-in collision avoidance feature could be largely attributed to the deficiencies of the existing sensory systems.

In industrial applications, space is of prime value and a shared robot work area could substantially reduce the need for space. Maximum efficiency may be reached with asynchronous and simultaneous operation of the robots sharing this work area [1]. It is

agreed by the concerned community that the major problem in a shared workspace is collision avoidance [2]. In shared work areas or workspaces, the pre-programming of the robots is the most common collision avoidance method. An elaborate offline preparatory process is required. A variety of integrated CAD software packages (e.g. DELMIA by Dassault Systemes) are designed to facilitate this task. This approach is reliant on the CAD model data of the robot and the environment. The offline nature of the method makes it unable to accommodate any changes during the operation. The alternative online CAD-based systems depend on the CAD modeling and real-time position information from the robots and other material handling equipment such as conveyer belts. With complete and up-to-date information, such systems are able to effectively protect the robot. The challenge in practice with all CAD-based systems is to maintain reliable CAD information. In particular, the hoses and cables create modeling inaccuracies. Minor modification to the arms, for example during maintenance, must be promptly reflected in the CAD model. In practice this is a rarity and leads to added risks.

A sensor-based approach to collision avoidance offers a higher degree of adaptability to a changing environment. The real-time nature of the sensor information makes them better suited for environments with uncertainties. It is also more suitable in dealing with the hardware failures or unexpected behaviour by the machinery. The most basic form of active collision avoidance is the "traffic light" approach [1]. In traffic light control, a robot does not enter a given area unless the area is vacated, and its presence in the area prevents the other machines from intrusion. Since these areas have to be much larger than the size of the robots, this approach leads to a less than optimal use of

assembly time and space [1] and limits simultaneous operations. The idea of this research is to overcome the need for this conservative approach.

Reliable sensor-based collision avoidance is a major challenge. To be effective, the collision avoidance system (CAS) must receive on-time information about the spatial placement of each and every part of the robot relative to its environment. A high degree of information integrity is expected of the sensory system and the system should be able to cope with the realities of a harsh industrial environment. The robot controllers must also be able to process this information and react in a timely fashion.

1.2 Statement of the Research Objective

The goal of this research is to provide a proof-of-concept for the use of the capacitive sensing in collision avoidance. The scope of this research work is limited to the industrial robotic arms operating in a predefined environment. By monitoring irregularities in the environment through capacitive sensing and providing predictive collision avoidance, the system aims to prevent collisions in a workcell containing multiple robotic arms. In line with the realities of most industrial robot controllers on the market a control rate of 50Hz is aimed for. The information available indicates that most industrial controllers have update rates of 20-50 Hz [3] [4] [5]. As it will be mentioned later, the proposed collision avoidance system controls the active robots by issuing a pause command to the robot controllers. Virtually all robot controllers provide an emergency stop capability. In many cases, the emergency stop is the quickest way to stop a moving robot as it activates the brakes and de-energises the drive system. However the use of emergency stop is not desirable in this application as it requires a more lengthy

restart. The intention here is to have an automatic recovery from the paused state while the emergency stop requires restarting of the cycle. As such, modifications to the software run on the controller have been made to truly accommodate the pause/go requests by the collision avoidance system.

1.3 Organisation of the Thesis

After this introductory chapter, the relevant literature is reviewed in Chapter 2. That includes the sensor technology and different proposed algorithms for collision avoidance. Chapter 3 presents an overview of the phenomenon of capacitance; and the capacitive measurement techniques and systems. In addition, the models for estimating capacitance are introduced in this chapter. In Chapter 4, the concept of a capacitive signature for an arm is introduced. It will be shown how a capacitive signature could serve as a virtually unique identifier of the environment and assist in collision avoidance. After that, the specifics of the sensor hardware are investigated in Chapter 5. This includes the data integrity and the design of the capacitive sensing electrodes. Chapter 6 discusses the statistical determination of the boundaries of the capacitive signature. Various approaches for determination of signature tolerances are examined and their effectiveness is analysed. Chapters 7 and 8 are on the runtime system and an overview of the experimental results, respectively. Chapter 9 summarises the achievements of this research and recommendation for future work.

CHAPTER 2

Literature Review

2.1 Introduction

Collision avoidance has been an active area of robotics research at least since the 1980s (e.g. [6]). While the focus of this thesis work is industrial robotic arms mounted on a fixed base, other areas are also reviewed. Interestingly, in the collision avoidance and collision detection research there is a substantial overlap with computer graphics, aerospace, virtual reality and solid modeling. This is stemmed from the common requirement to detect overlapping objects, be it for different purposes. It should be noted that although there could be inherent similarities between collision avoidance and collision detection, they are two distinct areas of work. To clarify, collision detection refers to a deterministic process to define whether two solid bodies are overlapping. On the other hand, collision avoidance refers to a broader field of preventing the collision which could include predictive and corrective actions [7]. Sensor-based collision avoidance is more specific to robotics applications. In many industrial applications, the workaround has been to confine the machines to predefined safe corridors [8]. For an autonomous robot without *a priori* knowledge of its environment, sensor-based collision avoidance becomes a requirement. In the interest of clarity, this review of the research work has been divided into two sections, sensor hardware; and path-planning and real-

time collision avoidance. The chapter concludes with a summary of the prior research and the concerns of this research.

2.2 Sensor Hardware

A variety of hardware ideas have been suggested and tested for collision avoidance proximity sensing. The most popular choices include ultrasound, infrared, inductive, capacitive, and vision systems. Some of the common methods and their basics of operation are described in this section.

2.2.1 Ultrasound Time-of-Flight

For a wave traveling at a known velocity, the time of travel is representative of the distance traveled. This is the foundation of a time-of-flight sensor. An ultrasound proximity sensor issues a sound pulse and measures the time it takes for the signal to reflect off the obstacle.

$$Distance = V_{sound} \times (T_{reception} - T_{transmit}) \quad (2.1)$$

Two advantages of the ultrasound systems are their insensitivity to the texture and the colour of the obstacle surface. On the other hand, the ultrasound systems are susceptible to the problem of multiple reflections and a limited resolution due to the long wavelength. In reality, most ultrasonic sensors cannot measure less than a few centimetres. At λ=42KHz (typical of an ultrasound sensor) the wavelength is ~8cm. A sound pulse could travel a multiple times and be detected resulting in an incorrect or incoherent measurement. The obstacles facing the sensor at sharp angles suffer from specular reflection. This phenomenon is depicted in Figure 2-1.

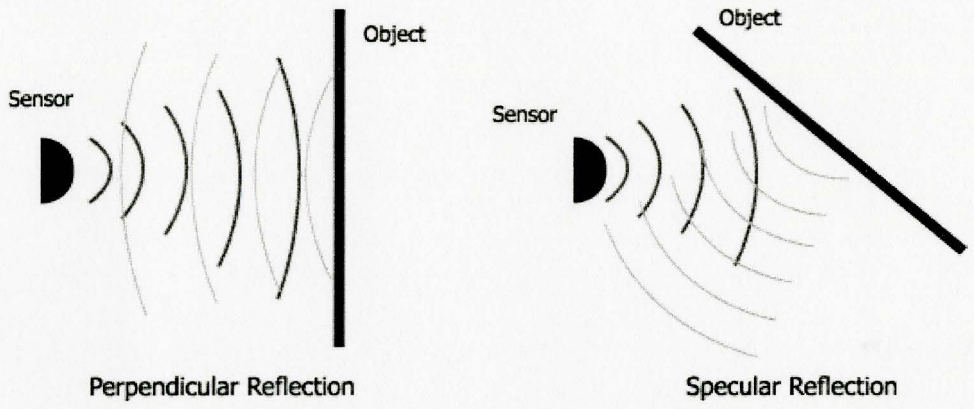

Figure 2-1: Example of the specular reflection

A problem faced by all proximity sensors based on a reflected signal is that the narrow field of view creates the blind spots. An object in the area between the sensors close to the body of the robot could be missed, resulting in blind spot. This is shown in Figure 2-2.

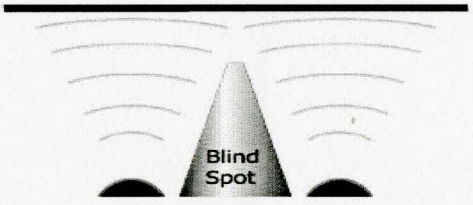

Figure 2-2: A case of reflected-signal sensors blind spots

Nakamura *et al.* [9] use sonar for a statistical mapping of the environment for a mobile robot. The team indicated that they used sensors that have a range of 0 to 250cm. Nevertheless, they did not report the type of the sensors or the manufacturer The sensors were claimed to have a 20° field of view That poses problems for a collision avoidance system because of large number of sensors required. To obtain the map the system obtains 30000 samples at training. This large number of samples is partly due to the sensor noise and the measurement uncertainties. There exists no mention of the length of time required for this acquisition or the number of samples needed at runtime. In their

search for a sensitive robot skin, Chueng and Lumelsky ruled out the use of sonar sensors due to the specular reflection issue and the blind spots or dead zones involved [10].

2.2.2 Infrared Sensor

Optical sensors have an established place in a variety of distance and proximity detection applications. The more common type operates in the infrared (IR) range. It is noteworthy that while the wavelength of infrared ranges from 1mm down to 750nm in comparison to the range of 750-450nm for the visible light, the wavelength is not the defining factor in the accuracy of the industrial grade sensors. The most common method to use in infrared sensors is triangulation. For a known transmitter/receiver geometry, the reception angle is indicative of the distance to the reflecting object. Figure 2-3 illustrates a sample geometry. The relationship the distance between the object and the angle φ is:

$$d_{object} = \frac{d_{base}}{2} \times \tan(\varphi) \qquad (2.2)$$

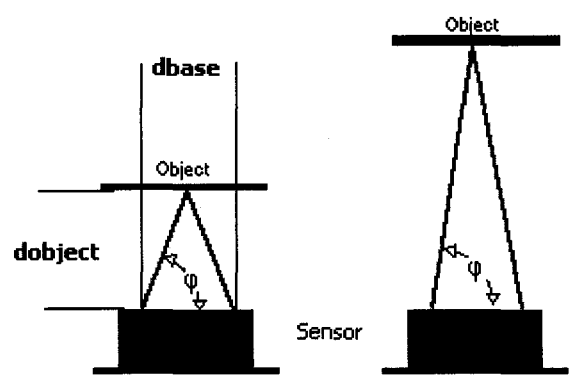

Figure 2-3: Triangulation in an infrared sensor

A major problem with infrared sensors is their dependency on a reflective surface. The texture and colour of the surface change the intensity of the reflected signal. Hence

certain objects are invisible to the sensor The specular reflection of mirror-like surfaces could also deceive the sensor or cause concealment.

In their design Cheung and Lumelsky used an infrared-based[1] sensor skin [10] They attempted to cover the body of the robot completely They deployed a "number" of sensor modules each containing 16 sensors. To process the raw sensor data a dedicated Motorola 68020[2] processor board was employed. They used 500 sensor pairs to partially cover the robot. The same authors used 475 individual sensors in [11]

Seraji *et al* [12] also used a commercially built infrared-based "Sensor Skin" on an RRC K-1207 robot. Figure 2-4 indicates the complexity and fragility of the setup.

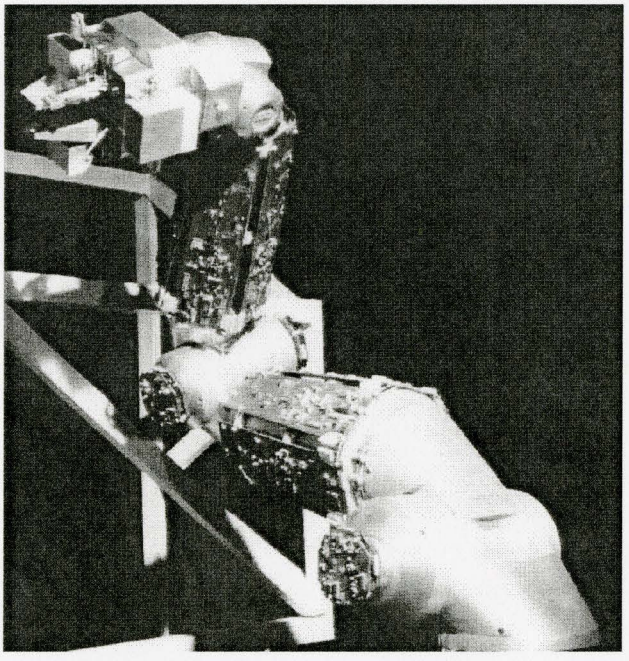

Figure 2-4: The sensor skin used by Seraji *et al.* [12]

The arm is guarded by 118 infrared detectors. The detectors are grouped into "Sensor Cells" each containing a microprocessor. The analogue circuitry is entirely

[1] Wavelength of 875nm
[2] A 32-bit processor

contained in the skin and the microprocessor interfaces with the main controller through a multi-node serial network[1]. This distributed processing is needed to bring the wiring to a manageable level and free the main processor for the main collision avoidance algorithm. The authors admit that the link is limited to 32x32 sensor cells. That is not considering the processing power requirements or the growth of the software complexity. The data delivery limits the extension of the system.

Gandhi and Cervera [13] used infrared sensor rings to cover the body of their Mitsubishi PA-10 arm. To provide a complete 360° coverage, each ring ought to house 10 sensors. To handle the data, each ring is managed by two microcontrollers[2] networked through an I^2C[3] bus to the main processor. The authors do not explicitly state the viewing angle of the rings however it appears that more than one ring is necessary to protect the entire length of an arm. Furthermore, although hardware is scalable to more than hundred sensors, they admit that the state-space of their learning process grows exponentially making this approach "unfeasible" for a large number of sensors.

2.2.3 Vision Systems

Machine vision systems provide another alternative for collision avoidance. Theoretically, an array of cameras with a clear view of the workcell could provide complete and real-time information about any robot or obstacle present. Although the captured image could contain all the information needed, the main challenge is extraction of relevant information. Machine vision is a broad field and as such a comprehensive

[1] EIA-485 also known as RS-485
[2] Microchip PIC18C252
[3] Inter-Integrated Circuit Bus also know as I^2C. Developed by Phillips Electronics, it is a master-slave serial network

review is outside the scope of this thesis. Nonetheless, a subset of the works directly related to collision avoidance or with beneficial implications is hereby examined.

Heng *et al.* [14] presented a case for the need for secondary system when machine vision is in use for mobile robots. Their active sensor fusion system uses a combination of vision and ultrasound to navigate successfully. They used an expansion rate factor with the vision system for depth detection (*i.e.* obstacle distance). If the size of the object grows rapidly, it indicates a closer obstacle. This method is only possible because the speed of the mobile robot is known and the object is assumed to be nearly stationary. Depth detection using machine vision generally requires more than one camera, which adds to the total system cost and complexity. All systems using fixed cameras risk obstruction by the moving objects including the robots themselves.

Norikawa *et al.* [15] deployed an "eye-on-the-hand" to create a CAS. The arm-mounted camera always has the arm in sight as shown in Figure 2-5. This also eliminates the need to coordinate the different frames. For this system to function predictably the obstacles must be further than 30cm from the camera. They state that closer objects could lead to "radical and dangerous" motions.

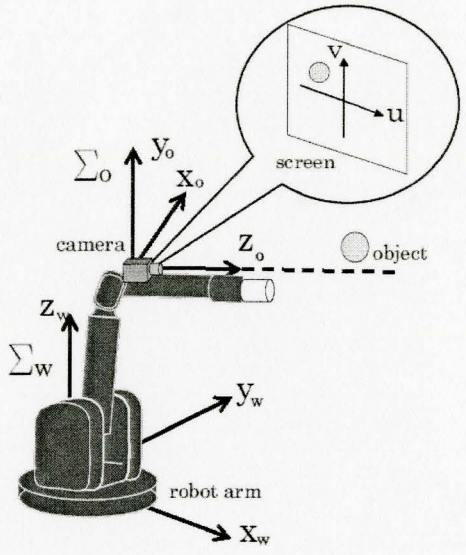

Figure 2-5: Eye-on-the-hand as proposed by Norikawa *et al.* [15]

2.2.4 Inductance

Inductance measurement is yet another option for proximity detection. Jagiella and Fericean [16] provide an overview of some of the available inductance-based sensors. Similar to the other systems discussed here, the inductive systems offer the advantage of non-contact detection. They also provide immunity to moisture and oil in the space between the sensor and the object. That is a clear advantage to other methods hereby discussed. Although capacitive sensors are also insensitive to surface quality of the electrodes, the quality of the dielectric between the two plates is a factor The authors claim that in comparison with capacitive sensors, inductive sensors have superior temperature robustness. Inductive sensors have proven themselves in harshest environments however their use in collision avoidance is limited. Naturally, they are only applicable for metallic objects. Most commercially available sensors are tuned for small

ranges of few centimetres. The average industrial robot has decimetre stopping distance and so there sensor cannot be used in a CAS.

2.2.5 Capacitance

Like inductive sensors, capacitive sensors use the electromagnetic field for the proximity determination. Capacitor sensors have a wide sense-angle and can cover a large area with a single sensor. They can also be used for non-conductive materials. These sensors provide the basis for very fast measurement rates. In another field of research, Novak and Wiczer demonstrated its use for surface finish scanning [17]. Novak and Feddema [18] implemented sensor hardware that measures up to 40cm for conductive and non-conductive objects. Novak and Feddema [18] and Ma [19] state that the measurement, unlike that of the reflection-based sensors, is instantaneous. Although this assertion is fundamentally true, the most common measurement technique is impedance identification by using an AC signal. As such, the frequency of the signal is a limiting factor. Any additional filtering or acquisition time would further elongate the process. A sound pulse can travel a 50cm distance in 2ms[1] which compares favourably with the measurement times of commercially available capacitance measurement circuitries. A major advantage of capacitive sensors is their inherent insensitivity to the colour and the texture of the object. Moreover, the angle of approach does not lead to concealment although a different distance might be reported.

Novak and Feddema define two classes for the capacitive sensors based on whether the obstacle is a plate of the capacitor or not. The first type, noted as the most

[1] With the approximate speed of 344m/s

common, uses a single plate, with the other side a grounded object. They acknowledge that such a setup is prone to parasitic capacitances to ground and requires corrective measures such as active shielding. As defined by the authors, the second type is when both capacitor plates are nearby and the obstacle is part of the dielectric[1]. The sensor developed by the team is of the second type. Both plates of the capacitor are on a single substrate. The setup shown in Figure 2-6 is the basic setup of the sensor. The charge amplifier captures the leakage from the oscillator through the "capacitors". The amplitude of the signal at the second plate (labelled 2) is indicative of the capacitance between the two plates. This capacitance is influenced by the distances involved and the effect of the obstacle on the electric field. The obstacle is conductive in this setup.

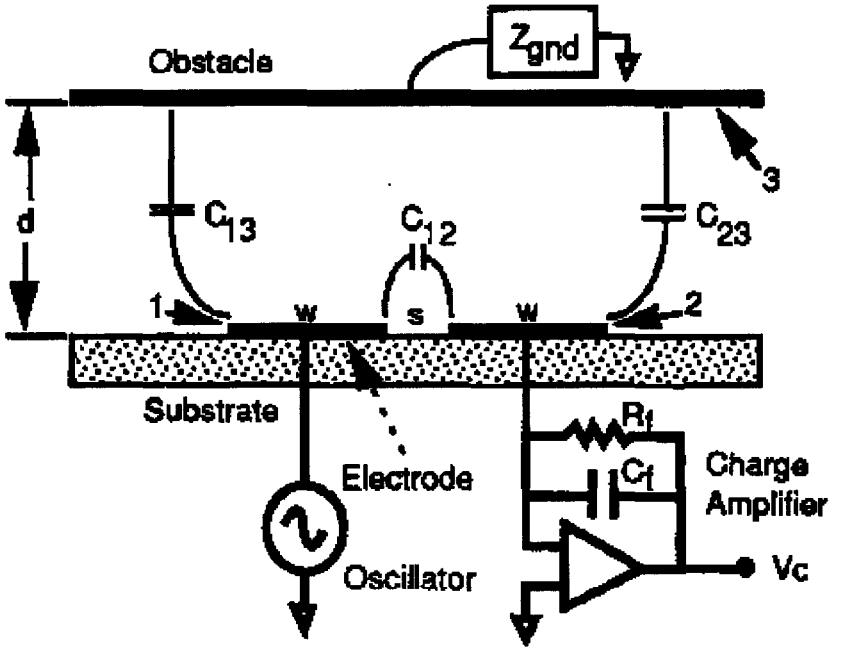

Figure 2-6: The schematic of the circuit used in [18]

The capacitance between the two plates is defined by

[1] Arguably a conductive obstacle acts to disturb the naturally occurring fields

$$C_{measured} = C_{12} \parallel (C_{13} + C_{23}) = C_{12} + \frac{1}{\frac{1}{C_{13}} + \frac{1}{C_{23}}} \quad (2.3)$$

where C_{13} and C_{23} are in series varying with the distance d; and C_{12} is constant .

Novak and Feddema only published the results for grounded conductive obstacles. A metallic robotic arm can be considered such an obstacle. They modelled two 15mm electrodes with the distances S and d as shown in Figure 2-6. In their simulation and analytical work, a 2-D case was considered. Behaviourally, such an arrangement is similar to infinite depth into the page. The authors used an FEA model run on the COSMOS/M v1.61 software to calculate the expected capacitances. Figure 2-7 indicates the expected results for the changing distance (d) from the sensor to a flat conductive obstacle for different sensor gaps (S). A smaller electrode trace-to-trace gap produces larger results yet with the obstacles farther than 125mm, the slopes of the four lines are similar.

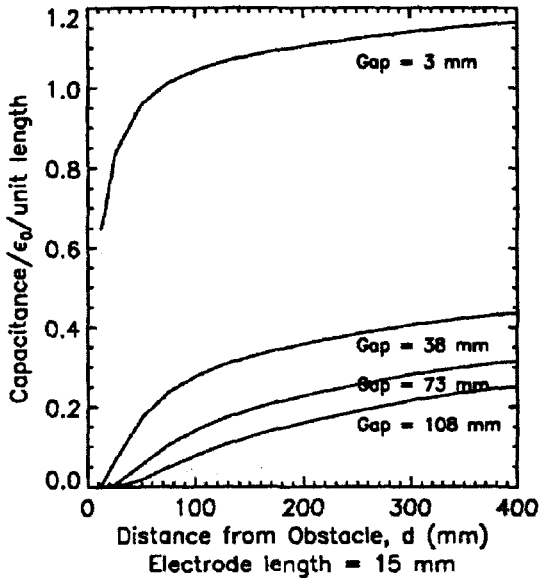

Figure 2-7: Simulation result for different gaps for a conductive flat surface [18].

The authors assessed their setup by using an etched electrode array on a three layer PCB[1]. The topmost layer accommodates the electrodes with the traces 15mm wide and 3mm apart. They also used dual frequency modulations. Each physical contact or trace is connected to two filters tuned to the different frequencies[2]. Their circuit design is shown in Figure 2-8. They state that the stacked arrangement enables them to have 8 sensors with 3mm gap or 4 sensors with 2, 38, 74 or 108mm gaps. It appears that the assumption has been made that when larger gaps are being tested the traces in between the two active traces do not influence the results. The oscillators are connected to the connections labelled *f1* and *f2*. *CA* indicates the *Charge Amplifiers* while SD is the filtering *Synchronous Detection* circuit[3] or the filter. The signal output of each trace is available at the corresponding V_{ox} output and it is digitised at this point. With the synchronous detection gain set to 80, V_o is

$$V_o = \frac{C_{12} + C_{pcb}}{C_f} \times 80 \qquad (2.4)$$

where C_{PCB} is the capacitance through the PCB and C_f is the feedback capacitor of the charge amplifier as shown in Figure 2-6.

[1] Printed Circuit Board
[2] Novak and Feddema use modulation at 100 and 153 KHz.
[3] Achieved through phase-locking

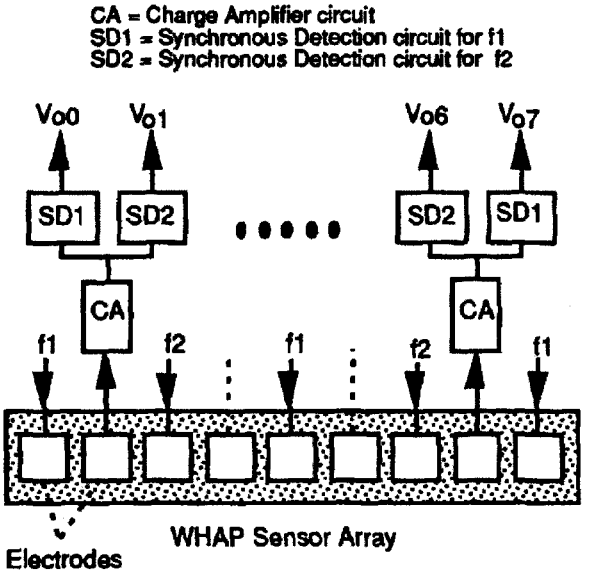

Figure 2-8: Array geometry and connections [18]

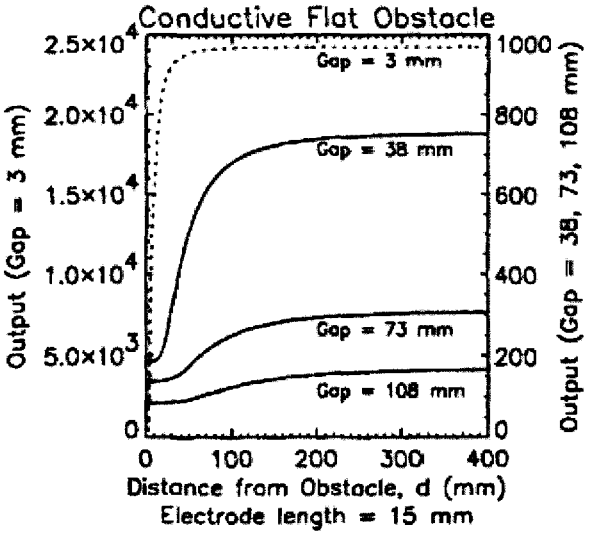

Figure 2-9: Experimental results for four different gaps [18]

Their experimental results for a flat conductive obstacle are shown in Figure 2-9. They state that beyond 40cm, the signal is lost in the noise. This maximum working distance was found not to be a function of the gap size. The team conducted similar tests for a 350x350mm concrete block. The results appear to have a similar profile with one quarter of the sensitivity. The authors assert that a smaller gap provides higher sensitivity

while sensors with larger gap would perform better with the smaller obstacles. The stated reasoning is the larger electric field; nonetheless they reported no result confirming this. They stated that their setup is insensitive to the parasitic capacitance to ground by design. This fact will be examined in Chapter 3.

The invisible and passive nature of a capacitive sensor makes it of use in other types of collision avoidance applications. Karlsson and Järrhed [20] provided an example for human detection in a robotic workcell. The roof is one plate of the capacitor and the floor is the other. A human intrusion into the space would change the capacitance and trigger an action. Unlike vision systems, this is independent of the person's attire.

2.3 Path Planning and Real-time Collision Avoidance

The focus of this research is correctly responding to the changes in the workcell. In this work, the intention is to respond to these changes based on the real-time sensor input. Lee and Chien [8] analysed the various approaches to time-varying obstacle avoidance. They categorised obstacle-conscious motion planning into four groups, heuristic online (HON), heuristic offline (HOF), analytic online (AON) and analytic offline (AOF). They stress that, the HOF approach to collision avoidance benefits from human intelligence at the design stage while they admit no "general" heuristic method could exist. A primitive method offered by the team is to visualise the basic path on a computer screen and iteratively modify the path to satisfaction. The second approach, HON, uses an online database of trajectories and geometries to predict or detect a collision. In general such an approach is only effective against collisions with known objects. The other approach is AON. As suggested by the name, the methodology is to

find an analytical solution to the path-planning problem during operation. This shifts the focus from design criteria assumptions to the real-time data. Their very broad analysis did not consider the nature or the source of the runtime data. The last class is AOF. The basic advantage of AOF over AON is the freedom from the time constraints. That creates the possibility for more detailed modeling. Once again the offline nature makes it unable to accommodate real-time changes. They also discussed the constraints for both online and offline approaches, including time, priority (who proceeds first), path, clearance, smoothness, and torque constraints.

Roach and Boaz [2] presented a time-space planning procedure for the coordination of two arms in a shared work environment. They proposed a supervisory algorithm which consists of two layers. The top layer determines the motion steps for the job and the global "interdependency" of the motions. The second layer performs spatial planning, local clearance checking, and path determination. The experimental setup used by Roach and Boaz was two 6-DOF robots on a worktable and the algorithm was designed for "sparsely obstructed" environments. When a collision is suspected, a repulsive point is inserted. This action is based on the assumption that a "reflexive" move would bring the arm into clearance away from the other robot. For more optimal results, the algorithm checks for physical overlaps at the planning stage. If a collision is predicted, delays are inserted to avert the situation. If a collision is bound to happen in the middle of the upcoming move, it was argued that mere alteration of the path would prevent the collision. If a potential collision is foreseen at the beginning or the end of the upcoming move, further action is taken. As mentioned, the proposed resolution is to

move the arm towards its base and consequently away from the intruding partner. The timing for the robots could also be modified to ensure the safe departure of the first robot. Their algorithm is very specific to the environment, in particular because of the assumption that moving towards a robot's base avoids collision.

Cheung and Lumelsky reduced the path-planning problem to a local obstacle-conscious planning [21]. Their design is based on the infrared Sensor Skin described previously. The information extracted from each sensor is a local tangent to the point of "contact"[1]. This is to avoid collision while not losing "contact" with obstacle. By following a tangent to the obstacle, the robot is to trace around the object and eventually clear it while inching towards the endpoint. Once the trajectory line is met again, the robot would continue on its original path. This requires minimum alteration of the overall path however it is time-inefficient. A model of the robot path in 2-D space is depicted in Figure 2-10 below. The detection of the obstacle forces the robot to follow the tangent. The step planning and tangent tracing is done in C-space and therefore obstacles approaching the robot body or the end-effector are handled in a similar manner. The method however fails to address multiple obstacles affecting the different parts of the robot.

[1] Defined as the closest object observed with no actual physical contact

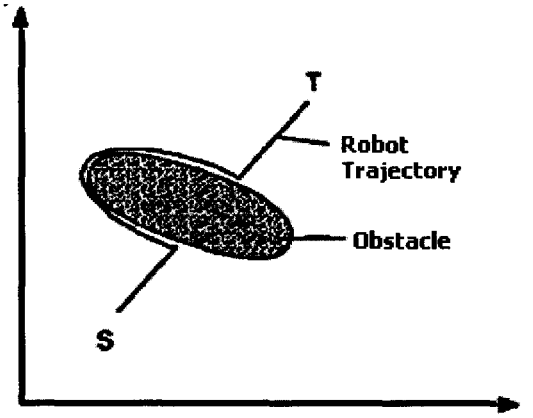

Figure 2-10: A robot trace around the obstacle in 2-D [21]

Their method also does not always lead to a solution without iterations. The case shown in Figure 2-11 below presented by the same authors in [11] is an example. In travelling from S to T, the method does not converge

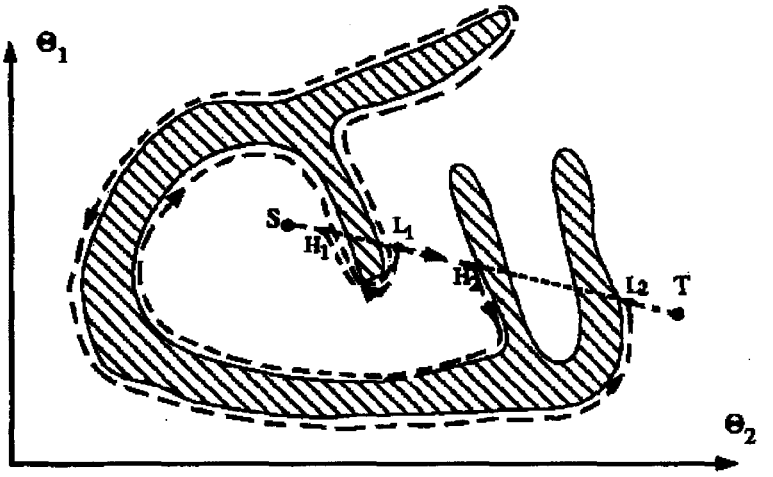

Figure 2-11: A non-converging case in [11]

Boddy and Stobart [22] proposed a hierarchical control scheme for use in unstructured environments similar to those discussed in this thesis. The intention of their work, as a part of a general architecture, was to enable safe operation of the machinery with only an approximate representation of the external world. The control structure has been segmented into three layers, a high-level goal/task interpreter, a tactical layer for

trajectory planning and the lowest level of the hierarchy, the executive layer. The higher level converts the commands into a series of achievable motions. The tactical layer is where the input from the sensory system is considered. In this layer conversion to actuator specific coordinate and path profiling are performed. The last layer is a closed loop drive system. The sensor hardware is to be a proximity or range sensor that covers the vital parts. The objective of the tactical layer is to modify the elements of the strategic plan to accommodate the perceived changes in the environment. New "safety" points are inserted between the endpoints set by the strategic layers. Each sensor generates a repulsion vector from the obstacle in its vicinity. The approach of the obstacle determines the magnitude. The repulsion vectors define the safety points. The system was developed for a PUMA 562 robot arm without the native VAL II controller in charge. The team equipped the arm with an array of ultrasonic sensors to provide proximity and range information. This method is fundamentally designed for protection of the end-effector and therefore provides no guarantee for the body of the arm. As well, bypassing of the native controller makes this approach less applicable to the industrial cases where the use of the native controller is desired.

Novak and Feddema [23] expanded their work on whole-arm capacitive sensing by proposing a control algorithm based on the repulsive force by exploiting the extra degrees of freedom available. Geared towards tele-operated applications, they aimed to ensure whole-body safety. In a tele-operated applications the end-effector is to obey the operator as closely as possible without putting its own or the cargo's[1] safety in jeopardy.

[1] Novak and Feddema's work was focused on hazardous waste handling

This is achieved by adding a "collision avoidance filter" between the command interpreter and the robot controller. The basic idea is to linearly scale the speed at the contact point to zero when an obstacle is detected:

$$Z_{if} = \frac{z_{ir}}{d_{max} - d_{min}}(d_i - d_{\min}) \tag{2.5}$$

where Z_{if} is the applied perpendicular velocity and Z_{ir} is the commanded perpendicular velocity at the point of contact for the i_{th} obstacle. The following figure further clarifies the relationship.

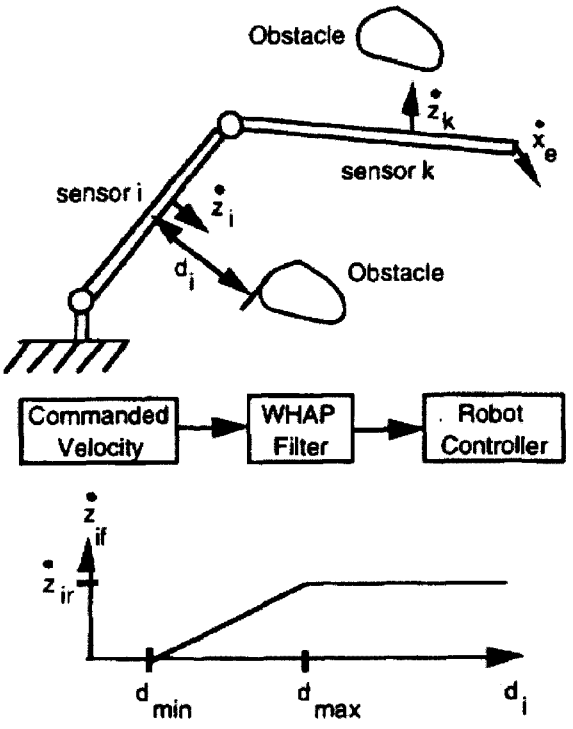

Figure 2-12: Overview of the scheme in [23]

However the placement of the filter between the operator and the motion controller detaches the operator from the actual motion. That is to say, when the system pre-emptively changes the robot's course, the operator can feel "out of control". This could also lead to an over-reaction by the operator. This is more exaggerated in the

circumstances in which the operator is not able to see the entire body of the robot and therefore does not expect the observed "disobedience". If the repulsive force leads to the movement of the robot when no movement at all is demanded by the operators, further unease is caused. The authors acknowledge this problem and propose the solution of stopping the robot stop even away from its equilibrium if no motion is requested.

For the case of a robot performing a pick-and-place task, the start and end points are of primary interest. In many other instances of industrial applications and beyond, the end-effector path is also crucial. A classic example is a welding robot. In these circumstances, an arm with redundant degrees of freedom could maintain the path while avoiding obstacles. Xie *et al.* [24] provide a theoretical solution to the problem by modeling the obstacles and other restrictions as joint impedances. With their model, the proximity sensor information (*i.e.* obstacles), the angle and torque limits of the joints, other external forces as well as singularity avoidance factor are modelled as impedances. The redundancy is resolved by minimising a desired cost function. The dynamics of the rigid robot could be written as:

$$\tau = M\ddot{\theta} + V(\theta, \dot{\theta}) + G(\theta) + J^T F_e \tag{2.6}$$

where τ is the robot joint torques and F_e is the force vector experienced by the end-effector, M is the mass matrix of the robot, $V(\theta, \dot{\theta})$ encompasses the centrifugal and Coriolis , $G(\theta)$ the gravity term and J is the Jacobian matrix of the arm. Points on the arm near obstacles are assigned artificial "collision forces" that would deflect the point from the obstacle. The total collision avoidance torque is made of

$$\tau_{CA} = \tau_{SC} + \tau_{JL} + \tau_{OBS} \tag{2.7}$$

where τ_{SC}, τ_{JL}, and τ_{OBS} are respectively he singularity avoidance, joint limit and obstacle avoidances torque elements. The influence of obstacle avoidance factor is dependent on its proximity The obstacle is only noticed when it is closer than R_{SOI} in Figure 2-13 The control torque was given by

$$\tau_c = M\ddot{\theta}^d + V(\theta, \dot{\theta}) + G(\theta) + J^T F_e - \tau_{CA} \tag{2.8}$$

Where $\ddot{\theta}^d$ is the vector of desired joint accelerations.

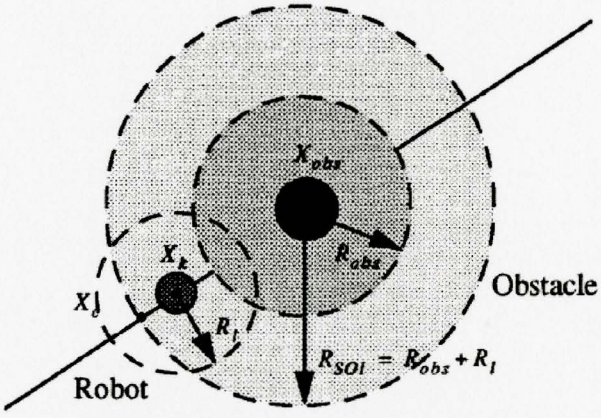

Figure 2-13: Three obstacle proximity zones in [24]

Xie *et al.* provide an all-encompassing solution however once again it is dependent on more information that available in many industrial cases. There is need for both joint torque sensing and control. However, in most cases, robot controllers are position-controlled. They also assumed that the proximity of the obstacle was either known or sensed online. It should also be noted that redundant degrees of freedom increase the overall cost of the system.

Seraji *et al.* [12] proposed an alternative approach to the basic repulsive force idea. If the proximity of the arm to the obstacle is to be presented as a virtual spring-damper mechanism, a force control algorithm should adequately prevent the robot from

colliding with obstacles. This representation enables collision avoidance work to benefit from the great body of work in force control. Once again, the obstacle in only considered when closer than a certain threshold.

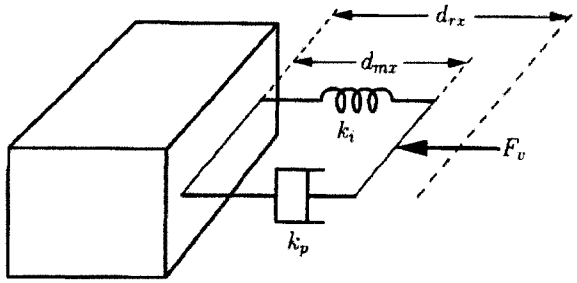

Figure 2-14: Virtual spring visualisation [12]

It needs to be clarified that this method requires strictly directional proximity sensors. They used a 3-axis IR detector at the end-effector (X,Y,Z). The body of the robot was covered with the IR "sensor skin". The large number of measurements requires a high bandwidth connection between the robot and the processing unit.

2.4 Summary

The review of the literature available in the collision avoidance field makes it evident that no single solution is available for the problem at hand. While a variety of sensor hardware is available for proximity detection, the choice is particular to the application. The ultrasound and infrared sensors provide a precise and focused measure of the distances and are relatively insensitive to the obstacle material. Yet their limited field-of- view necessitates large numbers of sensors which may lead to data processing and installation complexities. They are also sensitive to the reflective properties of the obstacle surfaces. The ultrasonic systems also fail to detect smaller objects as they depend on the surface size for the reflection. Inductive sensors are of limited use in the

collision avoidance work due to their limited range and angle; and their insensitivity to non-metalic objects.

The vision systems provide a promising research avenue but they suffer from many practical limitations. Many algorithms require marking points or distinct colours for the workcell elements or the potential obstacles severely limiting their applicability. They also suffer from image distortion by the lens or the image sensor or dirt in the air. It is fundamental for a vision system to have a clear view of all the objects of interest and therefore no occlusions can be tolerated. This incapacitates such systems in typical cluttered industrial environment. Most works reviewed agree that the computational costs of the visions systems also pose a major challenge. The large volume of data to be processed generally limits the real-time application of these systems. In cases where dedicated high-speed hardware has been developed, the real-time requirement can be met but only limited functionality is available and the system is inflexible.

The capacitive sensors offer an encouraging method for the applications in which wide sense-angle is acceptable. As the literature has shown, they are sensitive to both conductive and insulating materials and are relatively unaffected by the cluttering of the space between the sensor and the obstacles. Capacitive sensors are nonlinear in nature and have limited use for absolute measurements. Yet they provide a valuable measure of the environment and wide-angle information.

While path altering collision avoidance is invaluable in self-navigating robot applications and in cases where autonomy is acceptable, it could be detrimental in industrial work where predictability is vital. In the production applications the collision

avoidance is more focused on protection and not path finding. It was generally seen that the added flexibility results in reduced speed that is ill-afforded on a production line. It has also been seen that in all cases where an autonomous behaviour was proposed the industrial grade controller had to be bypassed. This shift in equipment creates major practical issues. The absence of a familiar proven controller limits the attractiveness of the solution for many potential users. By keeping the existing controller in use, the existing expertise of the professionals in the field can be exploited. It is also of high value to create a system that could function as an add-on to an existing system with no need for substantial changes to the existing equipments and programmes.

CHAPTER 3

Capacitance and Capacitance Measurement

3.1 Introduction

The collision avoidance system proposed in this thesis is based on the capacitance measured between electrodes installed on the robots being controlled. It is therefore appropriate to introduce the physics of capacitance in this chapter. The analysis of the capacitance values is important for validating the experimental apparatus and sizing the electrodes as discussed further in Chapter 6. At first an analytical overview is presented. Subsequently three models are introduced for estimating the capacitance for a given geometry. They are the basic parallel-plate capacitor, the method of moments specifically tailored for this application [19], and a model for non-parallel plates by Xiang [25]. The two last models are attempts to overcome the deficiencies of the parallel-plate model. Next, an examination of the most common methods to measure capacitance, various circuit topologies, and the hardware options along with the particular characteristics of the setup used in this thesis. Experimental results and their comparison with the theoretical values are also presented. It is worth mentioning that for this proximity sensing application, the capacitances involved are all of the quasi-static case due to the relatively slow speed of the robot compared to the excitation frequency involved [19].

3.2 Capacitance

Capacitance is defined as the capacity of a system to store electric charge for a given electrical potential difference [26] For two plates containing $+Q$ and $-Q$ of charge as shown in Figure 3-1, the capacitance is found to be:

$$C = \frac{Q}{V} \tag{3.1}$$

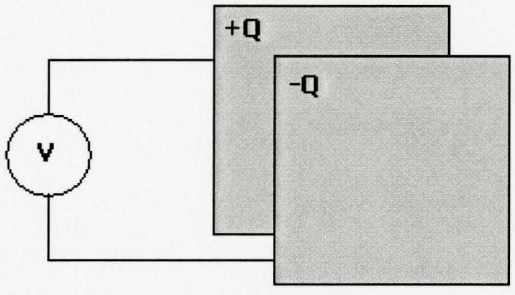

Figure 3-1: Two-plated capacitor

The SI unit for the parameter is Farads. 1 Farad is one Coulomb of charge per 1 Volt. To evaluate the capacitance analytically, both the voltage,V, and the charge density, Q, must be quantified. The voltage, or electrical potential difference, between the two plates is, by definition, the work required to transport a charge of[1] $q_+$from the lower potential point to the point with higher potential.

$$dV = \frac{dw}{q_+} \tag{3.2}$$

The work done is by definition.

$$dw = \vec{F}\ dl \tag{3.3}$$

[1] A positively charged particle q is considered, however the analysis is general by nature and applies irrespective of the actual charge.

The force field is a result of the electric field. Hence the external driving force on the unit charge could be explained as:

$$\vec{F} = -q_+ . \vec{E} \tag{3.4}$$

therefore the incremental voltage change dV along the path dl could be written as:

$$dV = -\frac{q_+ . \vec{E}}{q_+} . dl = -\vec{E} . dl \tag{3.5}$$

The total voltage difference between the two points p_1 and p_2 on the two opposing planes of the capacitors adds to:

$$V_C = V_{p_2 - p_1} = \int_{p_1}^{p_2} -\vec{E} . dl = V_{p_2} - V_{p_1} \tag{3.6}$$

From the Maxwell's Equations in electrostatic form:

$$\nabla . \vec{D} = \rho_v \tag{3.7}$$

$$\nabla \times \vec{E} = 0 \tag{3.8}$$

where

$\vec{D}$ is the electric flux density,

ρ_v is the volume charge density,

$\vec{E}$ is the electric field intensity and,

∇ is the gradient operator.

the charge Q in Equation (3.1) is:

$$Q = \int_v \rho_v \, dv = \int_v \nabla . \vec{D} \, dv \tag{3.9}$$

where v is an arbitrary volume containing one of the plates. Gauss' theorem guarantees that Equation (3.9) could be reduced to a surface integral of the form:

$$Q = \int_s \vec{D} \,.\, d\vec{s} \tag{3.10}$$

Knowing that [26],

$$\vec{D} = \varepsilon \vec{E} \tag{3.11}$$

where ε is the permittivity of the medium, Equation (3.10) reduces to:

$$Q = \int_s \varepsilon \vec{E} \,.\, d\vec{s} \tag{3.12}$$

Equation (3.13) establishes the relation between the charge on the plate and the resulting electric field. Using Equations (3.6) and (3.12) the capacitance is:

$$C = \frac{Q}{V} = \frac{\int_s \varepsilon \vec{E} \,.\, d\vec{s}}{\int_{p_1}^{p_2} -\vec{E} \,.\, dl} \tag{3.13}$$

3.3 The Parallel-Plate Capacitor

In their most basic form, capacitors are modeled as two parallel plates with a dielectric medium in between. Equation (3.13) could be greatly simplified if the field in between the plates in uniform. For two infinitely large plates positioned in parallel, the electric field is bound to be uniform and perpendicular to the surface of the plates to attain its symmetry. By ignoring the field fringing effect near the edges the assumption may be extended to large plates with small separation as in Figure 3-2[1].

[1] Throughout this document, electric field is assumed to extend from positive to negative

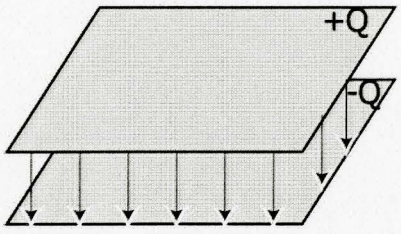

Figure 3-2: Electric field in the parallel-plate capacitor

For a uniformly distributed charge on the plate, the charge density is found to be:

$$\rho = \frac{Q}{A} \tag{3.14}$$

In the absence of any fringing effect, the field only has a normal component to the surface of the planes, $\vec{N}$ Therefore, the electric field $\vec{E}$ could be described as:

$$\vec{E} = \vec{N}\frac{\rho}{\varepsilon} \tag{3.15}$$

where ε is the permittivity of the dielectric. Substituting Equation (3 15) in Equation (3.6) yields:

$$V_C = -\int_{p_1}^{p_2} \vec{N}\frac{\rho}{\varepsilon}\ d\vec{l} \tag{3.16}$$

where $d\vec{l}$ is the incremental step normal to the planes and collinear with $\vec{N}$ The uniformity of the field allows further reduction of the integral to:

$$V_C = \vec{E}\ \vec{d} \qquad (a\ scalar) \tag{3.17}$$

By substituting and rearranging Equations (3 14) and (3 15), the relation between Q and E reduces to:

$$Q = \varepsilon EA \tag{3.18}$$

Therefore the capacitance is.

$$C = \frac{\varepsilon EA}{Ed} = \varepsilon\frac{A}{d} \tag{3.19}$$

To reiterate, the preceding relationship states that when the fringing effect is negligible, the capacitance between two parallel plates is the ratio of area to the distance between the two plates multiplied by the permittivity of the dielectric separating them. Regardless of the geometry involved, Equations (3.13) and (3.19) clearly indicate that the capacitance is proportional to the permittivity of the medium. Hence this factor is also important to this research due to the impact of the environmental conditions on the constant. This issue will be discussed in Section 5.7. The influence of the fringing fields has a major impact on the results as the distance is increased. This fact is discussed next.

3.4 Parallel-plate Capacitor with a Large Separation

The pivotal assumption in the analysis offered in Section 3.3 is a sufficiently small gap such that the fringing effect could be neglected. As this assumption is more and more violated by increasing the gap, the errors increase. In proximity sensing for collision avoidance applications the distances between electrodes are most often larger than the size of the electrodes used. As such, more accurate models are required to estimate the capacitance between the electrodes.

Ma [19] exploited the method of moments, (MoM), to numerically calculate Equation (3.13) for the case of a capacitor with 50x50cm plates. The distance between the plates is varied and the result is compared against the estimation provided by Equation (3.19). Figure 3-3 is the ratio of the results of the MoM to the parallel-plate approximation for distances of zero to 2m. The horizontal axis is the ratio of the distance to double the area. For his area of $0.25m^2$, ratio of 4 indicates a distance of 2 m.

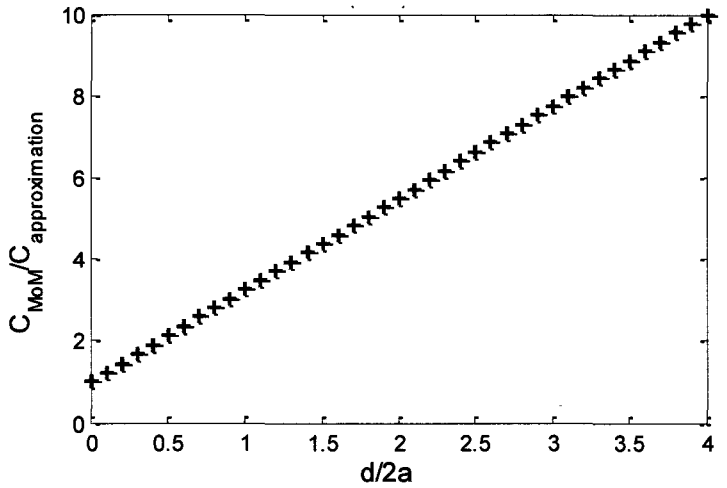

Figure 3-3: Ratio of MoM simulation to parallel-plate approximation for changing gap [19]

Figure 3-3 clearly shows that at the end of the simulation range the approximation formula (3.19) results in a value 10 times smaller than the value found by the simulation. It should be recalled that most practical electrodes for proximity sensing are generally smaller than 50x50cm while the distances are in this range. In his work, Ma shows the cause of this significant deviation. Figure 3-4 is the simulated field profile across an edge of one of the plates.

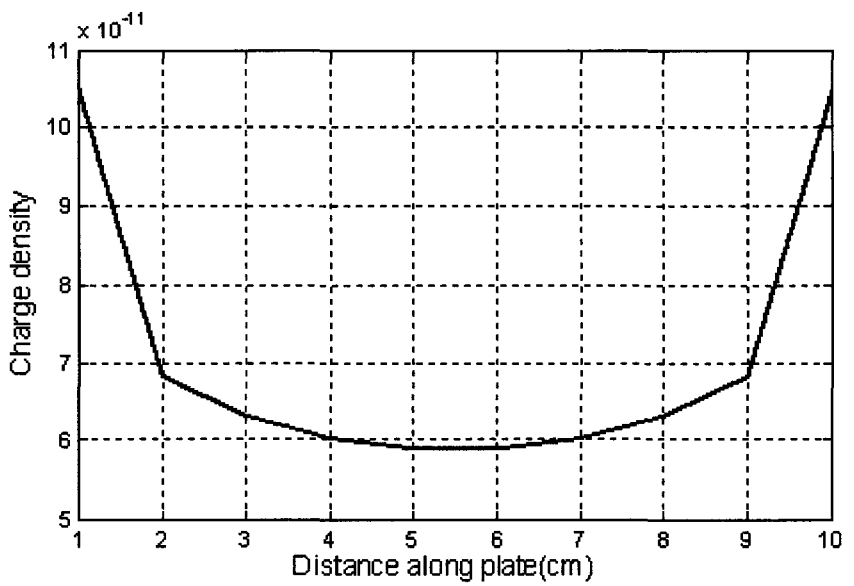

Figure 3-4: Charge density along the edge of the plate

As the plates separate further, the uniformity of the field is lost and the fringing effect has a greater influence. It should be recalled that an assumption of the parallel-plate approximation is that the field is uniform. Hence any use of the parallel-plate approximation should be approached with caution and in most cases is only a rough approximation.

3.5 Capacitance of Inclined-plate Capacitors

It is unlikely that in proximity sensing for collision avoidance applications the two plates would be parallel at all times. The inclined plate arrangement violates all the assumptions of the parallel-plate simplification. Xiang derived a set of equations the capacitance of two inclines plates for the 2-D case [25]. In his analysis only the width of the plates are considered. Therefore the capacitance is found per unit length and the plates are assumed to be of infinite length. The visual representation of the case is illustrated in Figure 3-5. Points A and B are the edges of Plate 1 and Points C and D are the edges of Plate 2.

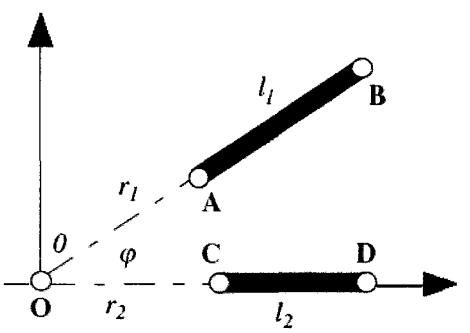

Figure 3-5: Front-view of the case studied by Xiang [25]

In this drawing, the plates are assumed to extend infinitely into and out of the page. It is an inherent assumption of the 2-D case that the plates are parallel in the Z

direction, the direction not shown. In other words, if a top view is provided (X-Z plane), the two planes would be seen as parallel. This analytical solution is exact for 2-D while its extension to 3-D is an approximation.

The details of the work are outside the scope of this thesis however the results are of direct benefit and therefore reproduced. The capacitance between the two plates, C_{inc}, has two components. One results from the field between the two plates,C_{in}, and the other from the field circling around the two plates, C_{out}.

$$C_{inc} = C_{in} + C_{out} \tag{3.20}$$

If the modulus k_{in} is defined as:

$$k_{in} = \sqrt{\frac{\left(r_1^{\frac{\pi}{\varphi}} + r_2^{\frac{\pi}{\varphi}}\right)\left((r_1 + l_1)^{\frac{\pi}{\varphi}} + (r_2 + l_2)^{\frac{\pi}{\varphi}}\right)}{\left(r_1^{\frac{\pi}{\varphi}} + (r_2 + l_2)^{\frac{\pi}{\varphi}}\right)\left(r_2^{\frac{\pi}{\varphi}} + (r_1 + l_1)^{\frac{\pi}{\varphi}}\right)}} \tag{3.21}$$

where r_1, r_2, l_1, and l_2 are defined in Figure 3-5; and the inside capacitance, C_{in}, is found to be:

$$C_{in} = \frac{K'(k_{in})}{K(k_{in})} \tag{3.22}$$

where

$K(k)$ is the complete elliptical integral of the first kind,

$K'(k) = K(k')$ and,

k' is the complementary modulus of k.

From Equation (3.21) it is found that:

$$k_{in}^{'} = \sqrt{\frac{\left((r_1 + l_1)^{\frac{\pi}{\varphi}} - r_1^{\frac{\pi}{\varphi}}\right)\left((r_2 + l_2)^{\frac{\pi}{\varphi}} - r_2^{\frac{\pi}{\varphi}}\right)}{\left((r_1 + l_1)^{\frac{\pi}{\varphi}} + r_2^{\frac{\pi}{\varphi}}\right)\left((r_2 + l_2)^{\frac{\pi}{\varphi}} + r_1^{\frac{\pi}{\varphi}}\right)}} \tag{3.23}$$

Similarly the capacitance resulting from the field outside the acute angle, c_{out}, is:

$$C_{out} = \frac{K^{'}(k_{out})}{K(k_{out})} \tag{3.24}$$

where:

$$k_{out} = \sqrt{\frac{\left(r_1^{\frac{\pi}{2\pi-\varphi}} + r_2^{\frac{\pi}{2\pi-\varphi}}\right)\left((r_1 + l_1)^{\frac{\pi}{2\pi-\varphi}} + (r_2 + l_2)^{\frac{\pi}{2\pi-\varphi}}\right)}{\left(r_1^{\frac{\pi}{2\pi-\varphi}} + (r_2 + l_2)^{\frac{\pi}{2\pi-\varphi}}\right)\left(r_2^{\frac{\pi}{2\pi-\varphi}} + (r_1 + l_1)^{\frac{\pi}{2\pi-\varphi}}\right)}} \tag{3.25}$$

and:

$$k_{out}^{'} = \sqrt{\frac{\left((r_1 + l_1)^{\frac{\pi}{2\pi-\varphi}} - r_1^{\frac{\pi}{2\pi-\varphi}}\right)\left((r_2 + l_2)^{\frac{\pi}{2\pi-\varphi}} - r_2^{\frac{\pi}{2\pi-\varphi}}\right)}{\left((r_1 + l_1)^{\frac{\pi}{2\pi-\varphi}} + r_2^{\frac{\pi}{2\pi-\varphi}}\right)\left((r_2 + l_2)^{\frac{\pi}{2\pi-\varphi}} + r_1^{\frac{\pi}{2\pi-\varphi}}\right)}} \tag{3.26}$$

It may be shown that for the limit case of $\varphi = 0$:

$$\lim_{\varphi \to 0} C = \varepsilon \frac{l}{h} \tag{3.27}$$

where h is the distance between the two planes. This agrees with Equation (3.19) for the parallel-plate capacitor recalling that in the 2-D case the area is reduced to only l.

3.5.1 Comparison of 2-D Inclined-plate Model and the Parallel-plate Model

The previous model gives an alternative for the estimation of the large gapped plates with the right choice of r_1, r_2, l_1, l_2, and φ. Due to the presence of π/φ factors, it is impossible to set φ to zero in the numerical calculations and small angles will be used to

obtain comparable results. To justify this approximation it should be noted that Equations (3.24) and (3.22) are continuous in the neighbourhood of $\varphi = 0$. To compare with the parallel-plate approximation, the two plates with equal width, l_1 and l_2 are defined. To graphically illustrate the continuity of the capacitance value, the angle φ changes from 5° to the neighbourhood of zero. To maintain consistency with the original equation, the corresponding r_1, r_2, and h are found for the given l and φ:

$$r_1 = \frac{h}{sin^{-1}\varphi} \tag{3.28}$$

$$r_2 = \frac{h}{tan^{-1}\varphi} \tag{3.29}$$

An electrode size of 30x10cm^2 at the distance of 10cm is chosen. This choice of electrode size is related to the electrodes installed in the experimental setup later. Numerical constraints limited the minimum angle sweep to 0.5°. Figure 3-6 illustrates the estimated values of capacitance for the small angles of up to 2°. The dashed line is the approximation using the parallel-plate formula. It is seen that due to the relatively large gap between the two plates, the parallel-plate model is an underestimation. To compare the results with the parallel-plate case, a small value of $\varphi = 1°$ was assigned. Figure 3-7 compares results of the parallel-plate approximation and Xiang's method for increasing air-gap size while maintaining the angle. For the 10x30cm^2 electrodes in use, and at the distance of 50cm, the parallel-plate estimation is 0.53pF. The inclined-angle method estimates the value to be at 2.12pF which is a ratio of 1:4. While this difference is not in direct agreement with the results of the MoM by Ma, agreement with the experimental data supported the method proposed by Xiang as seen in Figure 3-8. The maximum

deviation from the experimental data available is 1.33pF at the distance of 30cm. This is partly attributed to the fringing effect in the third dimension ignored by Xiang as well as the sensor errors. The details of these experimental apparatus are provided in Chapter 5.

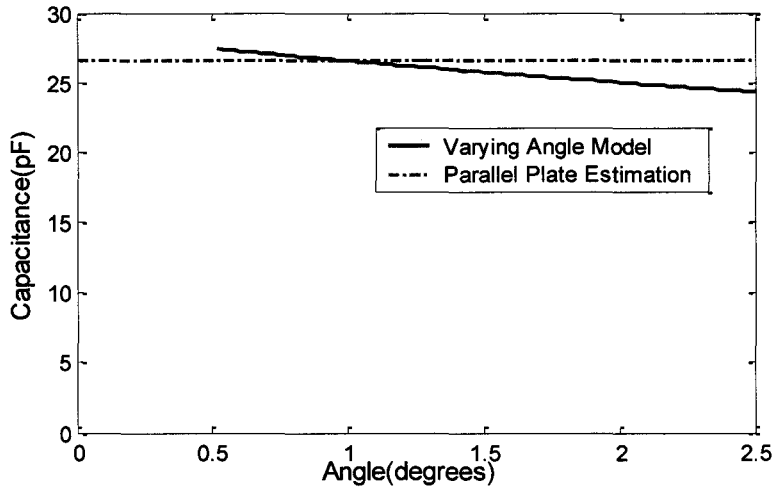

Figure 3-6: Continuity of the capacitance for changing angles for 10x30cm electrodes

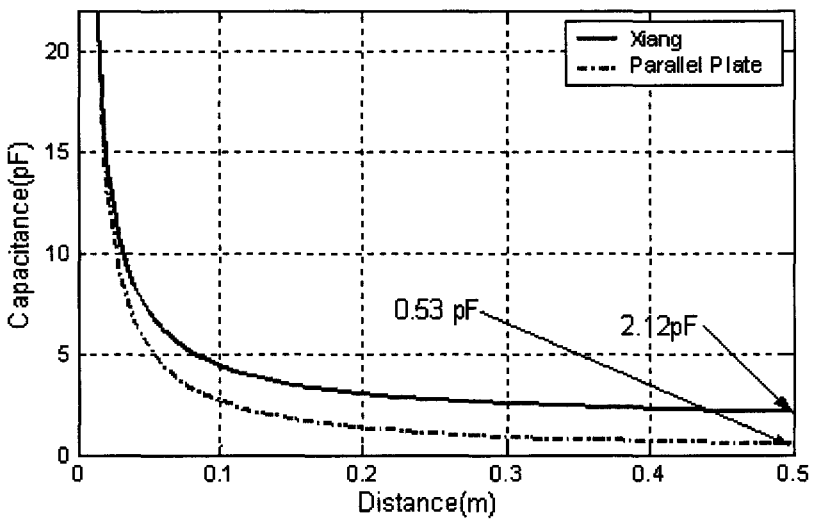

Figure 3-7: Comparison of Xiang's model with the parallel-plate model

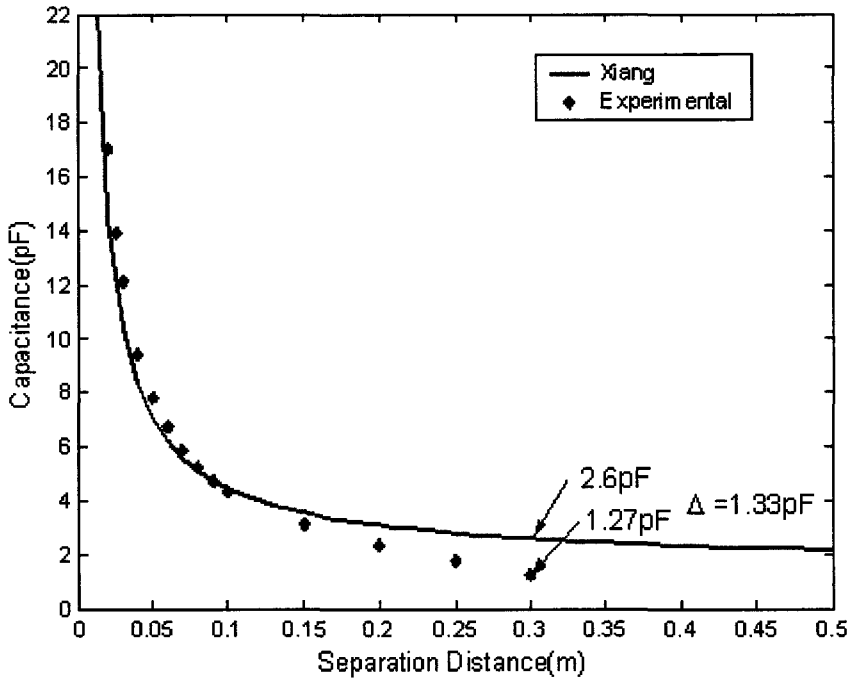

Figure 3-8: Xiang's model compared with the experimental data for 30x10cm^2

3.6 The Measurement Techniques

So far in this chapter computational methods for finding the capacitance of a known geometry were discussed. However it is the real-life measurement of the capacitance that is the primary interest of a proximity sensing system for a collision avoidance application.

3.6.1 Charging Time

A primitive form of capacitance measurement could be achieved through the charging time of the capacitor. Figure 3-9 is a basic series RC circuit for charging a capacitor.

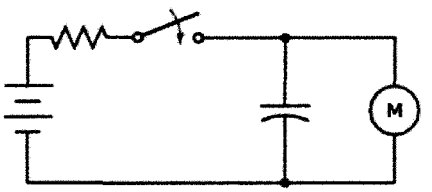

Figure 3-9: RC circuit

It could be derived that the voltage across the capacitor is:

$$V_C = V_{source}\left(1 - e^{\frac{t}{RC}}\right) \tag{3.30}$$

This technique is static and requires discharge of the capacitor before each measurement cycle, making it a non-ideal method for dynamic applications.

3.6.2 Tuned Resonator

Capacitors have been widely used as tuning elements in resonating circuits. If the test capacitance is part of the resonator, the frequency of the oscillator is related to the capacitance being tested. With the aid of an appropriate excitation circuit, the parallel LC circuit shown in Figure 3-10 produces a sinusoidal wave[1].

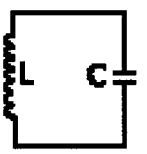

Figure 3-10: The LC Resonator

From the Kirchhoff's Laws of Electricity and the current-voltage relationship in the capacitor and the inductor, it is derived that:

$$f = \frac{1}{2\pi\sqrt{LC}} \tag{3.31}$$

[1] Circuits for LC resonator excitation are widely used. In the interest of space and clarity, the details are avoided

if L is in Henries and C is in Farads, the frequency would be in Hertz. Equation (3.32) could be rearranged to:

$$C = \frac{1}{L\,(2\pi f)^2} \tag{3.32}$$

A problem hampering the use of this technique in the collision avoidance applications is the magnitude of capacitances involved. As reported in the previous section, practical-sized electrodes result in capacitances of pico-Farad magnitude. That leads to very high frequencies. It should be noted that the problem is further exasperated by the practical preference to maintain the relative parity between the inductor and the capacitor values.

3.6.3 Impedance Monitoring

The primary method for measurement of the capacitance is impedance evaluation. In the complex domain, the capacitance adheres to the Ohm's Law and therefore any change of the capacitor would result in a shift in the impedance of the circuit. The general layout is depicted in Figure 3-11.

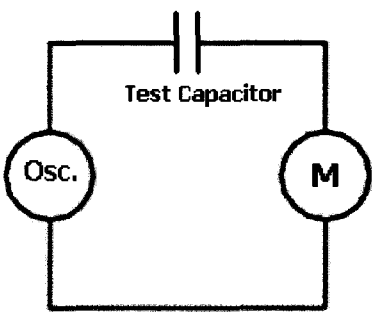

Figure 3-11: Measuring impedance of a capacitor

$$\tilde{Z}_c = \frac{1}{j\omega C} = \frac{1}{\omega C} e^{j\left(-\frac{\pi}{2}\right)} \tag{3.33}$$

Remembering Ohm's Law:

$$V = \frac{I}{R} = \frac{I}{\frac{1}{j\omega C}} \tag{3.34}$$

the capacitance is:

$$C = \frac{V}{j\omega I} \tag{3.35}$$

The relationship results in a lag in voltage illustrated in Figure 3-12. By adding a resistance, the impedance could result in a change in the amplitude. In the circuit of Figure 3-13, the amplitude measured across the capacitor depends on the capacitance.

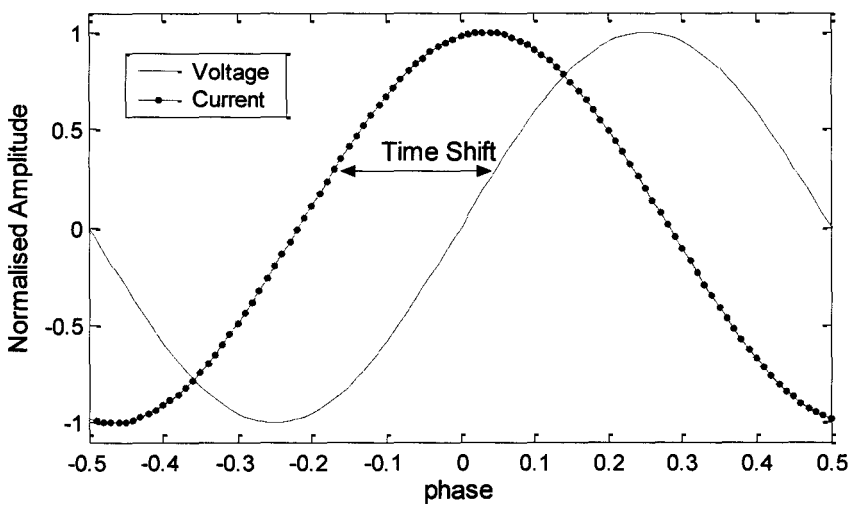

Figure 3-12: Voltage and current time-shift through a capacitor

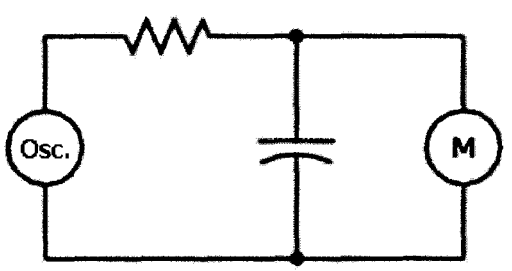

Figure 3-13: Amplitude drop circuit

$$V_c = V_{oscillator} \times \left(\frac{Z_c}{Z_c + Z_R}\right) \tag{3.36}$$

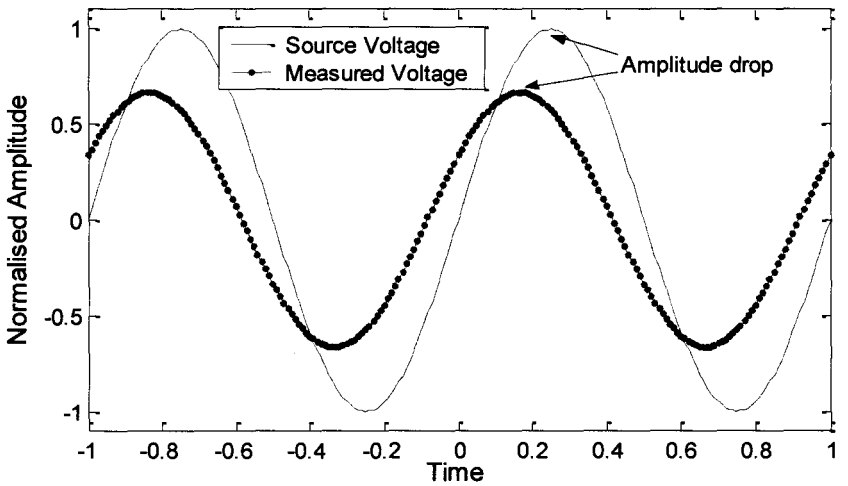

Figure 3-14: Voltage drop across a resistor

In the preceding circuit, the impedance does not only lead to a time shift but also it affects the amplitude. This parameter is intrinsically easier to measure[1].

$$Z_C = \frac{V_c \times R}{V_{oscillator} - V_C} \tag{3.37}$$

In the aforementioned arrangement, the test capacitor could be probed with the need for only one explicit connection by using a common ground between the oscillator, the measuring circuit and the test capacitors. The circuit would be completed through the ground as put forward in Figure 3-15.

[1]A basic rectifier-filter circuit could measure the peak-to-peak voltage. The practical details are omitted in the interest of space.

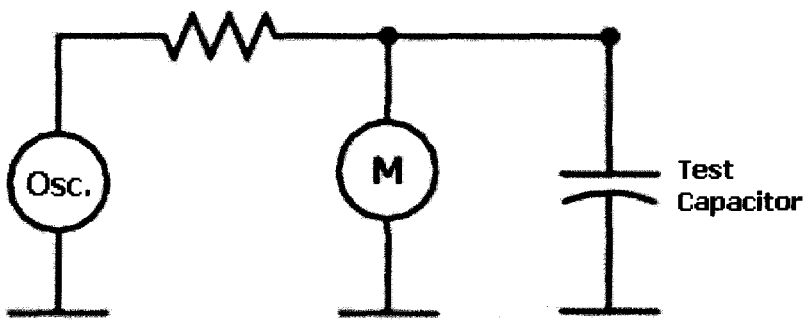

Figure 3-15: Ground-completed circuit

As previously noted, the impedance evaluation technique is the most common method of capacitance measurement for proximity sensing [27,I28,I17,I20,I18,I23]. With this approach, it is possible to use two or more frequencies for signal modulation to minimise the numbers of physical electrodes needed [18].

3.7 Circuit Topologies

In the previous section, various methods to measure capacitance were discussed. The circuit topology is yet another factor in the design. The topology refers to the placement of the test capacitor in the circuit. A wide range of circuit topologies as well as the formation of the capacitor as the proximity sensor are discussed in this section.

3.7.1 Capacitance to Ground

A very common method is the measurement of the capacitance to ground as discussed in Section 3.6.3. In this formation, the test capacitance completes the circuit to ground. The advantage of this approach is that only one plate is needed. The body of grounded obstacle forms the "second" plate of the capacitor. In the collision avoidance applications the grounded body of a robot could provide this second plate. Without the need for an explicit second plate, the human body could also act as the second plate. This

is commercially applied in automotive safety applications[1] A major disadvantage of this topology is the vulnerability to the parasitic capacitances to ground. The electrode cables and all shielding have unwanted capacitance to ground. This parasitic capacitance could be of higher order of magnitude than the signal being measured [29]. Particular to the collision avoidance applications, if the electrode is installed on robot A to detect robot B, the body of robot A causes a large unchanging common-mode capacitance.

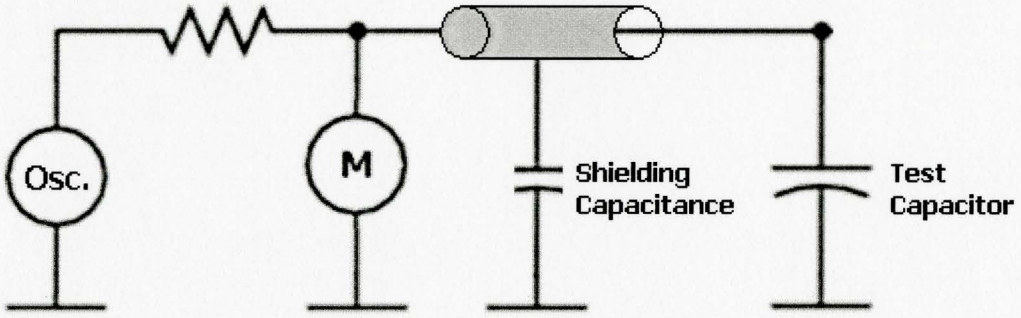

Figure 3-16: Parasitic capacitances to ground

To overcome this problem, it is possible to drive the shielding with the same source signal as the excitation. When the shielding and the electrode probe are energised simultaneously, no potential difference between them could arise and therefore no discharge would happen. This method is known as active shielding. The diagram in Figure 3-17 explains the idea.

[1] Capacitive sensing is preferred to detect presence of an occupant in passenger seat for activation of the SRS Air Bag. The capacitive sensors is more resilient to false detection compared to weight sensors.

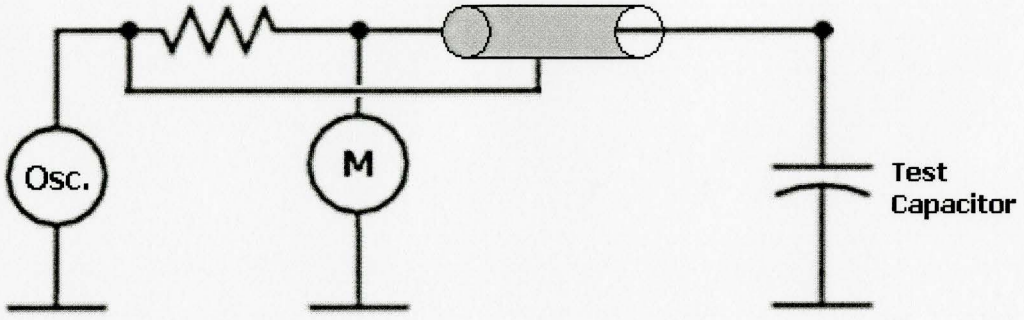

Figure 3-17: Active shielding to reduce effect of the parasitic capacitances

To provide isolation between the grounded robot and the closely installed electrode, a similar method could be deployed. The "capaciflector" concept as proposed in [30]provides such an isolation. The concept is shown in Figure 3-18.

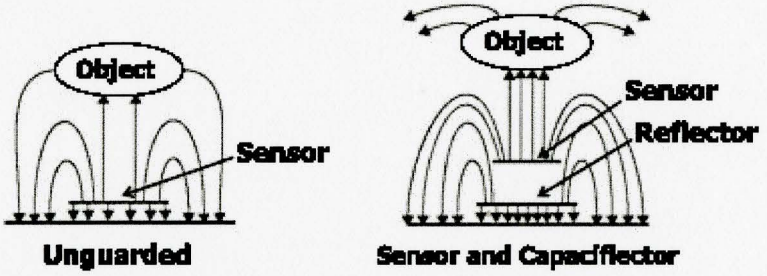

Figure 3-18: The effect of a capaciflector [30]

3.7.2 Isolated Capacitor

For the systems that measure the capacitance to ground, the excitation and sense signals are connected to the same electrode. To address the problem of the parasitic capacitances, the capacitor being measured could be isolated from the ground and other shared current paths. With two explicit "plates" available, the capacitance could be measured specifically between the two plates without the ground effect.

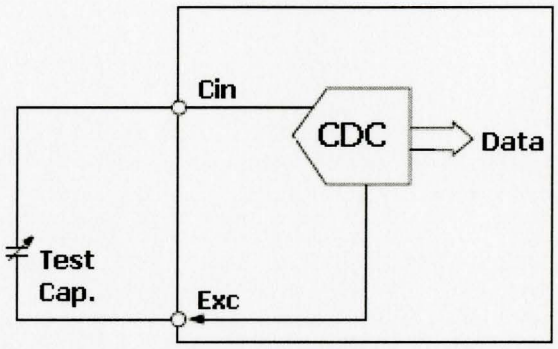

Figure 3-19: Isolated capacitor

Novak and Feddema [18] [23] and Karlsson and Järrhed [20] used this technique in two different applications of collision avoidance as reviewed in Chapter 2. Although in theory this method is insensitive to parasitic capacitance to ground, in practice a large capacitance to ground leads to signal distortion. The signal measured on the sense electrodes is dependent on both the capacitance and the excitation signal. Practically the driver for excitation signal would have nonzero impedance and the parasitic capacitances could dampen the excitation signal which would dampen the measured signal for the same capacitance.

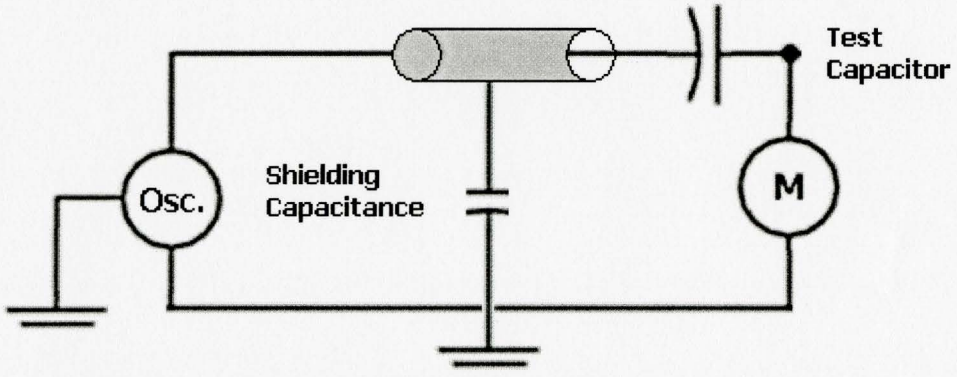

Figure 3-20: Effect of parasitic capacitance on circuits with output impedance

Since in most circuits, $V_{excitation}$ is assumed a constant. In extreme cases, the parasitic capacitance could lead to a drop in its effective amplitude. Assuming that the measuring circuit not a source of current leakage, $V_{excitation}$ is

$$V_{excitation} = V_{oscillator} \times \left(\frac{\frac{1}{j\omega C_{parasitic}}}{\frac{1}{j\omega C_{parasitic}} + R_{output}} \right) \quad (3.38)$$

This equation describes both an amplitude change and a phase distortion affecting the signal. For example, Analog Devices AD7142 tolerates up to 40pF between the input and ground while maintaining its declared accuracy.

3.7.3 Measurement by Field Alteration

As earlier explained, a defining factor in the value of the capacitance being measured is the geometry of the setup and the gap between the two electrodes or ground. The motion of the robot leads to changes in the capacitance. Yet this is not the only way by which proximity measurements could be obtained. If a foreign object occupies the space between the two fixed electrodes, the value of capacitance would change. This would happen whether one of the electrodes is ground or two explicit electrodes are in use. In case of conductors, the intruding object changes the field pattern. The insulators change the dielectric of parts or the entire gap. Karlsson and Järrhed [20] exploit this fact to detect the presence of a human in a robotic workcell. In Figure 3-21 the capacitance is measured between the ceiling and floor electrodes (labelled as antennae in the picture) enclosing the workcell. The entrance of a person into the workcell changes the capacitance and triggers an action.

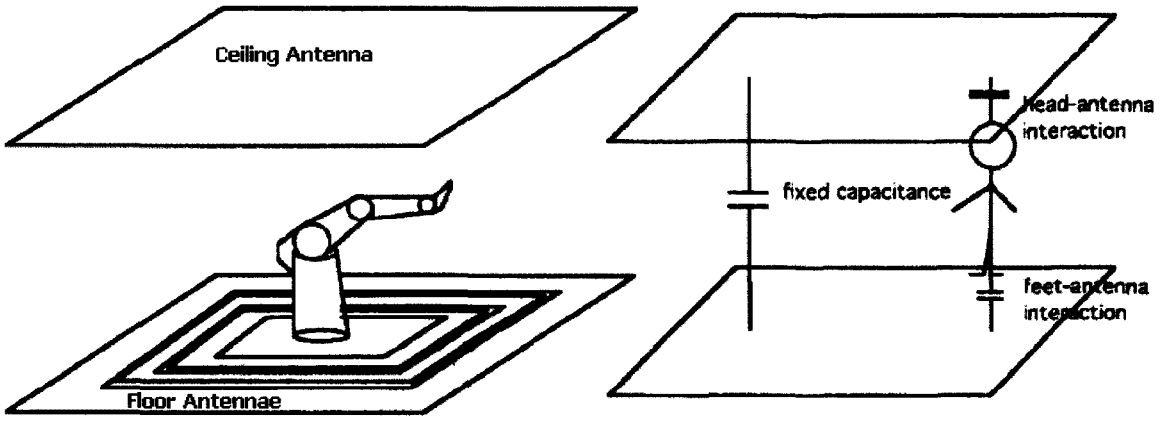

Figure 3-21: The workcell model in [20]

3.8 Conclusion

This chapter provided a brief background to the work by reviewing the physics of capacitance and analytical approaches. The parallel-plate approximation provides a simple method to estimate the capacitance for small gaps, but as the gap increases the assumptions are violated and the errors increase drastically. The simulation work by Ma provides a numerical solution that assists in better understating of the phenomenon but it is slow to compute. In comparison with the experimental data, the model proposed by Xiang is reasonably accurate and will be referred to later. In the second portion of the chapter, the various methods by which the capacitance could be measured were reviewed. That was then followed by a brief look at the relevant circuit topologies. The capacitor to ground topology offers a simple solution but with the isolated capacitor layout, the effects of parasitic capacitances are minimised, and a more accurate capacitance measurement is achieved. For this reason the isolated capacitor layout will be used in this thesis.

CHAPTER 4

Robot Arm Capacitive Signature

4.1 Introduction

The relationship between the capacitance and the distance between the objects concerned is very nonlinear (for example as in Figure 2-9). It is also dependent not only on the distance but the orientation of the capacitor plates and to the other objects in the vicinity [19,I18,I23]. This research exploits this indiscriminate sensitivity to provide a real-time monitoring of the environment. The environment might include static objects, other robots and other machinery. While proximity sensors like infrared provide a local distance measurement, the broad area coverage provided by capacitive sensing can provide a solution in many collision voidance settings. This chapter will start by introducing the proposed collision avoidance and the experimental hardware. The concept of capacitive signature is then introduced and the systematic requirements for creation of this signature are discussed. This is followed by a discussion of the use of multiple electrodes and a conclusion.

4.2 Overview of the Collision Avoidance Approach

For most production line robots, a high degree of predictability is required and autonomy is generally not desirable. Hence collision avoidance is confined to the prediction and prevention of a collision by timing control and pausing the robot. That is

in contrast to the mobile robots where autonomous path planning and self-navigation is an objective. There are reasons why speed alteration is preferable to path alteration for industrial arms. Most importantly is that the path could part of the manufacturing process as it is in grinding or welding. This difference is to a degree a subjective disparity. By choosing binary speed alteration (*i.e.* stop and go) the least changes to the existing robot programmes are required. This approach is also applicable as a fail-safe collision avoidance system in situations where the speed is not modifiable. With binary speed alteration, the immediate cycle is disrupted at the potential cost of one workpiece but machine damage is averted. This approach also allows for a simple digital interface between the native robot controllers and the collision avoidance supervisory controller. This makes it compatible with the input/output capabilities of virtually all industrial robots.

4.3 Experimental Hardware

To assist with the upcoming description of the system and analysis, the structure of the system hardware will now be presented. For this thesis, a two-robot arm workcell is investigated. One arm is a CRS F3 controlled by a CRS C-500 controller referred to as the F3. The second arm is a non-actuated single revolute joint arm referred to as R2. The capacitance measurements are performed by the measurement hardware connected to the control PC or the "supervisor". The supervisor is able to control the motion of the F3 through its digital input/output interfaced through an isolation board. The position of the first joint of the active robot, F3, is measured through a rotary encoder independently connected to the control PC. The use of an external encoder is needed in absence of a

reliable high-speed feedback from the C-500 controller The encoder has a resolution of 12 counter per degree of joint 1

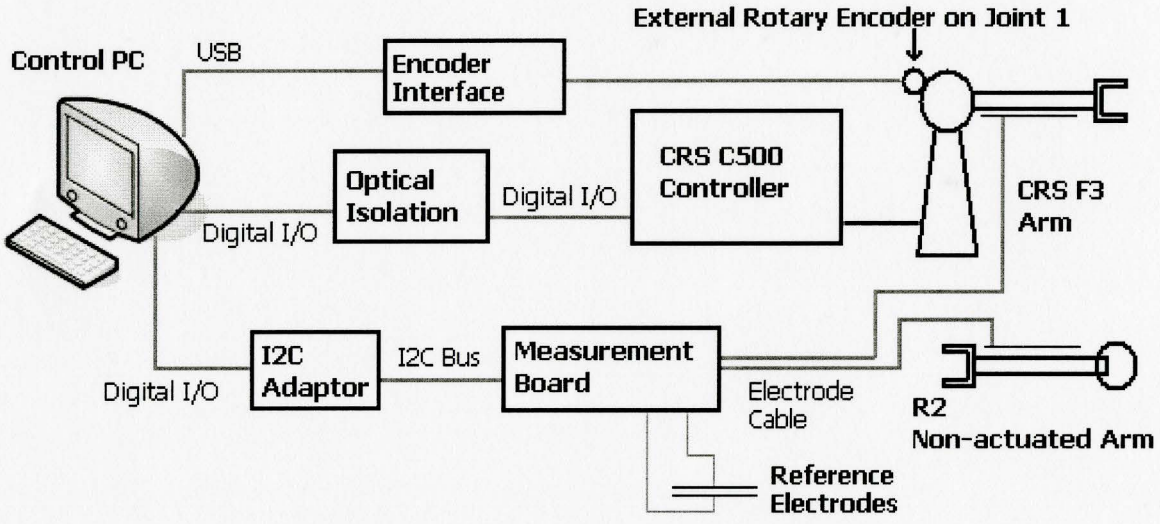

Figure 4-1: Layout of the system hardware

4.4 Capacitive Signature of an Arm

The aim is to provide safety in a workcell with multiple robots. If a given arm motion is associated with a unique and repeatable signature[1], a comparison of the runtime and expected signature should identify any abnormality The signature will be obtained from the capacitive values of the appropriately placed electrodes. If guarded robots come closer than it is acceptable or intended, this signature will change. Theoretically speaking, the misplacement of *any* object in the environment, particularly the metallic robot arms or the work pieces, will impact the signature. This runtime deviation could be used to trigger preventive actions. Beyond that, the advantage of the signature monitoring is that any irregularity is noticed ahead of time without the need for "close calls" That is to say, while the immediate next move might not be obstructed, the environmental irregularity

[1] Vibration signatures are used in the condition monitoring of the machines, e.g. [30]

could be a sign of a forthcoming problem. To explain, it is best to review the common case of two cooperating arms controlled independently. For clarification, a *cycle* refers to one complete motion sequence of an arm or arms in a repetitive operation. That is to say, consecutive cycles are identical and the sequence is reset and repeated at the end of each cycle. During normal operation, for any given moment in the cycle, the position of the two robots with respect to each other is well-defined. The position of the robots with regard to any external object including a workpiece is also well-defined at any given moment. This establishes a constant electric field arrangement and therefore a constant capacitance for a particular instant during the cycle. Remembering the general equation for capacitance Equation (3.13), repeated as (4.1), it is evident that an analytical or numerical calculation of the expected capacitive signature is cumbersome if not impossible[1].

$$C = \frac{Q}{V} = \frac{\int_s \varepsilon \vec{E} \,.\, d\vec{s}}{\int_{p_1}^{p_2} -\vec{E} \,.\, dl} \tag{4.1}$$

On the other hand the expected capacitive signature could be measured in advance and recalled at runtime for comparison. Equation (4.1) depends on the geometry and ε. Hence for any given physical state of the robot and its environment, assuming the electrodes are designed properly, the value of capacitance is unique for an unchanging dielectric. The correlation between the capacitive metric and the state of the robot and its environment is the essence of the proposed collision avoidance system. Figure 4-2 is the capacitive profile of a single pair of electrodes mounted on the two-arm setup shown in

[1]Finite element modelling also fails to meet the needs [19]

Figure 4-3 for one cycle. The horizontal axis is the percentage of the cycle completed, and the vertical axis is the measured value of capacitance. The white robot (F3) in the picture travels over the lower robot (R2) moving from the left to the right. The peak is when the F3 is directly above R2. The two electrodes are installed on the upper arm of the F3 and the main body of R2. As should be expected, for a given task, the shape of the profile is also dependent on the placement of the electrodes. As such, the ideal placement of the electrodes is of key importance.

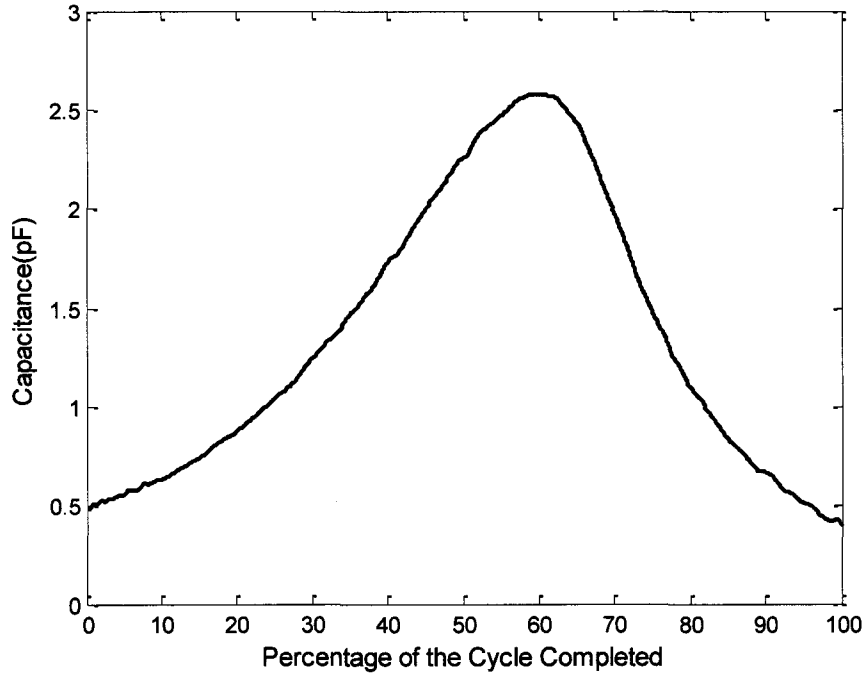

Figure 4-2: Capacitance profile for a cycle

The capacitive signature of a cycle is defined to be the values of all electrodes, for every point throughout the job cycle. The next section examines the method to find the status of the robot in its cycle.

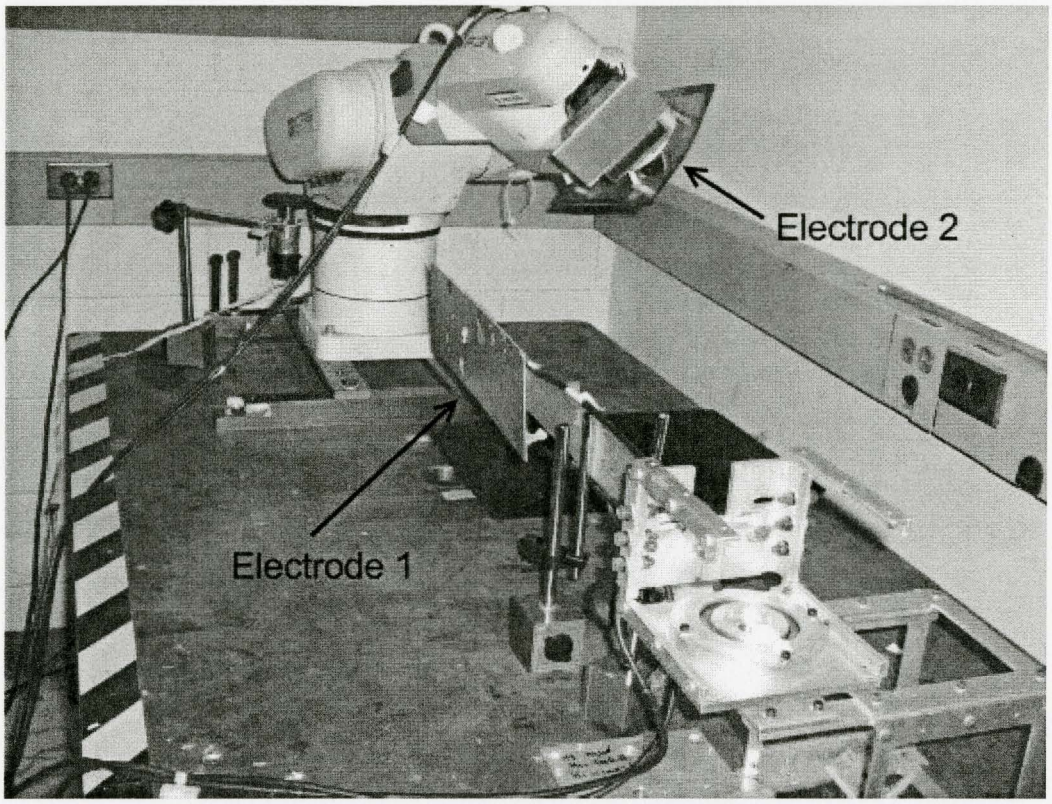

Figure 4-3: Basic two-robot test platform

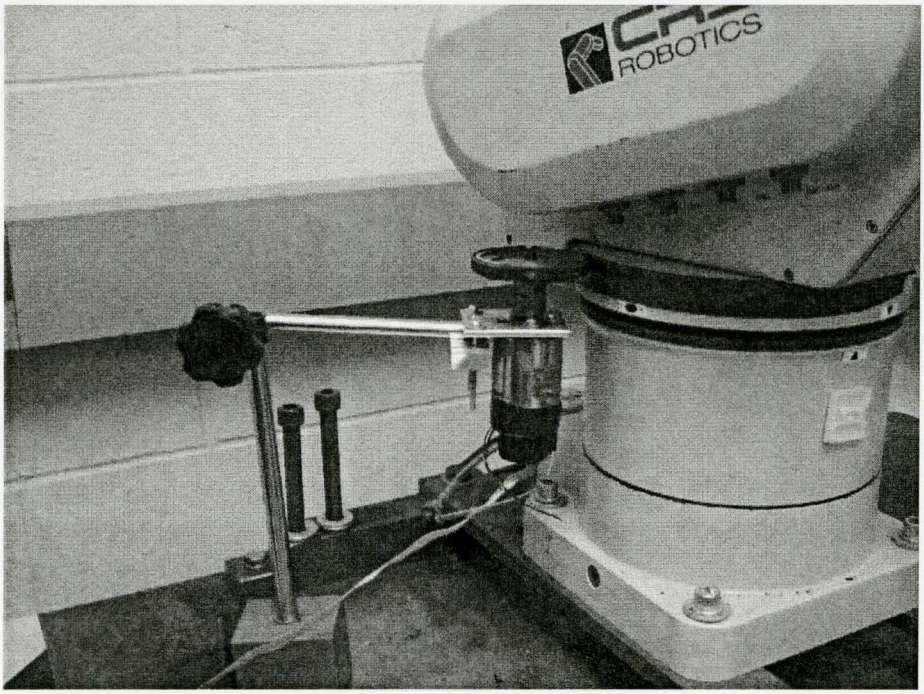

Figure 4-4: External encoder reading angle of the F3 Joint 1

4.5 Cycle Proportioning

It was discussed in the previous section that to create a signature, the capacitance is measured for every "instant" of the cycle. However, these instants cannot be derived from the elapsed time, since time and the percentage of the cycle completed or the "cycle fraction" are not truly correlated. To ensure that a reliable correlation between the time and the cycle fraction exists, it must be guaranteed that the exact start of the cycle is known and that the cycle is continuous in time. Neither requirement can be reliably met for all robots and controllers. With the addition of a collision avoidance system which can interrupt the motion, the time of a cycle becomes unpredictable. For example, if a cycle is known to take ten seconds when uninterrupted, this time will be unknown when interruptions are possible. Although the pause commands are issued by the CAS, the uncertainty in the robot reaction-time makes time irrelevant. For example, the CRS F3 arm with a C-500 controller used in this thesis exhibited up to 400ms of delay. Figure 4-5 shows the dispersion of this reaction-time at 10% of the maximum speed. Similar uncertainties have been observed for a PUMA 560 arm with a VAL II controller.

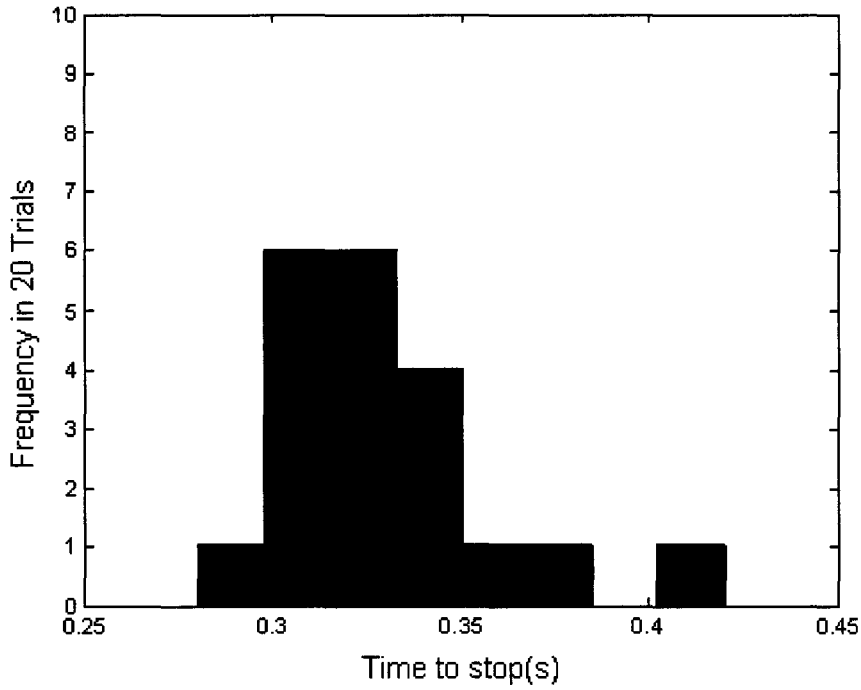

Figure 4-5: F3 reaction-time histogram for 20 trials at speed 10

The solution proposed in this thesis is to use the total arc length of all robots in joint space to measure the cycle fraction. This relationship between the total arc length and the cycle fraction will be proportional so long as the robots are synchronised. This is an acceptable assumption since synchronisation is required for the normal operation of a workcell containing multiple arms. An example is shown for a single DOF robot in Figure 4-6. In this case, the total arc length is simply equal to the integral of the absolute value of the joint velocity. It should be noted that the total arc length is independent of the time and therefore the robot may be paused to avoid collisions without affecting this relationship.

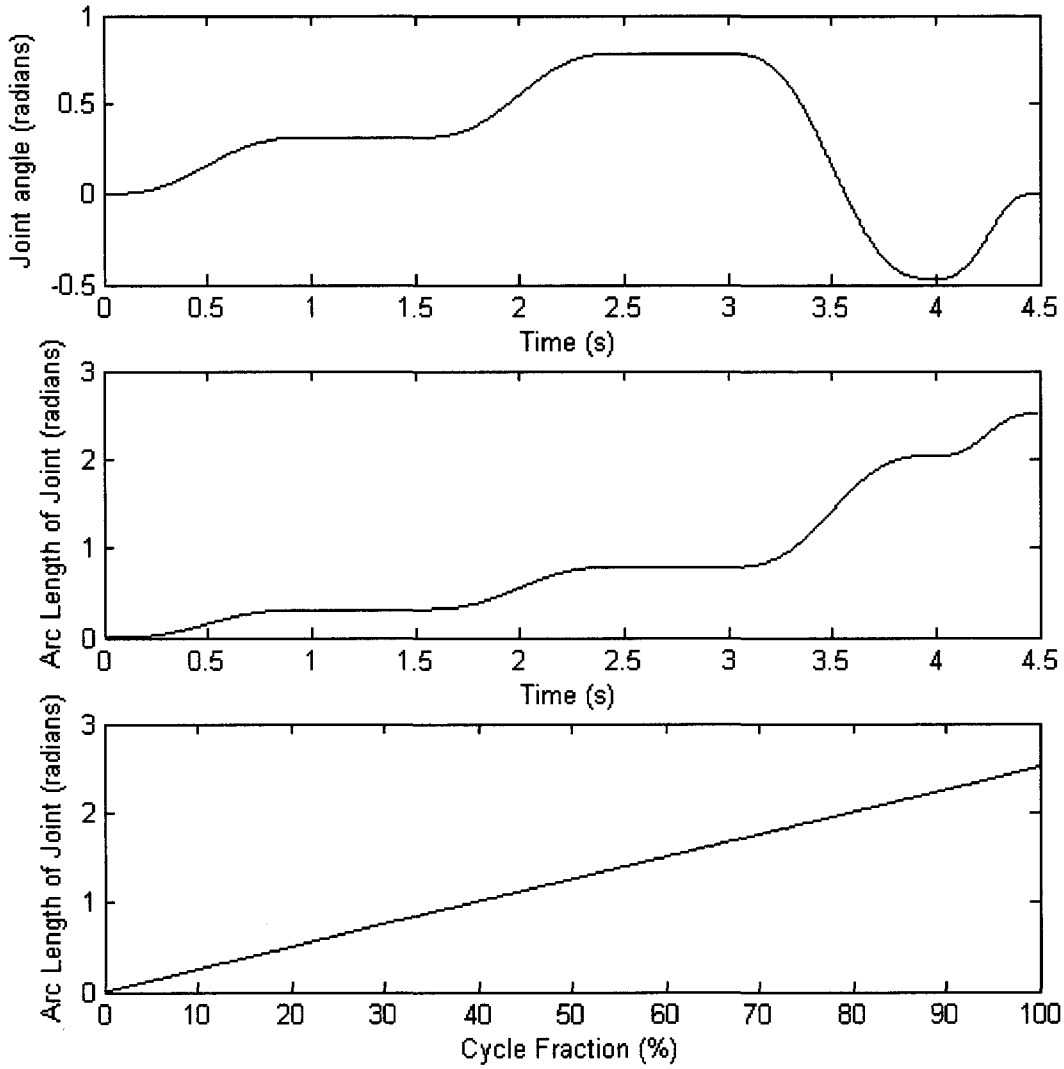

Figure 4-6: Joint angle versus time (top), arc length versus time (middle), and arc length versus cycle fraction bottom for a single DOF robot

4.5.1 Arc Length Estimate Simplification

For a typical 6-DOF industrial robot computing the total arc length requires knowledge of all joint velocities at frequent intervals. For a workcell with two arms, the number of real-time measurements jumps to 12, adding to the complexity of the data collection process and software. That being said, any one-to-one relationship between

any one joint and the cycle fraction is sufficient. For example if the first joint has a continuous, unidirectional motion throughout the length of the cycle, the value of Joint 1 can serve as the cycle fraction indicator. This simplifies the data acquisition and processing significantly; and this approach will be used in this thesis.

4.6 Electrode Multiplicity

Theoretically, any change in the workcell will result in a change in the value of the capacitance and a deviation from the expected capacitive signature. Yet the sensitivity of the system is subject to the practical limits of the sensors. As seen before, the influence of objects on the value of a capacitor is inversely proportional to the distance from the electrode-pair. Therefore, abnormalities further away from the sensor plates could be not detected with a finite resolution or they would amount to a smaller variation than the expected noise. As such, more than one pair of electrodes may be necessary to provide required sensitivity in all areas at risk and a layer of redundancy. The signature profile of the system will therefore contain readings from all the sensors. Figure 4-7 is an example of a setup in which more than one electrode-pair has been chosen to provide protection for the robots. The electrodes on the side and underneath the arm provide maximum sensitivity in the directions that a collision is likely. Higher local sensitivity enables the system to show higher tolerance against the noise. If the features in the signatures are more distinguishable and the geometric changes are more noticeable, more relaxed limits could be imposed. This leads to an enhanced robustness against bad readings. Figure 4-8 shows two signatures for identical cycles with only the placement of sensors changed. It is evident how the features of this workcell are more pronounced in Combination 1.

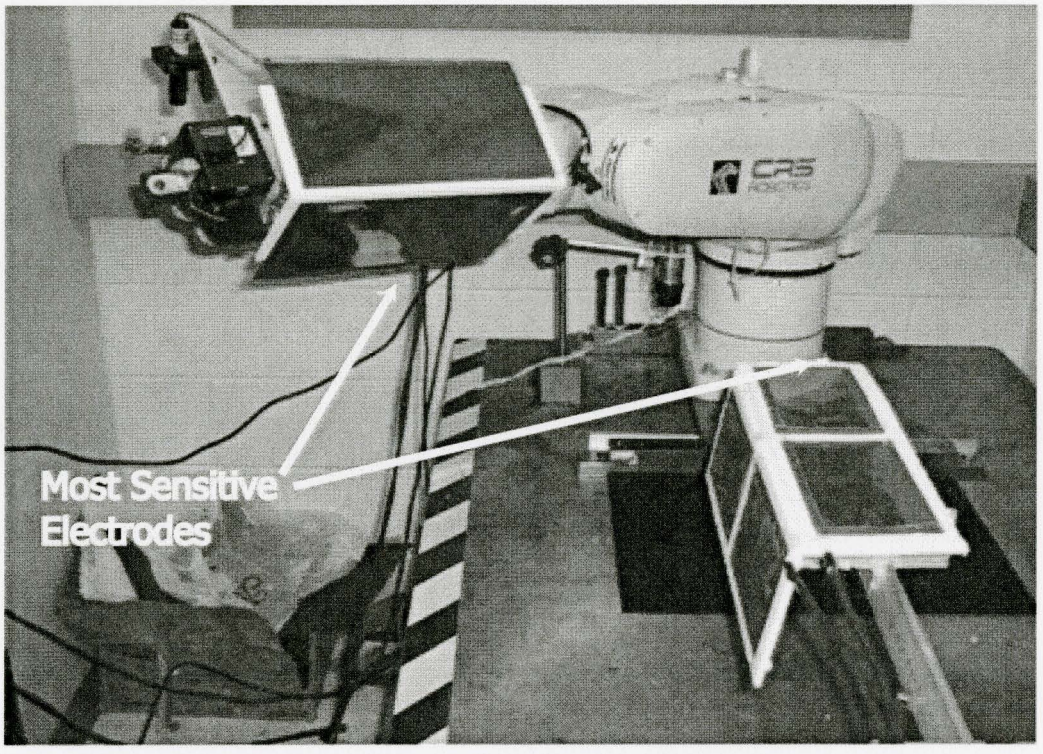

Figure 4-7: Two robots with more than one electrode-pair.

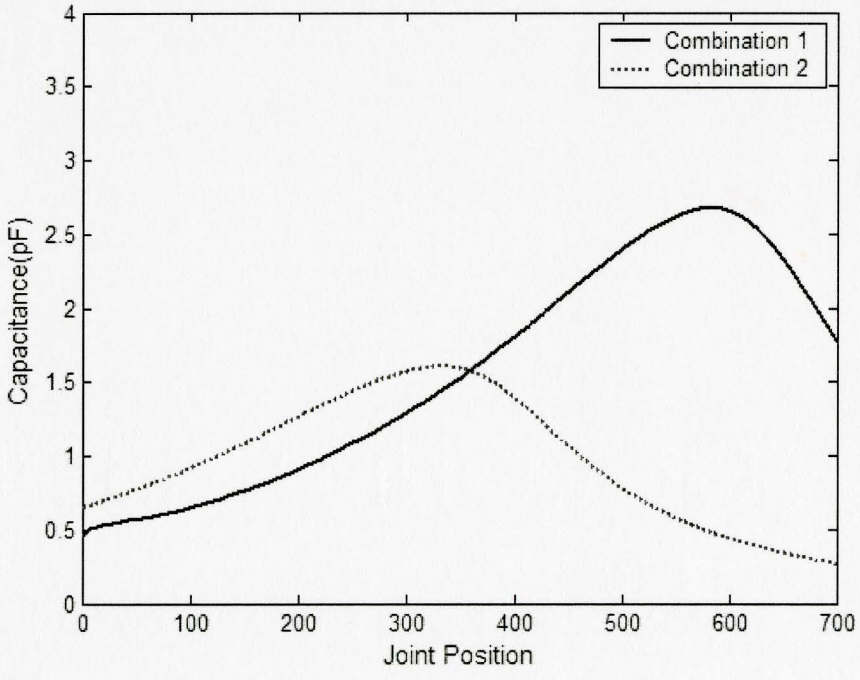

Figure 4-8: Effect of electrode placement

4.7 Conclusion

For applications where the path of the robot cannot be arbitrarily defined, speed variation is the most viable option as the collision avoidance strategy, with "stop and go" its most basic form. It requires only minimal interaction with the robot controllers, a capability that is widely available on industrial controllers. A brief look at the work of the others in the field and preliminary experiments indicated that establishing an inverse model of capacitance is unsuitable for industrial applications. Due to its nature, each application and setup requires the cumbersome development of fitting a linear model. To provide large-area coverage with a smaller number of sensors, the sensors have to be unfocused. That prevents derivation of the minimum distance between the bodies for individual points. Alternatively, in cases where a pre-defined environment is at hand, the capacitive metric provides the means to detect unexpected circumstances. An analogy would be the use of checksums to verify integrity of computer files. While the checksum data does not contain the original data or recovery information (the exact distances in this case) it can reliably indicate a corrupted file (a potential collision in this case).

To create a reusable signature, the capacitance values must be related to the state of the robot throughout its cycle. The arc-length of the arms is representative of this cycle fraction. While calculating the exact arc-length is not always practical or desirable, any parameter that has a one-to-one correlation with the arc-length is sufficient. To this end, the position of Joint 1 of the F3 arm has been chosen and the motion is defined to ensure that this value is only increasing for each cycle. The training and operation of the CAS

rely on this cycle fraction to synchronise. In the following chapters the generation and use of this arm capacitive signature will be shown.

CHAPTER 5

Data Acquisition and Electrode Design

5.1 Introduction

At the heart of this system is the capacitance measurement hardware. In this chapter, the details of the data acquisition system are examined. The circuitry specifications and limitations are analysed. Before proceeding to the statistical analysis of the signature in the later chapters, the sensor data quality and hardware related noise issues are considered. It has already been asserted in the previous chapter that the deployment of more than one pair of electrodes could increase the sensitivity and safety level. The hardware alternatives for multi-pair measurement system are noted and the proposed system is looked at in details. That is complemented by notes on the implications of the expanded hardware on the data rate and quality. Throughout the previous two chapters, the importance of the electrode size and placement was brought up. Design methods and general guidelines for effective design of the electrodes are offered in this chapter. The final discussion is related to the changing dielectric and the methods used to compensate for this changing environmental factor. This section is considered to be a part of the data acquisition system given that it could be integrated into the acquisition process and be in essence transparent from the other subsystems.

5.2 Capacitance to Digital System

To focus the sensitivity on the robots, it is imperative to place the electrode-pair on the arms. By using electrode plates on each arm, the distance between the robots will have a direct and pronounced effect on the capacitive signature. That is in contrast with the case where one robot is part of the changing field of an electrode installed elsewhere. For this reason a chip with isolated measurement topology was needed. The Analog Devices AD7746 chip has been chosen for capacitance measurement. This device provides a direct digital interface and a 21-bit effective resolution. The manufacturer claims an accuracy of up to 4fF [28].

5.3 Details of the AD7746

The AD7746 is a two-channel measurement chip, named a Capacitance to Digital Converter or CDC[1]. The active measurement range of the chip is 8pF with an adjustable common-mode of 18pF. The two channels are processed by a single conversion unit through an internal multiplexer and cannot be used simultaneously. This CDC is capable of differential measurement. In this mode, the result the different between the two inputs is the result. The single-ended mode is always in use for this setup and therefore the reader is spared of the details of the differential mode. Figure 5-1 is the simplified block diagram of the CDC. To improve clarity, certain blocks that are not of use in this research are omitted. The measurement is performed via $EXC1$ and $CIN1(+)$. Figure 5-2 illustrates the connection of test capacitance to the CDC. The differential negative input is disabled via a software setting. The CAPDAC block is explained next.

[1] This term is applied by Analog Devices to its family of capacitance measurement systems.

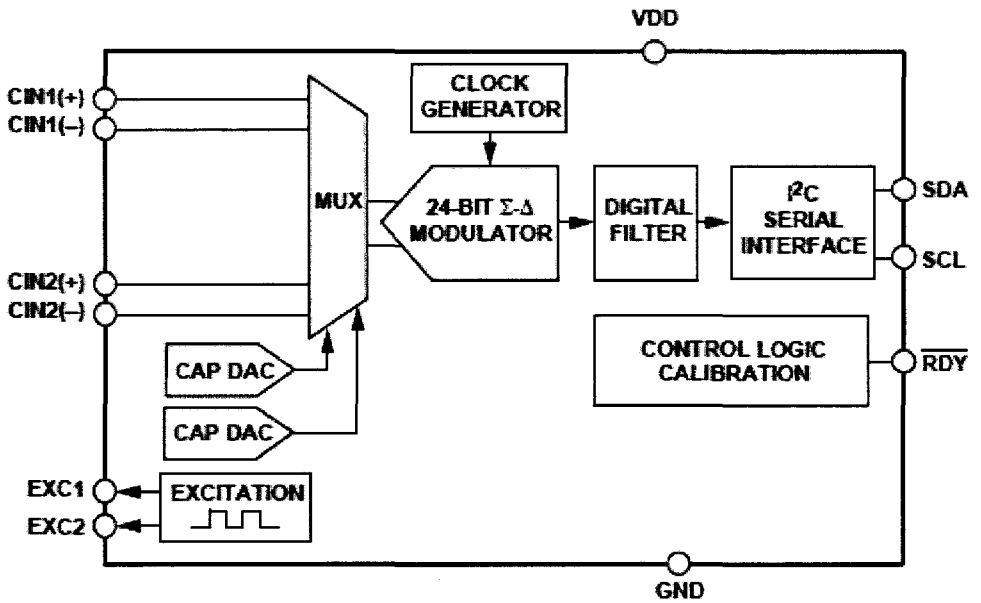

Figure 5-1: Simplified AD7746 block diagram [28]

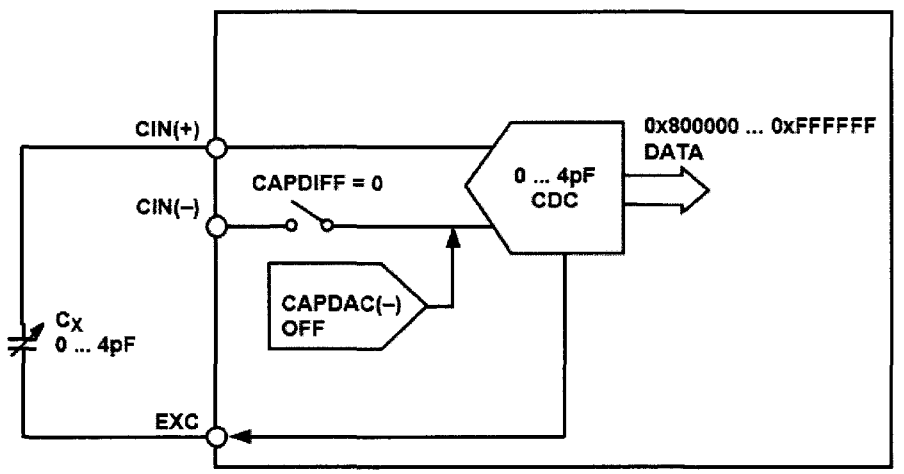

Figure 5-2: Single capacitance measurement [28]

The results of the conversions are provided in a 3-byte packet on the serial interface. The results range from 0 to $2^{24} - 1$ or 0x000000 to 0xFFFFFF hexadecimal. The numbers are in *Excess-23* format [28]. The unsigned integer is biased by 2^{23} as shown in Equation (5.1).

$$C_{CDC} = \frac{((Result_{AD7746}) - 2^{23})}{2^{24} - 1} \times 4.096 \qquad (5.1)$$

where $Result_{AD7746}$ is the value received digitally from the device. The following C code has been used in the interface software:

$$farad = (value * 8.192 / 0x1000000) - 4.096; \qquad (5.2)$$

where *farad* is the capacitance in pF and *value* is the digital readout. As indicated in Figure 5-1, the data passes through a filter layer. The manufacturer states that this is a 3rd order digital filter working on the raw data before the factory calibration corrections are applied. The filter layer improves the noise rejection of the system at the cost of speed. Table 1 lists the expected performance of the device for various filter settings.

Table 1:
CAPDAC conversion performance

CAPDAC Conversion Time (ms)	Output Data Rate (Hz)	-3dB Frequency (Hz)	P-P Noise (aF)	Effective Resolution (Bits)	P-P Resolution (Bits)
11.0	90.9	87.2	212.4	17.6	15.2
11.9	83.8	79.0	137.7	18.2	15.9
20.0	50.0	43.6	82.5	19.4	16.6
38.0	26.3	21.8	50.3	20.1	17.3
62.0	16.1	13.8	33.7	20.5	17.9
77.0	13.0	10.5	28.3	20.7	18.1
92.0	10.9	8.9	27.8	20.8	18.2
109.6	9.1	8.0	27.3	20.9	18.2

The data rate of the sensor is the bottleneck of the entire system. Therefore the CDC conversion time is of major importance for the system if it is to operate in real-time. While an increased throughput results in an apparent increase in the noise levels, it should be noted that the electrical accuracy of the CDC is only one of the factors. It will be shown in the next chapter that many elements including the physical vibrations of the arm can have a much larger contribution to the system noise level. In the experimental

system used throughout this thesis the fastest conversion time setting of 11ms has been opted for. It should be noted that the 11ms variable is the software setting applied to the CDC and is not the sampling period of the system. The sampling period used will be 20ms unless otherwise noted.

5.4 The Digital to Analog Converter and Offset Calibration

To extend the measurement range through common-mode subtraction, the AD7746 contains two digital to analog converters or CAPDACs[1]. While the dynamic range of measurement for the CDC is -4.096 to +4.096 pF, a common-mode modifier CAPDAC enables the chip to measure up to 21pF. As demonstrated in Figure 5-3 the CAPDAC value is internally subtracted from the test capacitance before the signal is fed to the CDC. This shifts up the effective range of the CDC by the value of the CAPDAC. The published range of the CAPDAC is 0pF to approximately 17pF.

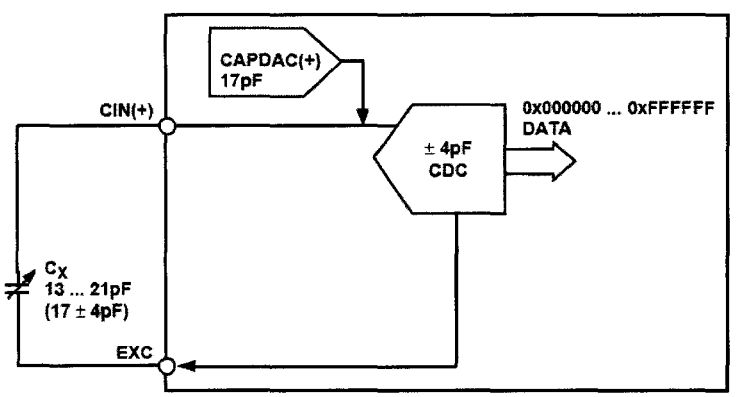

Figure 5-3: The AD7746 DAC [28]

For example, if an active range of 5 to 9 pF is desired, by setting the CAPDAC to 6pF the effective range is shifted up to 2 to 11pF covering the desired range. Any value

[1] CAPacitive Digital to Analogue Converter will be referred to as the CAPDAC or the DAC interchangably.

below the minimum of 2pF results in a negative -4.096 value and values larger than 10pF return +4.096. While the CDC is capable of measuring what is stated to be a negative capacitance, this is only possible in the differential mode where one input is negated. No truly negative capacitance is measured by the system as this is an algebraic concept. Therefore the value of the capacitance being measured is:

$$C_{measured} = C_{CDC} + C_{DAC} \tag{5.3}$$

where C_{DAC} is the value of the DAC in Farads as opposed to a binary setting

Knowing that the CAPDAC is software accessible, in theory the measurement range of the system is 0-21pF An active offset adjusting scheme could be used to modify the offset until the measurements are in the range. However the re-initialisation of the device requires up to 50ms. The 8pF CDC range covers approximately a third of the extended range of 21pF The worst-case scenario will require re-adjustment of the CAPDAC twice and three measurements. This will result in an unacceptable sampling period of at least of 20+50+20+50+20=160ms. Figure 5-4 lists the steps needed to measure an exemplary 19pF value.

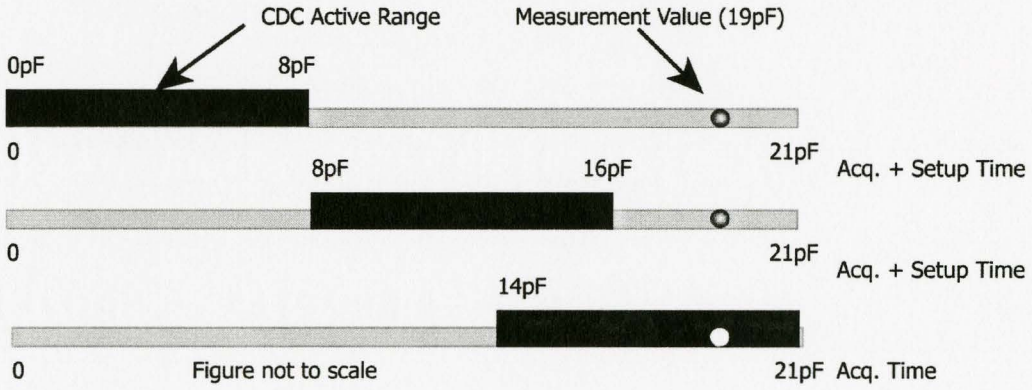

Figure 5-4: Active CAPDAC worst-case search

As seen, the extended range scheme is substantially slower than the standard acquisition time and hence the real-time applicability of the system is adversely affected. For this reason the value of the DAC will be digitally set only during the initialisation phase in this thesis . This is set as 7-bit number. The eighth bit (MSB) is to turn the CAPDAC on or off. The 7-bit number is linearly scaled from zero to full range. Considering Equation (5.3), it is therefore desirable to find the value of the CAPDAC in Farads. The next section describes the methodology used to calibrate the CAPDAC.

5.4.1 Offset Calibration

To measure the absolute value of capacitance it is required to find the full range of the CAPDAC. The AD7747 documentations specify that the full range of 17pF is not calibrated and variation of up to ±20% should be expected. To improve the accuracy of the measurements, the CAPDAC was calibrated with respect to the CDC measurements. Hence, the accuracy of this calibration is dependent on the trueness of the CDC readouts. As previously brought up, due to the limited range of the CDC compared to the DAC, no single set of calibration data could exist that would cover the entire range of the DAC. To calibrate against the main CDC with a non-changing capacitor, only the lower end of the CAPDAC range could be used. That is to say, if a valid reading is to be obtained with the maximum value of the DAC, no reading could be acquired with the DAC close to zero or disabled. Similarly, when valid readings could be obtained with the DAC off and/or smaller DAC values, the larger values would lead to an under-range reading of -4pF[1] and therefore no valid reading could be obtained. Figure 5-5 illustrates the effect of the DAC

[1] The exact value is -4.096pF however for clarity of the text -4pF is used.

for a 9pF test capacitor. The two flat ends indicated a saturated converter and therefore invalid results. In this example, the DAC could not be set to lower than 4pF and higher than 13pF. It is also obvious that no direct CDC reading without the DAC influence could be obtained. Ideally, with the DAC enabled and set to zero, no change in the reading should be noticed. It is evident from experiments that merely powering on the DAC changes the readings (setting the register to 0x80[1]). This could be caused by an offset-like effect of the DAC power or by the nonlinearity of the DAC. The difference would be that in the first case the DAC would always, and regardless of its actual value, would influence the reading by a constant value in addition to any the DAC settings. In the second case, the change is caused by a missing zero state or a nonlinear DAC behaviour and therefore no on/off offset exists. A linear regression best fit was used to minimise the error sum throughout the range. If the physical setup is not changed, it follows that for constant environmental conditions the capacitance is constant between two subsequent tests with different values of the DAC. If C_{CDC_x} is the readout from the chip for the X_{th} test, and C_{DAC_x} indicates the capacitive effect of the DAC for the test, the following condition must hold true:

$$C_{true} = C_{CDC_1} + C_{DAC_1} = C_{CDC_2} + C_{DAC_2} \tag{5.4}$$

where C_{true} is the capacitance of the test subject. If the fractional value of the DAC register in its on state is defined as V_r, the linear DAC could be modeled as:

$$C_{\mathrm{DAC_x}} = \beta + \alpha V_r \tag{5.5}$$

[1] Binary value of 1000,0000

where β is the offset of the line of the best fit and α is its slope. From Equations (5.4) and (5.5) it is deduced that:

$$\begin{aligned}(\beta + \alpha V_{r1}) + C_{CDC_1} &= (\beta + \alpha V_{r2}) + C_{CDC_2} \\ C_{CDC_1} - C_{CDC_2} &= \alpha\,(V_{r2} - V_{r2}) \\ \alpha &= \frac{C_{CDC_1} - C_{CDC_2}}{V_{r2} - V_{r1}}\end{aligned} \tag{5.6}$$

with β found from $V_r = 0$. The calibrated measurement is then obtained using:

$$C_{measured} = C_{CDC} + \beta + \alpha V_r \tag{5.7}$$

But it is desirable to use the entire range of the DAC and more than two calibration points. To this end, a method has been developed to synthetically extend the range of the CDC using the DAC and improve the calibration. The problem will be further explained graphically first. Figure 5-5 is a plot of the theoretical expected outputs from the CDC unit with varying DAC values. For the same test, increasing the DAC value will result in a lower readout until the point of negative saturation.

To extend the range, it is possible to shift the lines for 9pF and 15pF in Figure 5-6 to be in line with the line of the first sample. Because the calibration test capacitors are not of exactly known values, it is not permissible to use the nominal difference to shift the data. Yet if the data series are made to overlap, the overlapping points for a given value of the DAC indicate the difference between the test subjects without relying on the exact value of the DAC. Graphically speaking, the valid (sloped) range of the 9pF data series is shifted down and is aligned with the data from the 3pF series.

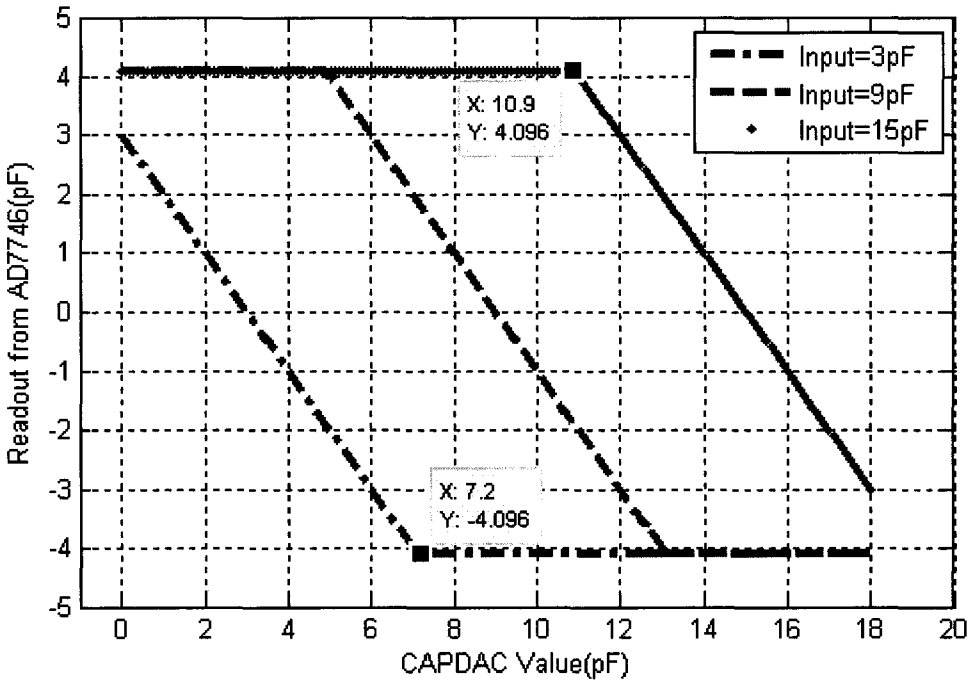

Figure 5-5: Theoratical CDC readout and the C_{DAC} value for 3 test capacitors

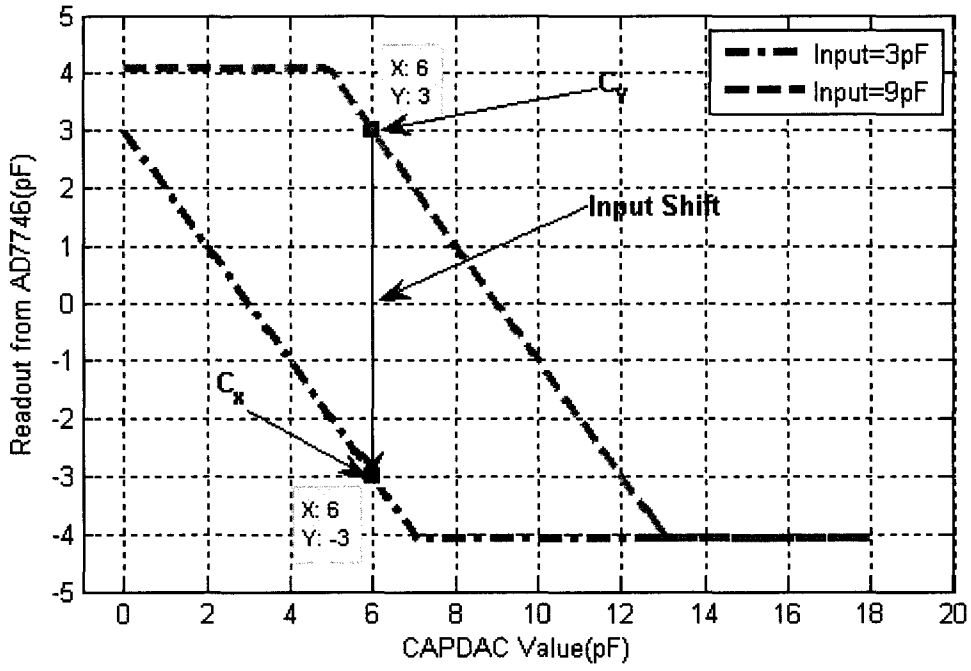

Figure 5-6: Calibration line shift

It must be true that:

$$C_x = C_{CDC_1} + C_{DAC_1} \tag{5.8}$$

$$C_y = C_{CDC_2} + C_{DAC_1} \tag{5.9}$$

therefore for an unchanged DAC value:

$$\Delta C = C_x - Cy = C_{CDC_1} - C_{CDC_2} \tag{5.10}$$

Using ΔC the data sets extending the range to the right could be shifted and aligned. Because ΔC is independent of the absolute value of the DAC, the synthesised calibration set is as accurate as the CDC. In practice 10 sample points were recorded and ΔC was calculated as the average of the all ten. While the DAC is utilised to perform the measurement in the calibration, its exact value is not part of the calibration process. With the data from the synthesised range, linear regression is used to find the slope. Because the horizontal axis has a range of 1.0, the slope is the full range of the DAC. Figure 5-7 shows the calibration line and the calibration data. For this particular chip, $\alpha = 18.33pF$, $\beta = 0.4pF$, an $R^2$of 0.9999≅1.00 was achieved.

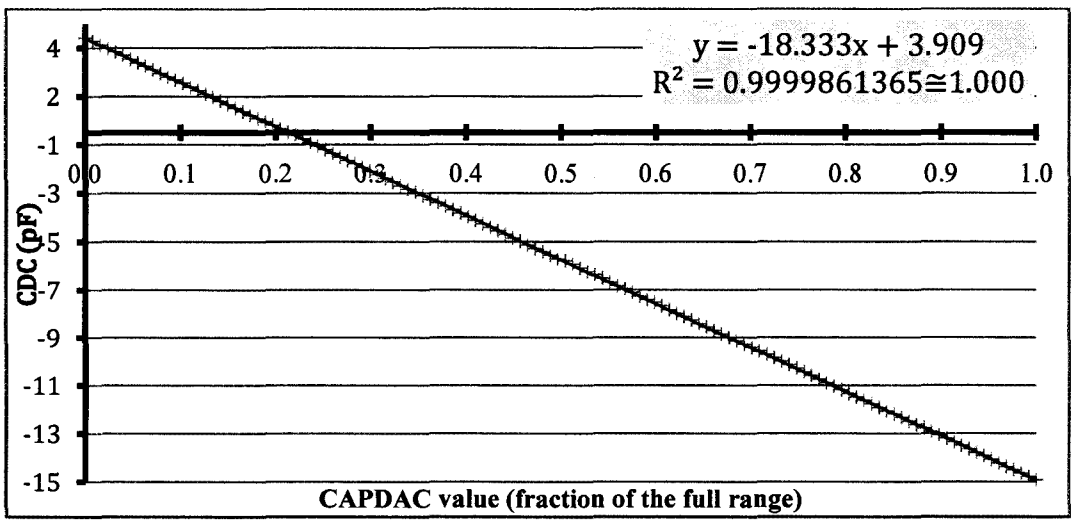

Figure 5-7: Extended CDC readout vs. CAPDAC

The offset is dependent on the test capacitance initially used. This test capacitance is in the range of the CDC and is therefore found by turning the DAC off. The difference between the measured capacitance and the y-intercept of the line is the offset of the line of best fit for the DAC.

As expected this calibration process is specific to each individual chip. If a device is to be used for absolute measurements, the calibration must be repeated. For collision avoidance applications, this calibration process is only necessary if the AD7746 in use must be replaced without repeating the training process as will be discussed in Chapter 6. This calibration process can be avoided if the user performs the training procedure since the CAS functioning only depends on the relative[1] (and not the absolute) capacitance values.

5.5 Data Quality

Before any statistical analysis of the active system can proceed, it is desirable to establish the quality of the static data. Table 1 indicates that the effective resolution of 15 bits is expected, which translates to a 200aF accuracy. Yet the sample data collected from the system indicated that a higher level of noise is present. In this section, the variance of the data for fixed electrodes under static and semi-active conditions are analysed. The first case is the electrodes held by a plastic fixture (shown in Figure 5-8). The other two cases involve the electrodes held by an unpowered robot and a powered robot (shown in Figure 5-9). In all cases, the system is subject to no intentional external disturbance; and

[1] Relative to the time of training

the electrode size, and air-gap are unchanged. The data is collected at a slower rate[1] of 20Hz. The empirical results indicate that without further filtering no more than two decimal points (0.01pF) is reliable.

The value of the capacitance is directly dependent on the distance between the two plates and therefore any vibration is expected to increase the variance. The fixture in Figure 5-8 is directly between the two plates and therefore is largely resilient to vibrations of the worktable. However if the electrodes are on two different structures, namely a robot and a worktable, more vibration is expected (shown in Figure 5-9). This is confirmed by the sample data collected. Table 2 compares the results of the three tests. The size and the separation of the electrodes are similar Nonetheless the mean capacitance values are different due to the difference in the objects surrounding the electrodes. For example, the metallic grounded body of the robot has profound effect on the readout. In the case with the arm powered, the measurements displayed a higher variance. That can be attributed to the vibrations of the position-controlled joints of the arm.

Table 2:
Comparison of the measurement statistics for the electrodes held by the fixture, by an unpowered arm and by a powered arm

Condition	Fixture	Robot Off	Robot On
Sample Size	10000	1000	1000
Mean(pF)	1.302154	2.567555	2.55943
Median(pF)	1.302125	2.567552	2.55938
Variance(pF)	3.0e-7	8.9e-007	6.0e-006
Max-Min(pF)	0.0037	0.006	.0621

[1] Slower than the standard 50Hz (20ms)

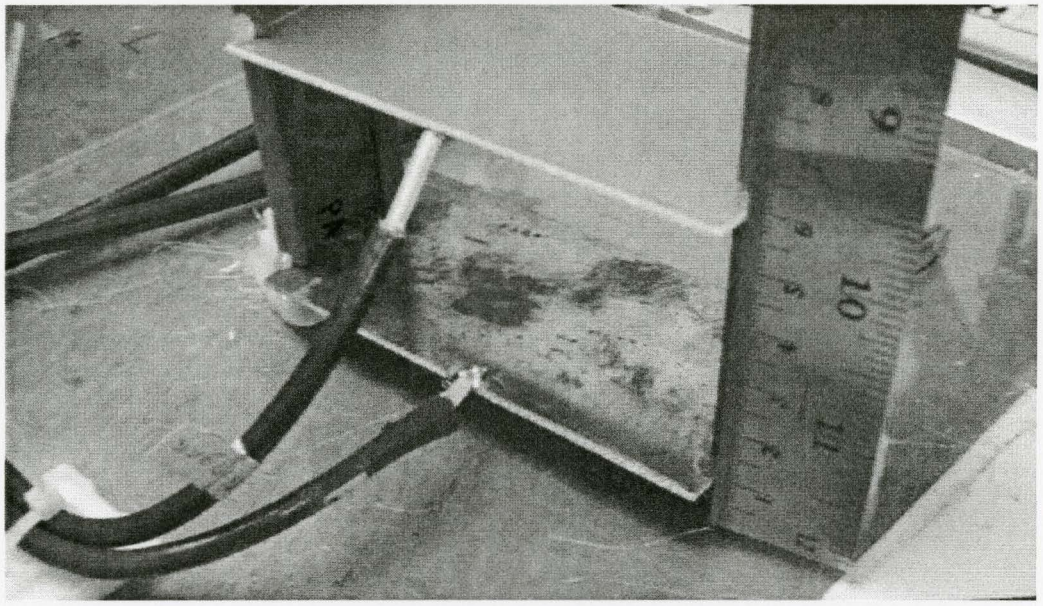

Figure 5-8: Fixed reference electrodes on fixture

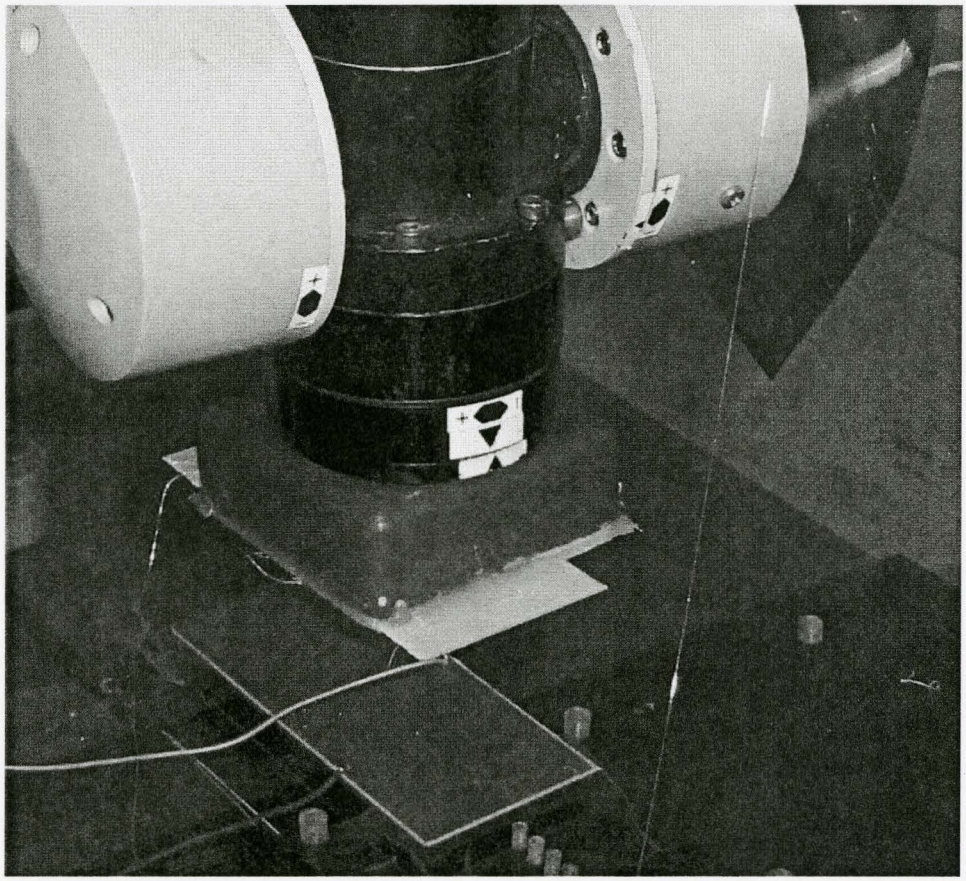

Figure 5-9: Electrodes on the robot and the worktable

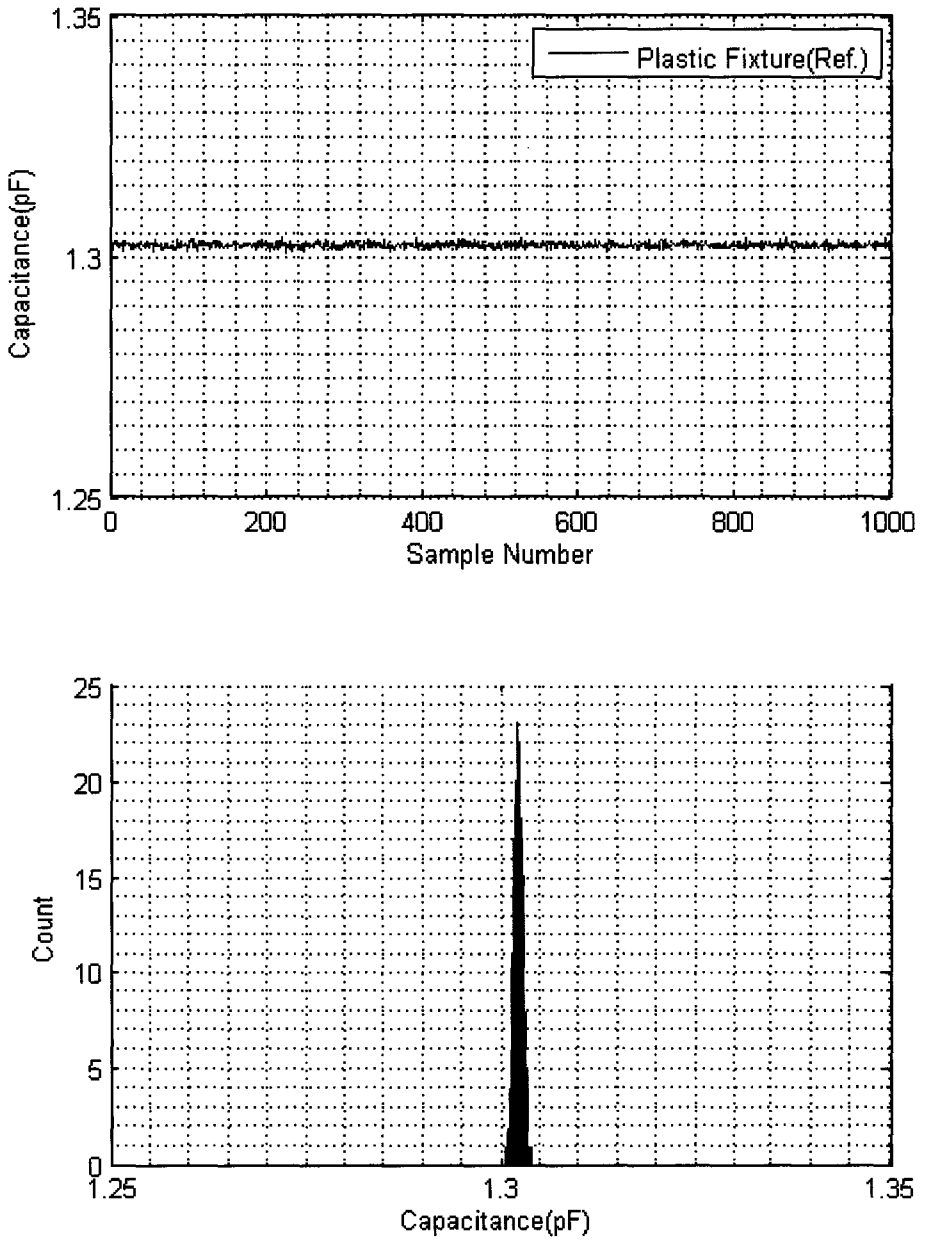

Figure 5-10: Plot of the capacitance values and their histogram for the electrodes held by the plastic fixture

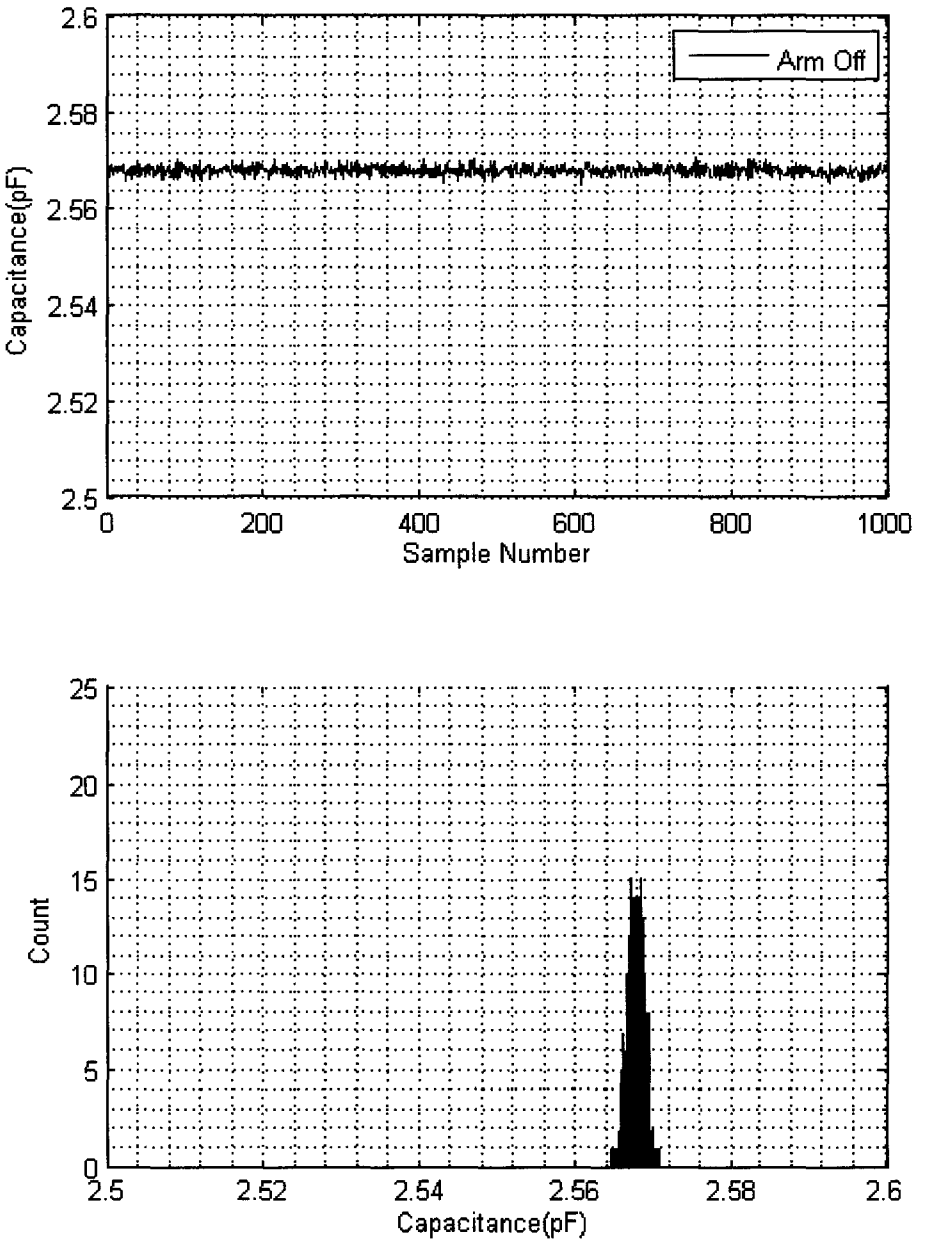

Figure 5-11: Plot of capacitance values and their histogram for the electrodes held by the unpowered arm

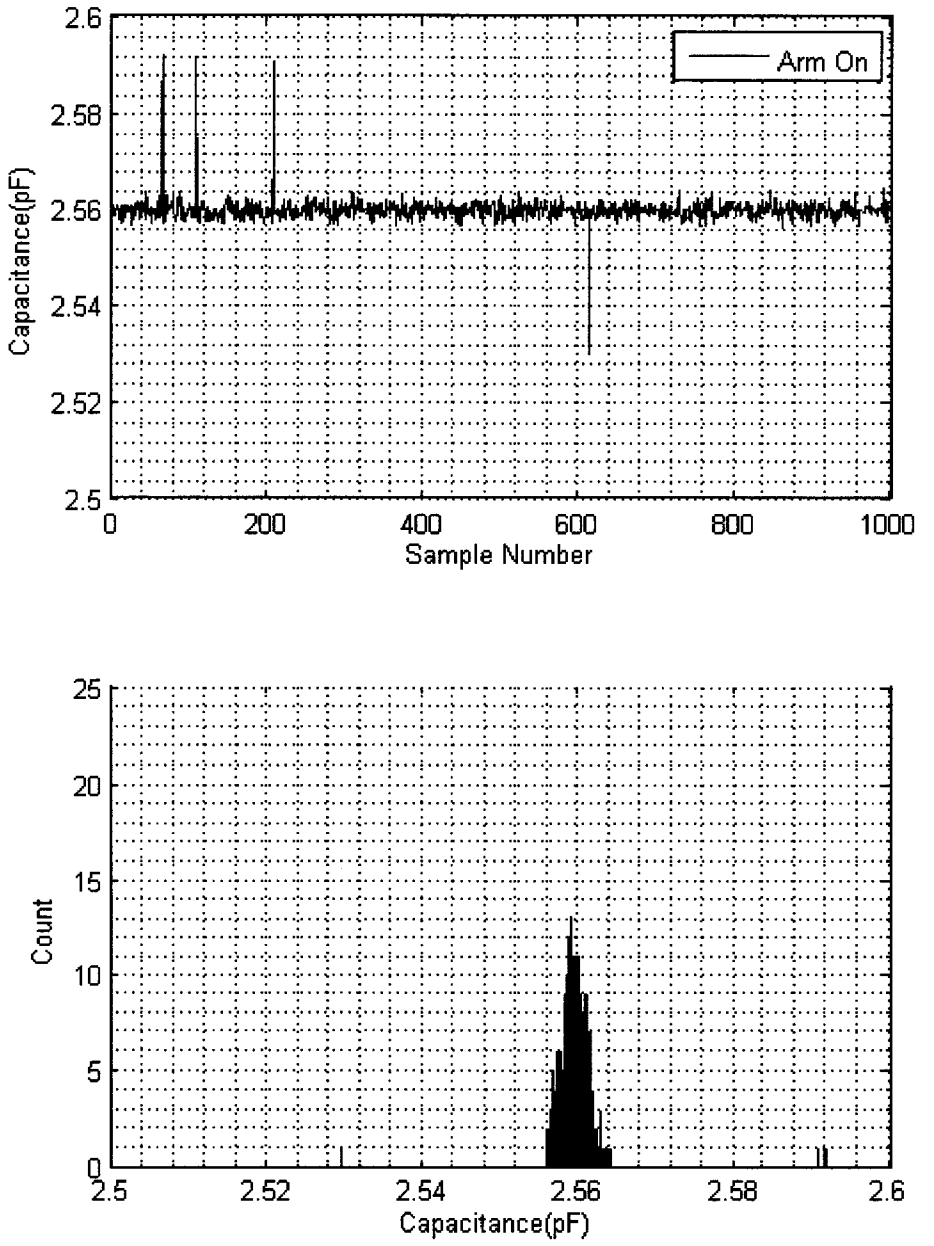

Figure 5-12: Plot of of capacitance values and their histogram for the electrodes held by the powered arm

5.5.1 Effect of Cables

To avoid crosstalk between the cables and minimise the electrical disturbance along the cables to the electrode plates, coaxial cables have been chosen. The cable shielding is connected to ground. Therefore there is a parasitic capacitance to ground proportional to the length of the cable. As it was discussed in Section 4.7, large parasitic capacitance to ground will adversely affect the accuracy of the measurements. Table 3 lists the characteristics of the cables in use.

Table 3:
Electrical specification of the two coaxial cables in use

Type	Manufacturer	Part #	AWG	Impedance (Ω)	Capacitance (pF/m)	Core
RG-58 A/U	Belden	8259	20	50	101	Stranded
RG-58 A/U	Belden	82240	20	53.5	86.6	Single Strand

The most notable characteristic is the 101pF/m capacitance between the core conductor and the shielding. Figure 5-13 and Figure 5-14 show the published performance degradation of the AD7746 for the increasing parasitic capacitance to ground. It could be seen the device is more sensitive to capacitance between the CIN pin and ground compared to the EXC and ground. The documentation suggests a maximum of 60pF between CIN and ground and a maximum of 100pF between EXC and ground. The experimental results for varying cable lengths from 50cm to 6m are shown in Figure 5-15. At the length of 6m, the cable capacitance should be 600pF. For the CA application the length of the cable will be constant and this error will not affect the relative capacitance, hence the cable effect will not hinder performance.

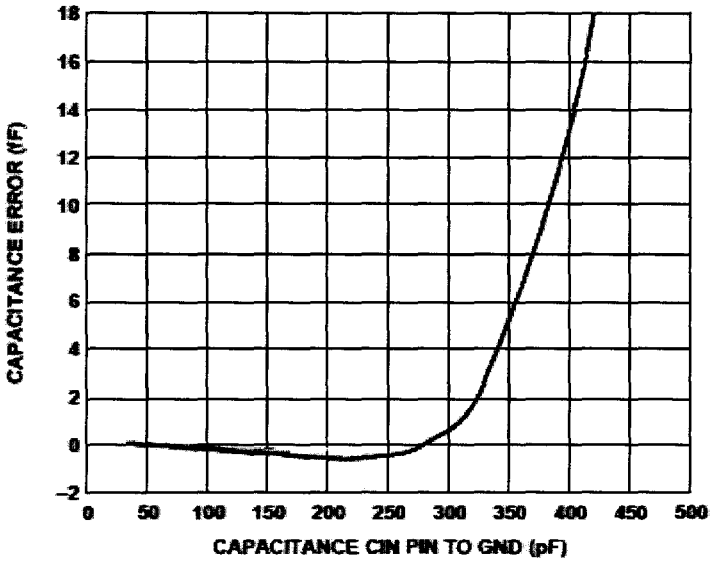

Figure 5-13: Measurement error in femto-Farad versus CIN-Ground capacitance at 5V supply

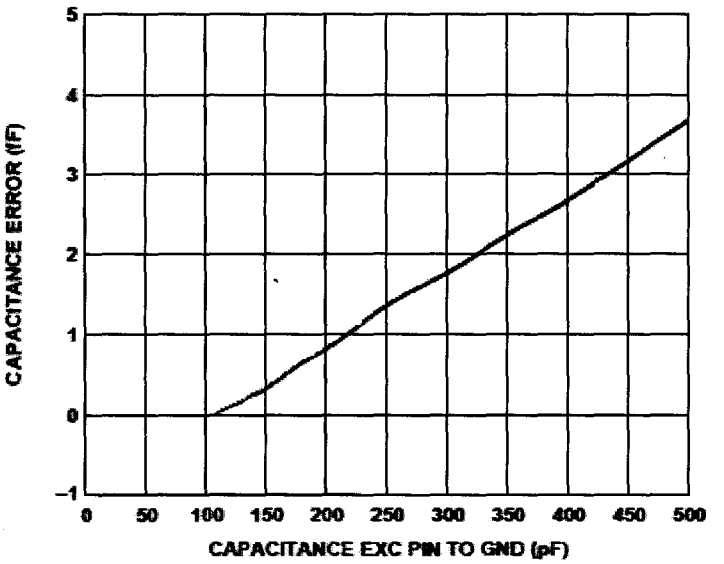

Figure 5-14: Measurement error in femto-Farad versus EXC-Ground capacitance at 5V supply

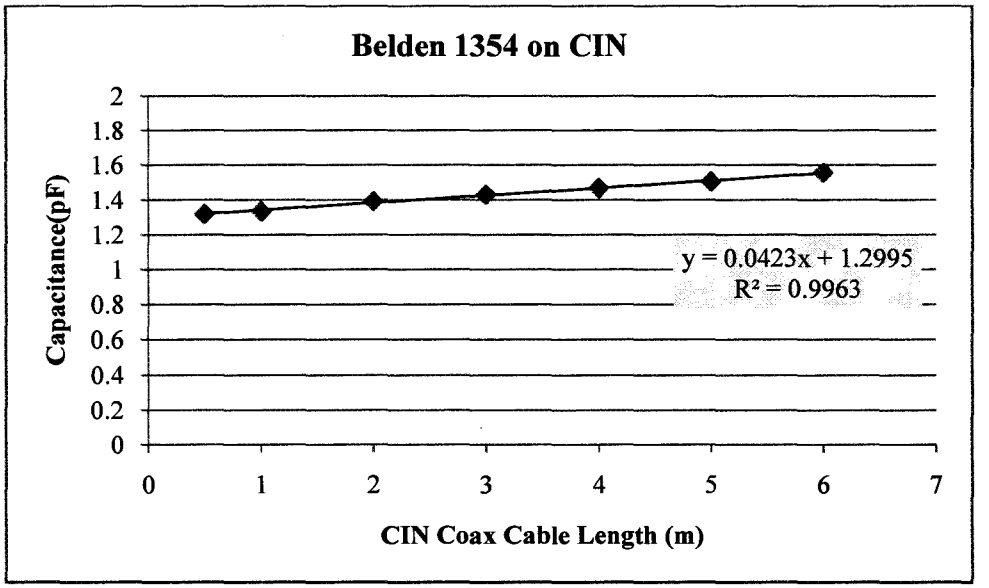

Figure 5-15: Measured value of an unchanged test capacitance for increasing cable length connected to CIN

5.6 Hardware for Multiple Electrode-pairs

To provide a more effective protection and to direct the sensitivity of the system to the more susceptible areas, the use of more than one pair of electrodes is desirable. The benefits of this approach were discussed in more detail in Section 4.6. The hardware implementation is examined here. Novak and Feddema [18] use frequency modulation to distinguish channels that are active simultaneously. Different electrodes pairs with the possibility of crosstalk use different frequencies and a filtering layer is responsible for the isolation. It is noted that Novak and Feddema resorted to a custom-built measurement system with no absolute reading. However this is not possible with any of the commercial chips accessible. Although the AD7746 provides two channels, it is in essence a single channel CDC. The channel selection requires the time-intensive process of re-initialisation. It is also incapable of supporting more than two electrodes. Two alternative methods are hereby investigated.

5.6.1 Multiplexing Scheme

A multiplexing circuit that enables fast software controlled connection to an array of sensors has been developed by the author, Y. Ma (a former Master's student) and Dr. Gary Bone (Professor and supervisor). The multiplexing circuit switches between 16 separate EXC and CIN channels (32 in total). The channel selection is done by the supervisor PC.

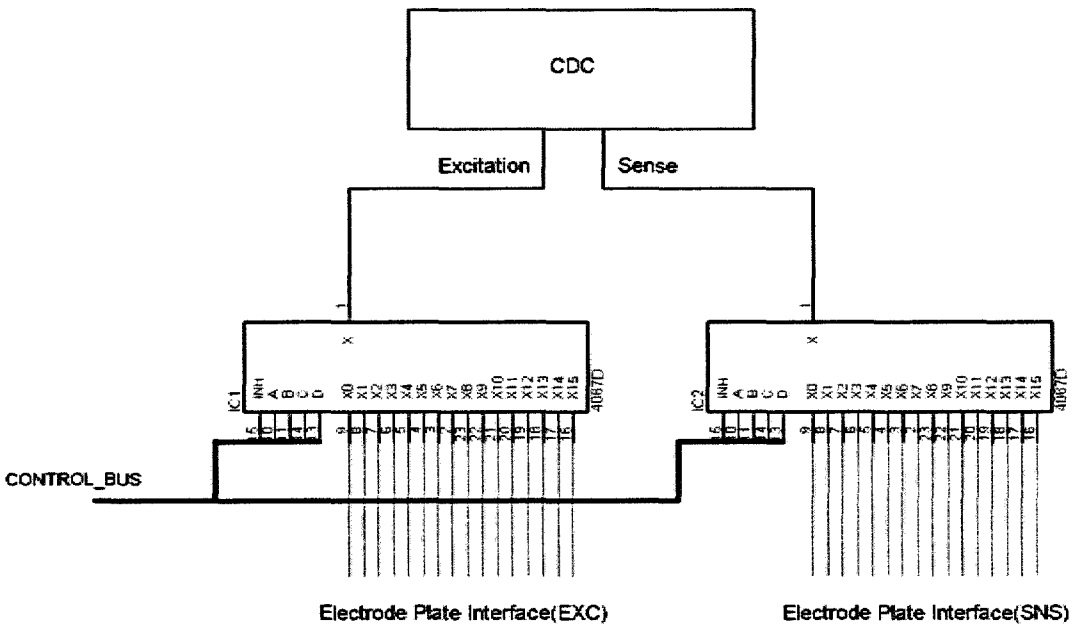

Figure 5-16: Electrode Multiplexing Hardware

Figure 5-16 shows the multiplexing hardware in relation to the CDC chip. This setup requires active selection of the target electrode channel. The measurement chip is unaware of the switching and therefore the channel switching could happen while a measurement is in progress. To maintain the reliability of the measurements the settling time of the multiplexing circuit and the transient time of the AD7746 must be respected,

so the sampling time possible with this scheme is relatively long. This time issue will be examined further in Section 5.6.3.

5.6.2 Multiple Chip Scheme

Preliminary testing indicates that it is possible to use more than one active AD7746 chips at a time. However due to the shared modulation frequency the possibility for crosstalk between the electrode-pairs cannot be ruled out. As well the electrode-pairs would be fixed. With a multiplexer the electrodes could be interweaved resulting in more combinations than with chip-per-pair as shown in Figure 5-17 for a four-electrode case. In this example the chip-per-pair scheme could measure two capacitances while the multiplexed system can measure four.

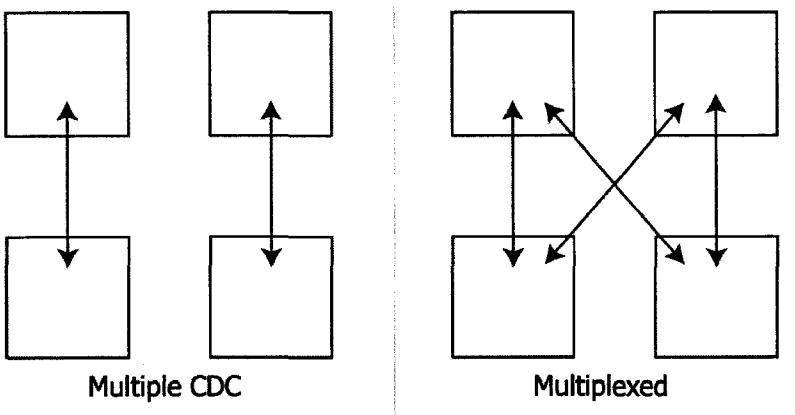

Figure 5-17: Chip-per-pair scheme (left) compared with multiplexed scheme (right)

Furthermore, the AD7746 does not provide a full I^2C interface meaning that not more than one device could be used on the serial bus and the PC interface would require further expansion for every chip, making it less appealing. However, the chip-per-pair setup will provide a faster sampling rate than the multiplexing scheme. .

5.6.3 Effect of Multiplexing on the Data Rate

Recalling Figure 5-16, it is seen that the switching time of the proposed multi-channel system is the sum of the multiplexer settling time and the time required for at least one complete measurement. While the transient time of the additional hardware in all cases is less than 500ns [34], the sampling period of the AD7746 must be greater than 11ms. As such, any analysis should focus on the transient of the CDC. To establish the transient and the maximum allowable sample rate for the multiplexing scheme, a series of tests were performed. The independent variable remained the delay between the switching instant of the external multiplexer and the moment the measurement is polled. In this experiment, the system switched between three electrode-pairs. Table 4 compares the readings. Although in some cases the mean value is close to the expected (labelled "*TRUE*" in the table), the peak-to-peak value should also be considered. That is because peak-to-peak is indicative of the jitter of the readings. When the transient of the system is not respected (*i.e.* for delays smaller than 20ms), the readouts are spread over a wider range. This fact is more evident in Figure 5-18. The values obtained through a sequence of switching, delay and reading for one electrode-pair is shown. With a delay of 20ms or more reliable readings are attained. The faster rates result in completely misleading values and/or the values with substantial jitter. In the case of no delay (0ms), the system appears to be validly measuring a different electrode. This indicates that the propagation through the chain has not reached the CDC. Figure 5-19 provides a graphical view of the measurement validity for the different sampling rates.

Table 4:

The effect of delay between the switching instant and the reading instant (all capacitance values in pF)

Switching to Reading Delay(ms)	Pair 1: Reference		Pair 2		Pair 3	
	Mean	Peak to Peak	mean	Peak to Peak	Mean	Peak to Peak
TRUE	1.31	.006	2.00		3.42	
0	3.383	2.11	3.383	2.118	3.373	2.118
12	2.019	2.112	1.651	0.698	2.668	1.443
15	1.625	1.610	1.886	0.625	3.136	1.274
17	1.372	0.739	1.971	0.338	3.344	0.701
20	1.315	0.005	2.005	0.019	3.425	0.034
25	1.314	0.004	2.006	0.017	3.426	0.012
50	1.314	0.004	2.005	0.015	3.426	0.010

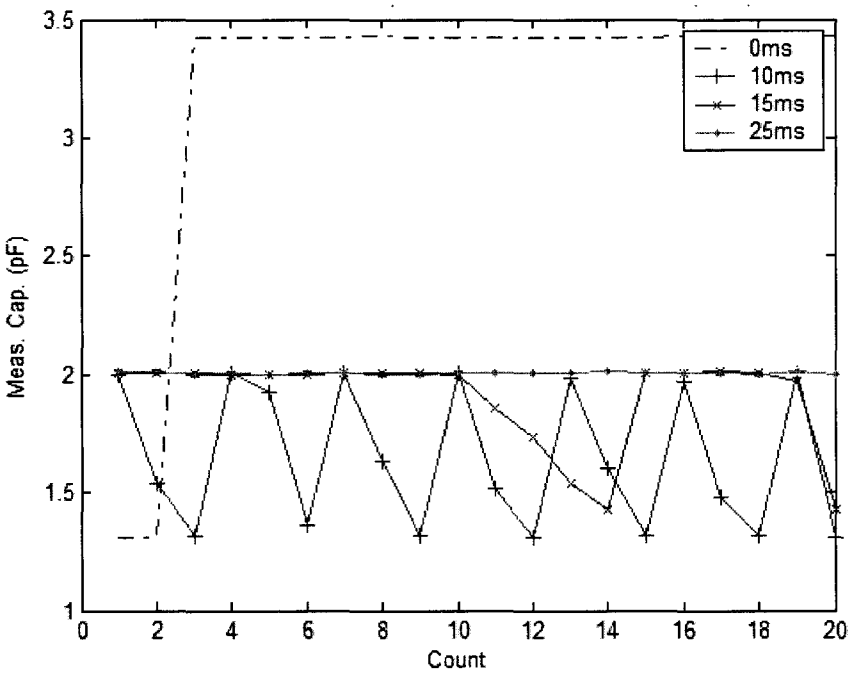

Figure 5-18: The delay between the switching instant and the reading instance with the multiplexer setup

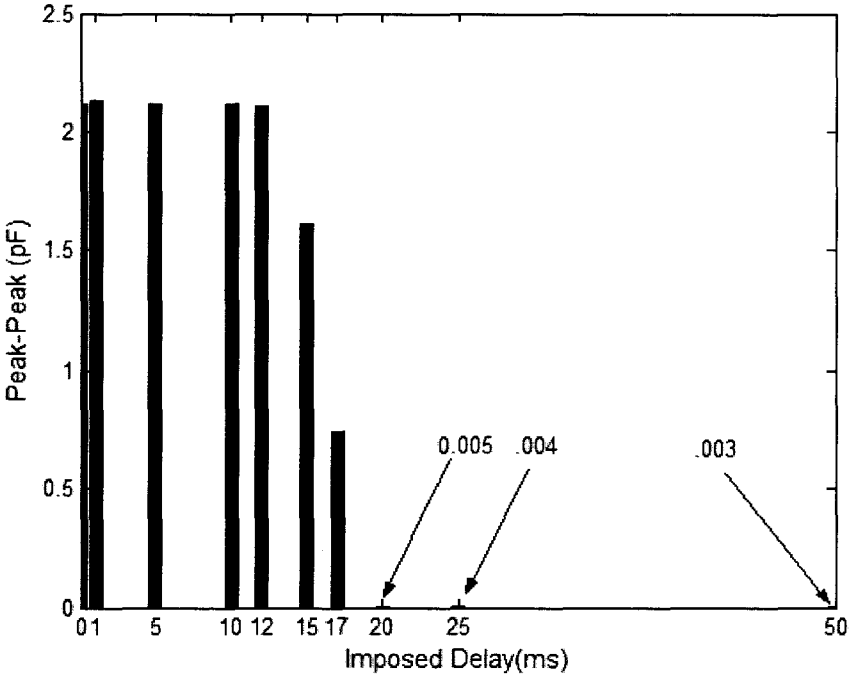

Figure 5-19: Peak-to-Peak value for different delays

While the expected value is approximately 2pF, at the published acquisition time of 11ms, more than 2pF of variation is seen. It is reasonable to assume that any delay less than 20ms results in an unacceptable signal jitter and each added electrode-pair will add 20ms to the sampling period. That could be explained by the fact that since the switching and sampling are not synchronised, the first measurement after switching is corrupted and a second measurement needs to be completed. Therefore up to three measurement periods are necessary.

5.7 Changing Dielectric Constant

Recalling Equation (3.13), repeated in (5.11), it is observed that the capacitance is proportional to the dielectric constant of the medium, ε:

$$C = \frac{Q}{V} = \frac{\int_s \varepsilon \vec{E} \cdot d\vec{s}}{\int_{p_1}^{p_2} -\vec{E} \cdot dl} = \varepsilon \frac{\int_s \vec{E} \cdot d\vec{s}}{\int_{p_1}^{p_2} -\vec{E} \cdot dl} \tag{5.11}$$

The electric field between a sensor pair primarily travels through air. Others [33,I32,I19] agree that humidity and temperature amongst other ambient factors change the dielectric of the air. This could result in a shifted signature profile for a robot motion although no geometric change has occurred. Table 5 compares different readings over a span of time for the electrodes in Figure 5-8. There was no change to the electrodes arrangement. To minimise the effect of noise, each value is the average of 100 readings.

Table 5:
Changes in capacitance of a fixed electrode over time

Date and Time	Mean Value(pF)
2008-02-04 03PM	1.291
2008-02-05 03PM	1.291
2008-01-13 10AM	1.259
2008-02-05 05PM	1.291
2008-03-25 06PM	1.302
2008-03-31 05PM	1.372
2008-03-31 07PM*	1.317

***The electrodes were locally heated**

For a fixed electrode in a static setting, measured at two different instances:

$$C_{reference}\ (t = t_1) = \varepsilon_1 \frac{\int_s \vec{E} \cdot d\vec{s}}{\int_{p_1}^{p_2} -\vec{E} \cdot dl}$$

$$C_{reference}\ (t = t_2) = \varepsilon_2 \frac{\int_s \vec{E} \cdot d\vec{s}}{\int_{p_1}^{p_2} -\vec{E} \cdot dl} \tag{5.12}$$

the normalising ratio of the environmental effects is:

$$\frac{\varepsilon_1}{\varepsilon_2} = \frac{\varepsilon_2 \frac{\int_s \vec{E}.d\vec{s}}{\int_{p_1}^{p_2} -\vec{E}.dl}}{\varepsilon_1 \frac{\int_s \vec{E}.d\vec{s}}{\int_{p_1}^{p_2} -\vec{E}.dl}} = \frac{C_{reference}\ (t = t_1)}{C_{reference}\ (t = t_2)} \tag{5.13}$$

Therefore the signatures created at time t_1 could be compared with the signature created at time t_2:

$$C(t = \mathrm{t}_2) \times \frac{C_{reference}\ (t = \mathrm{t}_1)}{C_{reference}\ (t = \mathrm{t}_2)} \equiv C(t = \mathrm{t}_1) \tag{5.14}$$

where ≡ denotes the collision avoidance comparison.

The practice deviates from the above argument in case where the electric field travels through non-conductive elements other than the air. In those areas, the dielectric is not a strong function of the ambient condition and remains mostly unchanged. For collision avoidance application, the overwhelming portion of the space of interest is air-filled. This is supported by the experiments performed by Ma [19].

5.8 Electrode Sizing and Design

The proper sizing and placement of the electrodes are crucial for ensuring a fail-safe protection of the workcell and the robots. In the design of the electrodes, it is important to maximise the sensitivity of the system to displacement. To this end, using the maximum dynamic range of the system is desirable[1]. With the aid of the CAPDAC, a common-mode of up to 13pF[2] could be tolerated. Figure 5-20 is an illustration of this.

[1] 8.192 pF, however 8pF is mentioned for clarity.
[2] 13pF is the minimum based on the published specifications of the chip.

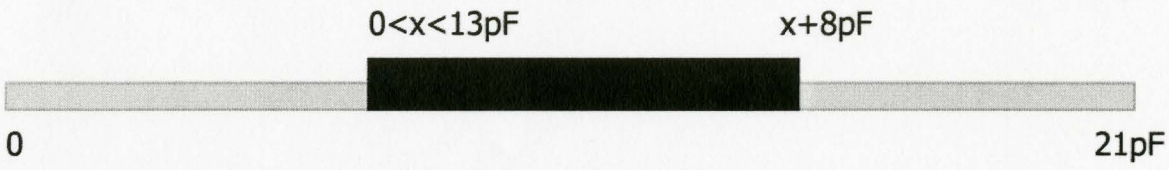

Figure 5-20: Dynamic range of 8pF over the entire range of 21pF

If the capacitive signature is to be entirely in the measurement range, the difference of the maximum and the minimum value for any pair must not exceed 8pF It is noteworthy that it is possible to have a saturated sensor at either end of the spectrum yet this practice limits the protection the system could offer The distance between the two electrodes is a function of the robots' motions and is therefore predefined for any particular collision avoidance scenario. If for a given electrode setup, the area of the electrodes is the constant, A, and the two extreme of distances are labelled d_{max} and d_{min}, resorting to the simple parallel-plate capacitor model in Equation (3.19) the following relationship can be established.

$$C_{max} - C_{min} = \varepsilon \frac{A}{d_{max}} - \varepsilon \frac{A}{d_{min}} = \varepsilon \times A \times \left(\frac{1}{d_{max}} - \frac{1}{d_{min}}\right) \quad (5.15)$$

$$A = \frac{(C_{max} - C_{min})}{\varepsilon \times \left(\frac{1}{d_{max}} - \frac{1}{d_{min}}\right)} \quad (5.16)$$

For $\varepsilon \approx 9\frac{pF}{m}$ [1]

$$A = \frac{8pF}{9\frac{pF}{m} \times \left(\frac{1}{d_{max}} - \frac{1}{d_{min}}\right)} = \frac{d_{min} \times d_{max}}{d_{min} - d_{max}}\left(\frac{1}{m}\right) \quad (5.17)$$

where d_{min} and d_{max} are functions of the motion. This is inaccurate for large gaps and is therefore only an approximate design guideline. The work by Xiang could accommodate

[1] ε of the free space is rounded to 8.854×10^{-12} F/m. This value has been approximated to 9pF/m and used as the permittivity of the air for the estimation.

the larger gaps and improve the accuracy of the estimation. Figure 3-8 repeated in Figure 5-21 indicates the results obtained using the Xiang method at a 2° angle and the experimental results for a pair of 10x30cm electrodes. The error increases as the distances is increased. The maximum error is small compared to the parallel-plate approximation.

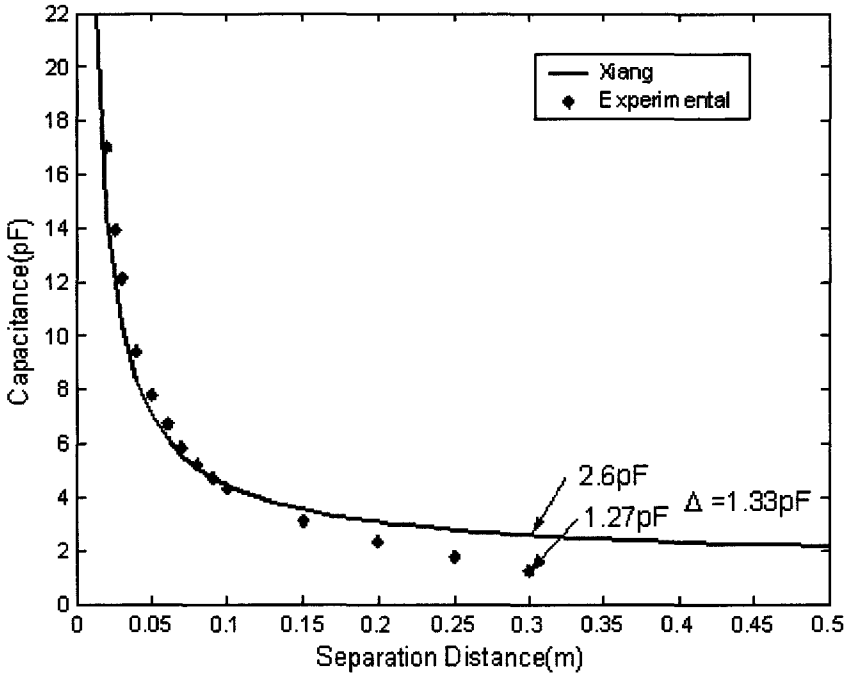

Figure 5-21: Comparison of Xiang's model with the experimental data for a pair of 30x10cm^2 electrodes

Using this method, the estimation of the electrode area could be further improved. To deduce the area the following parameters need to be established. Some of the variables are functions of the collision avoidance hardware and some are dependent on the particular workcell configuration.

The hardware parameters:

- $Range_{CDC}$: The active range of the measurement device
- CDC_{max} : The maximum allowed capacitance
- CDC_{min} : The minimum allowed capacitance

The workcell specific parameters:

- φ : The angle between the electrodes
- D_{min} : The minimum expected distance between the electrodes
- D_{max} : The maximum expected distance between the electrodes
- $Ratio$: The ratio between width and length of the electrode
- $Width_{min}$: The minimum allowable electrode width
- $Width_{max}$: The maximum allowable electrode width
- $Width_{inc}$: The incremental width step for the iterative solution

Equation (5.18) reiterates that the capacitance is a function of the area and the distance.

$$C = f(A, d) \tag{5.18}$$

Therefore knowing the active range of the sensor, the following relationship could be established:

$$C_{max} - C_{min} = Range_{CDC} = f(A, d_{\min}) - f(A, d_{\max}) \tag{5.19}$$

Although the inversion of the function $f(A, d)$ analytically to obtain A is problematic, numerical methods could be used to find a range of acceptable values. To this end, an iterative MATLAB code was developed. The algorithm is as follows:

1. Loop for $width$ from $Width_{min}$ to $Width_{max}$ at $Width_{inc}$ steps
2. $length = width \times ratio$
3. $A = width \times length$
4. $C_{max} = f(A, d_{min})$
5. $C_{min} = f(A, d_{max})$

6. $\Delta C = C_{max} - C_{min}$
7. Set the status of width to *"unacceptable"*
8. If $(C_{max} < CDC_{max})$ & $(C_{min} > CDC_{min})$&$(\Delta C = Range_{CDC})$ then

   set the status of width to *"acceptable"*
9. Increment $Width$ by $Width_{inc}$
10. If $Width < Width_{max}$

    then goto step 2
11. Display the results acceptable values for width and length

Figure 5-22 is an example of results. The desired ratio of width over length is a design parameter specific to each case. In this case the ratio is set to 5:1. It is found that with a width of 13 to 15cm, the entire range of the sensor is used while no saturation occurs. It needs to be mentioned that these are only approximate values for size of the sensor plates that would be directly facing one another. In this example a sweep of the electrode widths from 10 to 20cm is shown. Higher than zero *"acceptable?"* indicate acceptable points. C_{max} and C_{min} are the estimated values at the extreme ends. That is to say, for the given width what the expected values of capacitance would be for the defined minimum and maximum distance of the two electrodes. Δ_C is the difference between C_{max} and C_{min}.

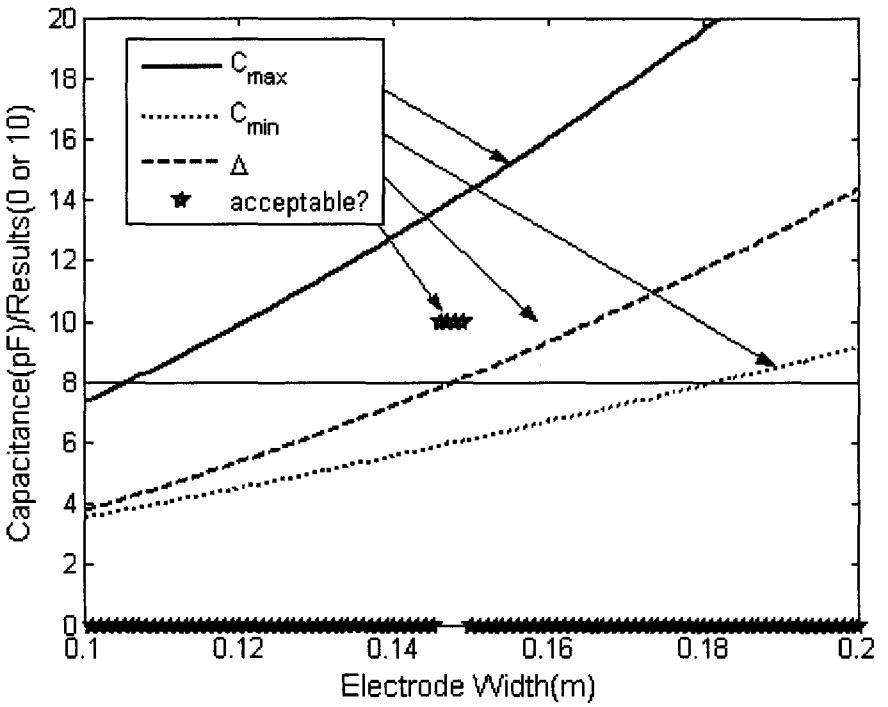

Figure 5-22: Software suggested electrode widths

5.9 Conclusion

While a number of options exist for the capacitance measurement, the Analog Devices AD7746 provides a robust and precise measurement in a compact package. To extend the measurement range, the AD7746 uses a common-mode offset that is not factory calibrated. In this chapter a calibration method was proposed for the internal offset of the chip. The quality of data was analysed and baselines for the statistical work were established. To improve the collision avoidance coverage, a multi-electrode scheme and the required hardware alternatives were discussed. The influence of this extension to the system, both in terms of sampling rate and the integrity of the data were empirically tested. The effects of the cable capacitance on measurement error were analysed. As it was previously discussed the changing dielectric constant of the air could threaten the

stability and robustness of the system. To compensate, a normalising reference electrode-pair was deemed necessary and the method proposed by Ma was adopted. Finally the issue of electrode design was also addressed. To facilitate this, a novel method to find the range of applicable electrode dimensions was created.

CHAPTER 6

The Signature and the Operational Boundaries

6.1 Introduction

In this research, a predetermined signature profile will be used to detect any abnormalities to ensure a safe operation. The use of training runs to obtain the profile will eliminate the need for any analytical or computer modeling of the environment. While major changes in the scenery are to stop the robot, the variations due to the normal operation must not hinder the operation. Small variations in the robot path from one run to the next, the physical vibrations of the arms and the measurement noise all contribute to the fluctuating capacitance values observed during normal operation. To warrant a robust system, this uncertainty is accounted for through the creation of safe operational boundaries. In other words, the signature of the motion does not need to equate to any one value but should be in a region or between two limits. This chapter describes the details of the data collection and the systematic determination of these boundaries with two goals in mind, effective collision avoidance and reliable operation. While training is an integral part of this process, all efforts will be made to limit the length of training for practical reasons including the cost of the required production downtime.

6.2 Overview of the Data Processing

The robot task sequence has been chosen to have a continuous progression of Joint 1 on the target CRS F3 arm. The data is stored in a multi-array file. Multiple sequences of the measurements for the position, the capacitance readings and the time for each sampling instant is recorded. The sampling is done at fixed intervals of 20ms as previously noted. The overall recording sequence is synchronised with the active robot. While the recording and the robot motion start at once, and the sampling is done every 20ms, the robot is not always at the same exact positions at each sampling instance. For example for two different trials, if the first position sampled is 1, the second sample position is 12 in one case and 14 in the other. While it is possible to enforce a position based sampling, this would violate the basics of collision avoidance and requires a hard real-time computing environment. Therefore the data storage was also designed to eliminate the need for this position-based sampling. The required data processing to create the final signature based on the position (or the cycle fraction) is performed in MATLAB. The position information is obtained by the externally mounted optical encoder described in Section 4.3.

6.3 Motivation for Operational Boundaries

From the physics of capacitance examined earlier, the value of the capacitance between two bodies is inversely proportional to the distance between them. Hence it is implied that for non-changing medium, an increase in the capacitance indicates contraction of the distance. Conversely, a decrease in the capacitance measured indicates widening of the space between the two electrodes. As such, only an upper bound is

necessary for the capacitive collision avoidance application. On the other hand, the imposition of a lower bound compels the system to detect all abnormalities. That is to say, a lower than expected signature indicates an unexpected incident. While this is not an indication of an impending collision, there exist useful cases of predictive behaviour resulting from the enforcement of the lower boundary If the cause of this lower reading is the absence of an object at an intended place, then the object could be occupying another space the robot is travelling to. An example is the case of a two-robot workcell where two arms leave their home positions to manipulate a workpiece. The first robot passes overtop of the second robot to perform a task on workpiece. Figure 6-1 is the top view of this hypothetical case. Robot A performs the initial task on workpiece C. Once finished it moves away from the Workpiece C and meanwhile Robot B passes on top towards the workpiece.

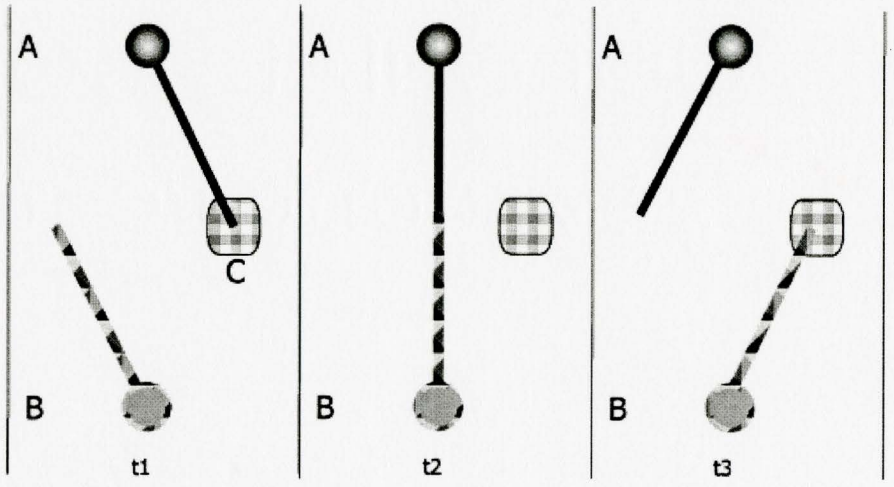

Figure 6-1: Top view of the normal operation sequence

Figure 6-2 shows the case where Robot A has not finished in time or otherwise failed to move away At time t_2, Robot B is passing the midpoint. With Robot A not underneath, the sensor reading is smaller and if not stopped a collision is likely at time t_3.

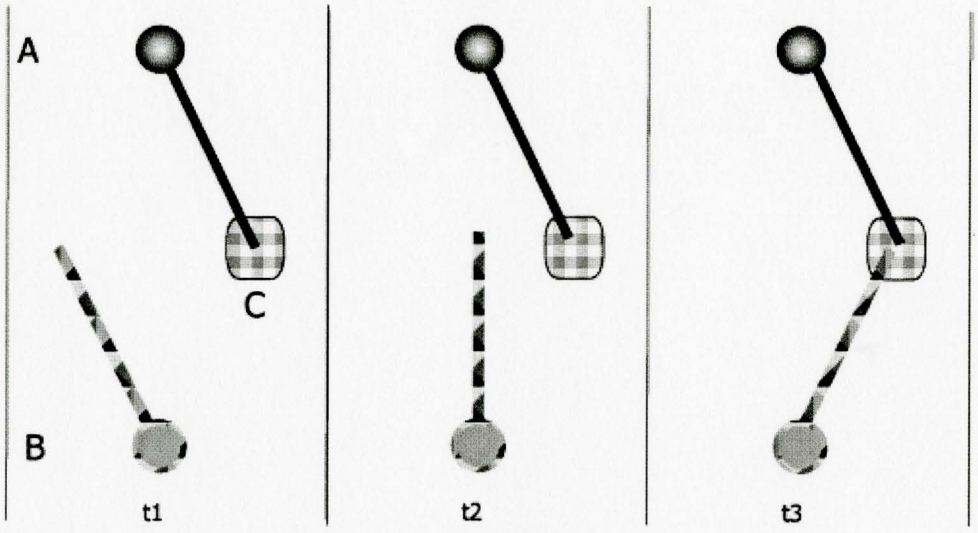

Figure 6-2: Top view of the failure case

The primary target environment for this research is the production environments in which the tasks are defined and deviations are not desirable therefore lower readings are as much cause for concern as the higher readings. Hence both boundaries will be used in this thesis. An inherent benefit of this approach is that sensor fault monitoring would be integrated into the system. If any connection to an electrode plate is disconnected, a lower-bound breach occurs making it fail-safe.

6.4 Sparse Sample Sets

As mentioned before, the sampling is done at fixed time intervals. This means that between the two samples the robot has completed a portion of its cycle for which no capacitance measurement exists. That results in many "empty" points along the arc-length. For a fixed sampling rate, the positional spacing between samples increases as the speed of the robot is increased. If encoders are used for the position, it is possible to lower the speed of the arms to the point where for every discrete point there exists a

measurement. Yet this results in impractically slow motion speeds. Therefore, it is necessary to develop an alternative approach as described in the proceeding sections.

6.5 Signature Generation

A signature profile to be used at runtime must contain an upper bound and a lower bound for every position possible throughout the cycle. Figure 6-3 is the profile of a sample run at the robot speed of 5[1]. The figure also shows a noticeable degree of jitter. Figure 6-4 shows another run with identical speed. The graph is zoomed in between the positions of 300 to 400. As shown, only nine sample points are captured. To enable the runtime system to operate at any speed, it is therefore vital to create a complete signature containing all the discrete points.

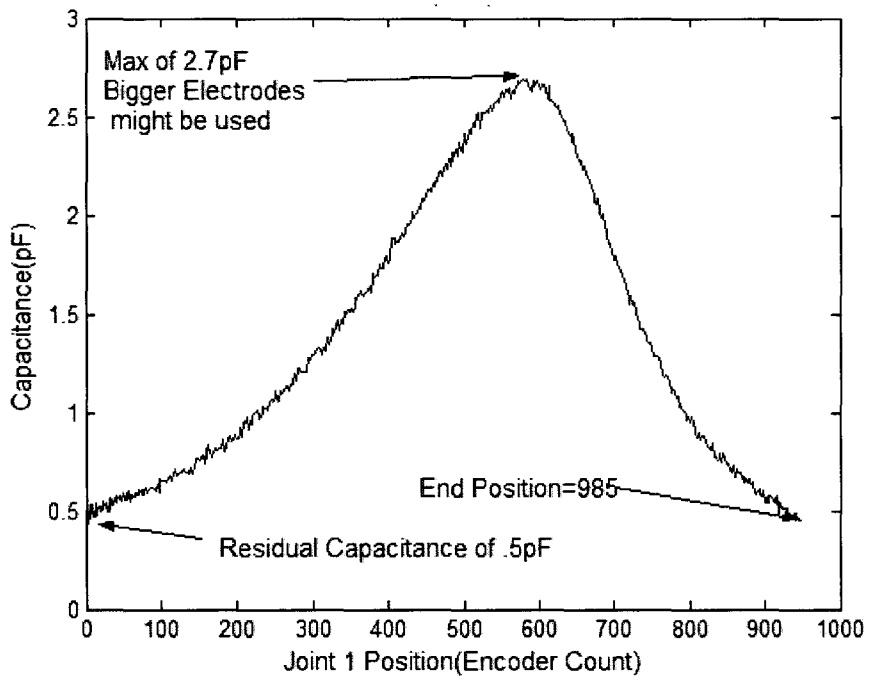

Figure 6-3: Sample run with the robot speed of 5.

[1] This number is the percentage of the maximum speed of the robot and is the only speed unit used by the C-500 controller.

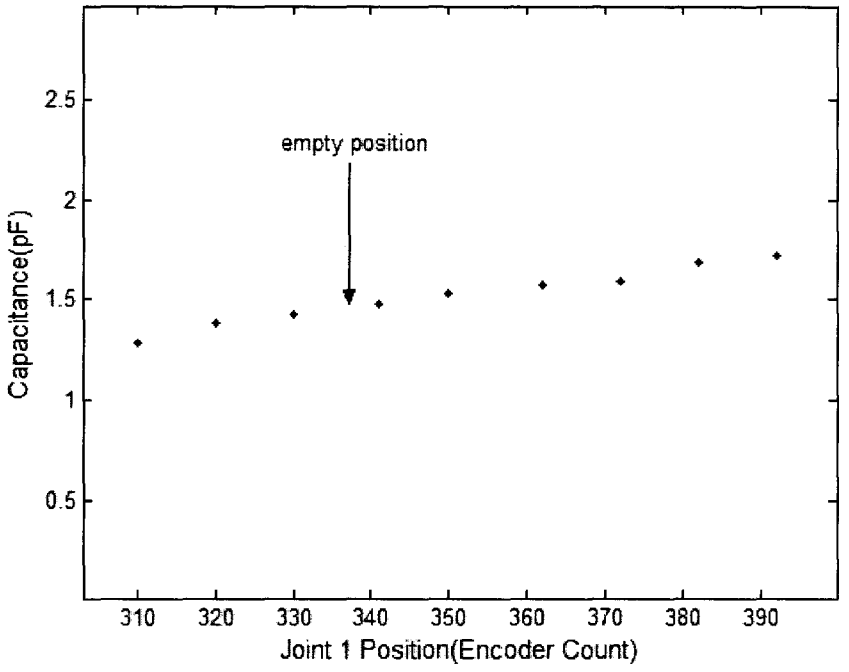

Figure 6-4: Close-up of Figure 6-3

Figure 6-5 illustrates two trials. The problem is further exacerbated by the fact that the runtime sampling is also inevitably asynchronous in position.

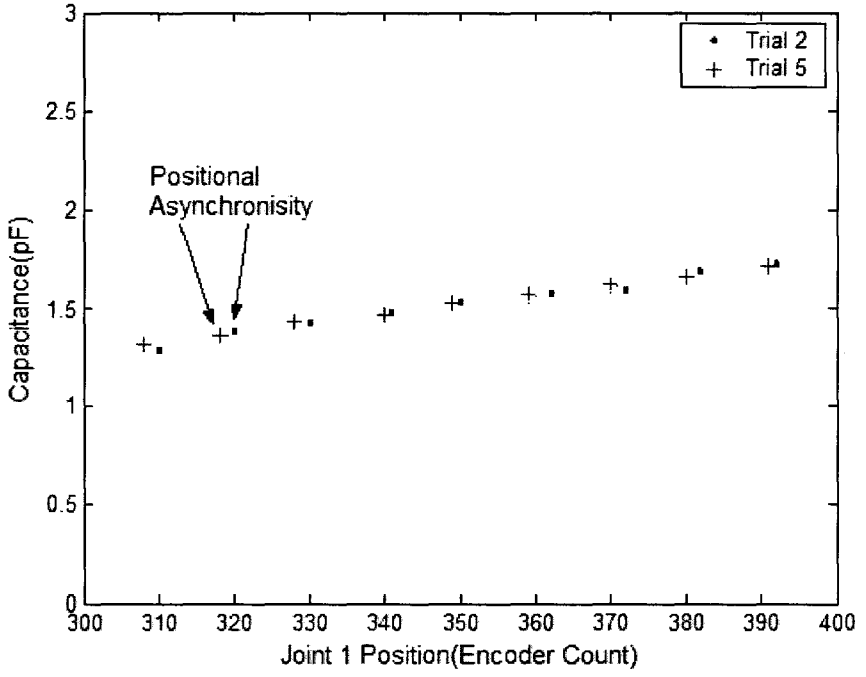

Figure 6-5: Asynchronous runs at the robot speed of 5

Therefore two hurdles must be overcome. One is the derivation of all the missing points. The second hurdle is establishing the operational boundaries for runtime use. While the static sensor data, as in Figure 5-10, exhibit a normal-like distribution, an arm in motion is not guaranteed to follow that trend. Therefore a non-parametric approach to the statistics will be pursued.

6.5.1 Repetitive Boundary Search

A primitive method to try to obtain the boundaries is to find the minimum and the maximum for every existing point. Figure 6-6 show the cloud generated by drawing the minima and maxima of the raw data. Figure 6-7 is a closer look. Because of the scatter of the positions for each sample, for the 10 trials, most points have only a single capacitive entry. If there is only one sample for a given point, that constitutes the average, the minimum, and the maximum and therefore meaningful boundaries cannot be found.

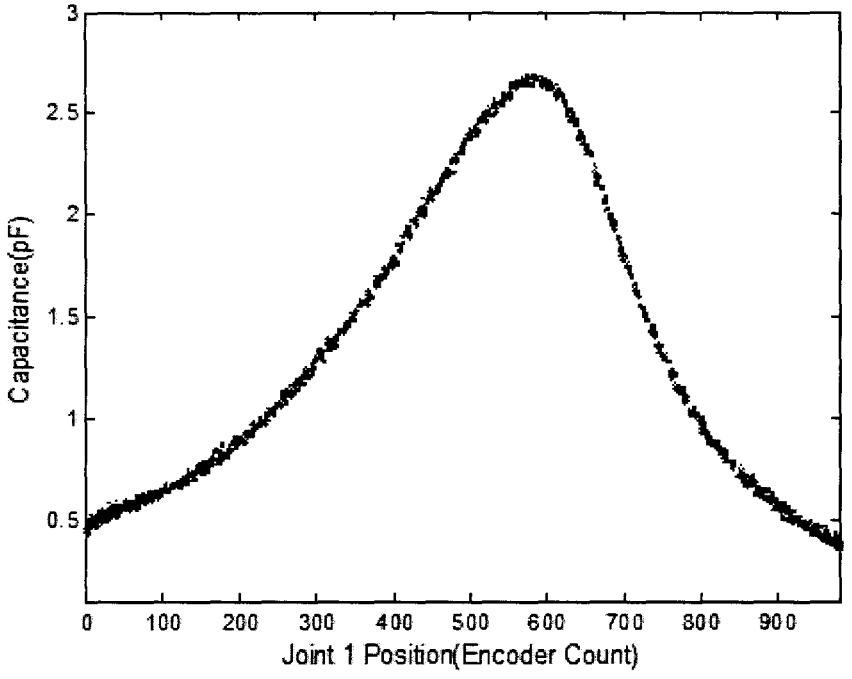

Figure 6-6: A normal run with min and max shown

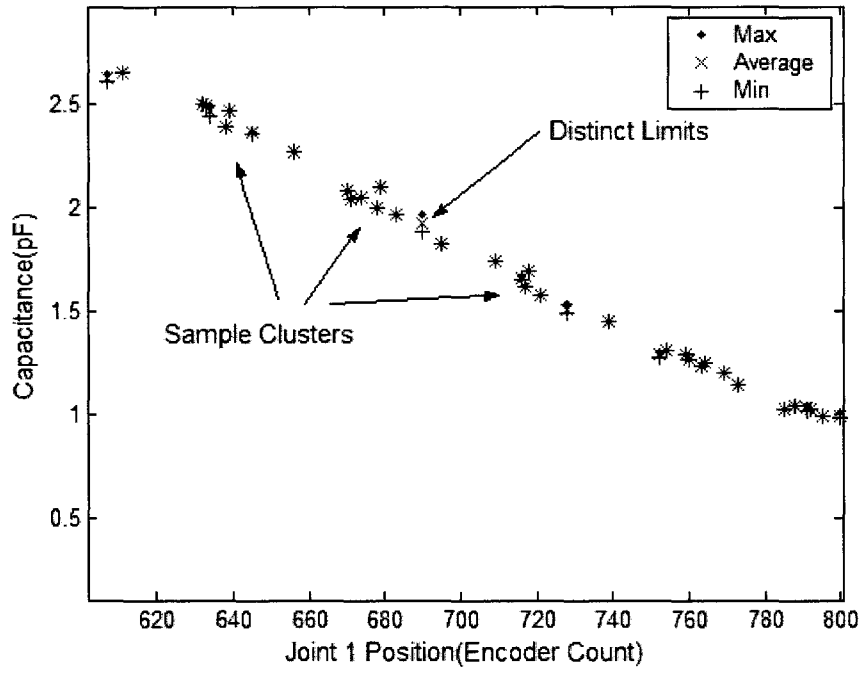

Figure 6-7: Zoomed of a standard run with min and max

To perform a meaningful statistical work, a larger number of points are required. Yet given the scatter, the number of the samples acquired for each point is substantially smaller than the number of the training trials. Hence, to achieve a reliable number of samples, a prohibitively long training time might be required. As already stated, this is not suitable for the industrial environments where the training time is expensive. Figure 6-8 is the histogram of sample sizes for a 50-trial training over a 980 count range. As expected, a large number of points do not include any information to form boundaries. Less than 10 samples are acquired for 95.5% of the points. To fulfill the stated objective of limited training time, alternative approaches will be investigated for construction of the signature profile.

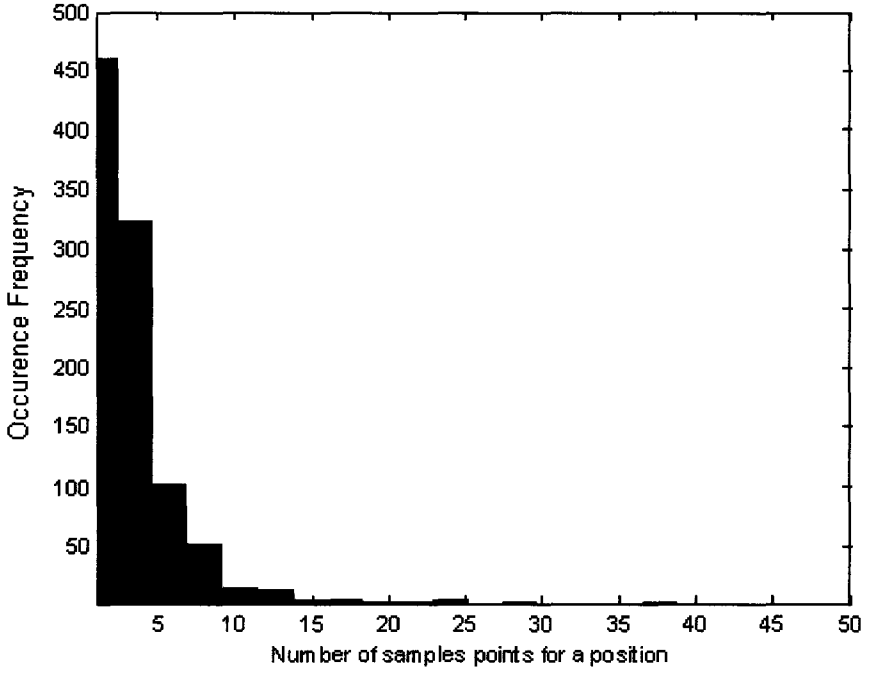

Figure 6-8: Histogram of sample sizes for each point

6.5.2 Linear Interpolation

The close proximity of the points suggests the potential for a linear approximation of the missing points. That is, the creation of a continuous profile through linear interpolation of the existing points. In essence, this method is dependent on the fact that any feature change in the profile is larger than the minute changes between two consecutive position points. The acquired data are denoted by "x" while the interconnection is the linear approximation. The concept of linear interpolation could be extended to the minimum and maximum points as found in the previous section. Nonetheless this method does not address the issue of small-sized or single entry points. Figure 6-9 is a close up of the upper and lower boundaries obtained by interpolating the maxima and minima of all trials. The problem remains that the boundaries are reduced to a single point wherever there is a single sample. Alternatively, a second process could be

proposed in which the minimum and maximum bounds are found by comparing the post-process data. That is, the data after linear interpolation. Figure 6-10 is superimposition of all 50 trials on a single graph. As it is visually noticeable, the profile is blurred and a region is formed. The problem with this approach becomes clear in a closer look provided in Figure 6-11.

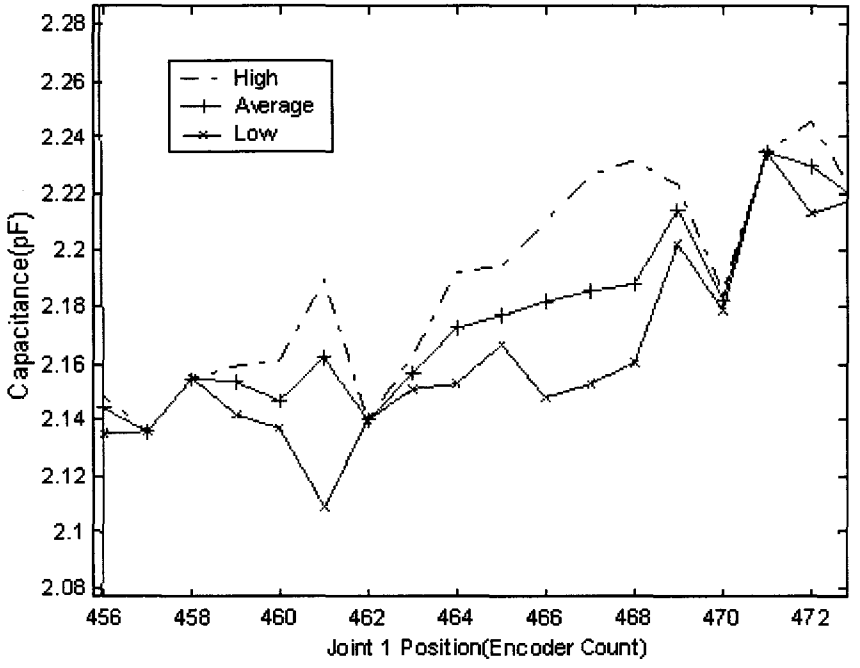

Figure 6-9: Close-up of the boundaries obtained by linear interpolation

For the given 50 trials, the upper bound is indicated by the thick line. It is seen from the data that the area between the peaks are not covered. That is to say although it is apparent the points like the one indicated as the "missed point" could be seen during normal operation, they would be violate the boundaries generates by this method.

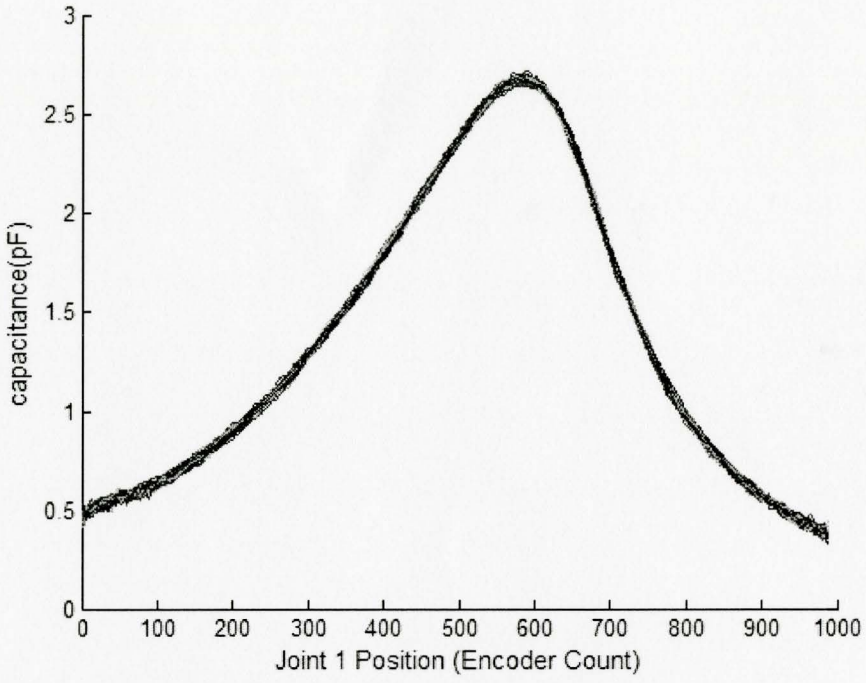

Figure 6-10: Overlay of all interpolated signatures

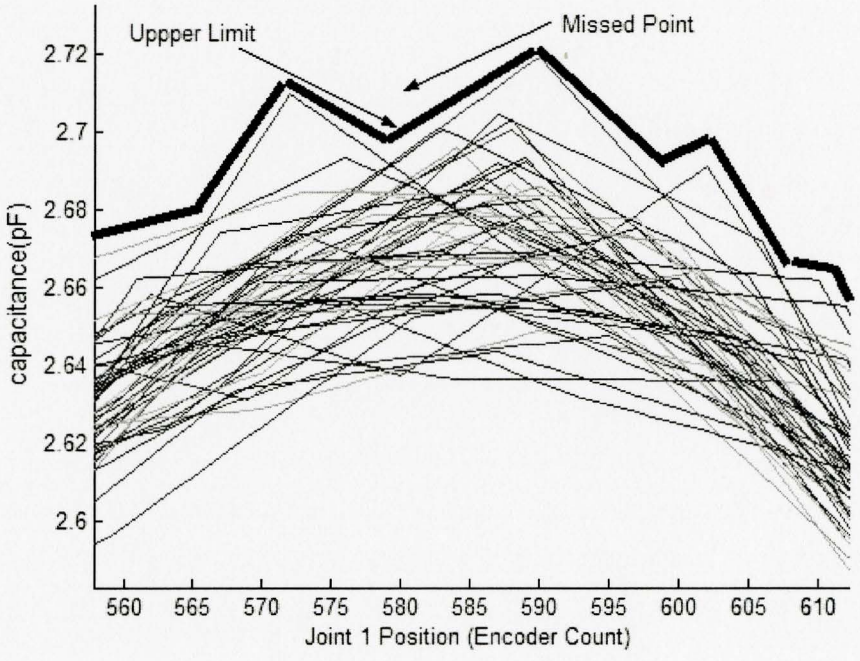

Figure 6-11: Close-up of overlay of all interpolated signatures

6.5.3 Low-pass Filtering

It is clear from the preceding illustrations that linear interpolation of each trial results in a noticeable jitter. Low-pass-filtering of the data can substantially reduce the local fluctuations. A basic low-pass-filtering could be achieved by using the average of all the samples for each point. Figure 6-12 plots the average of a 50 trial run. To clarify, the sample average here refers to the average of all samples for every position point for all trials. For each point, a capacitive value is either measured or derived from the neighbouring points. With a 50 trial run, there would exist 50 sets of data. The average is the mean of data for each and every position point. This is done after a linear interpolation of all the raw data. Due to the small sample size for each point, a high frequency jitter is still present in the signature.

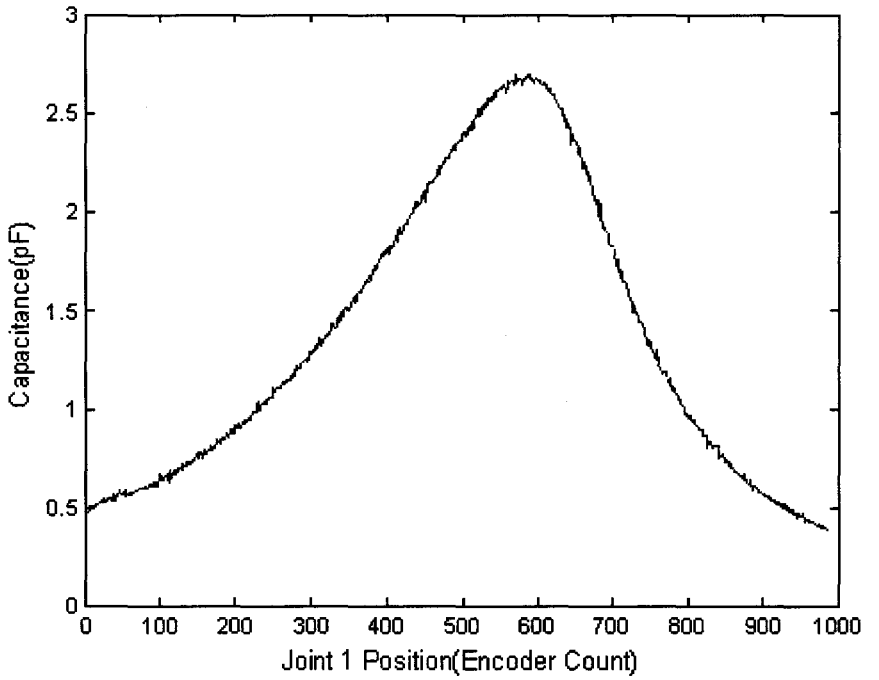

Figure 6-12: Sample average

It was pointed out that the scatter of points creates sample clusters (e.g. Figure 6-7). Hence a moving average across the cycle fraction (the position here) could further improve the quality of the data. This can be justified by recalling that the higher frequency content is not of value and the profile frequency of interest is on par with the frequency of the arm's motion. To avoid a shift, or a lag, the averaging window is centred on each point. Figure 6-13 compares the result of a moving average filter with a window of ±2 positions and the sample average. Figure 6-14 provides of a close-up. It is evident that the effect of the noise has been drastically reduced. The moving average is based on repeated data at the either end. For position points with no reading in the average-vicinity, the average is zero. The zeros on the horizontal axis of Figure 6-13 indicates positions for which no data existed.

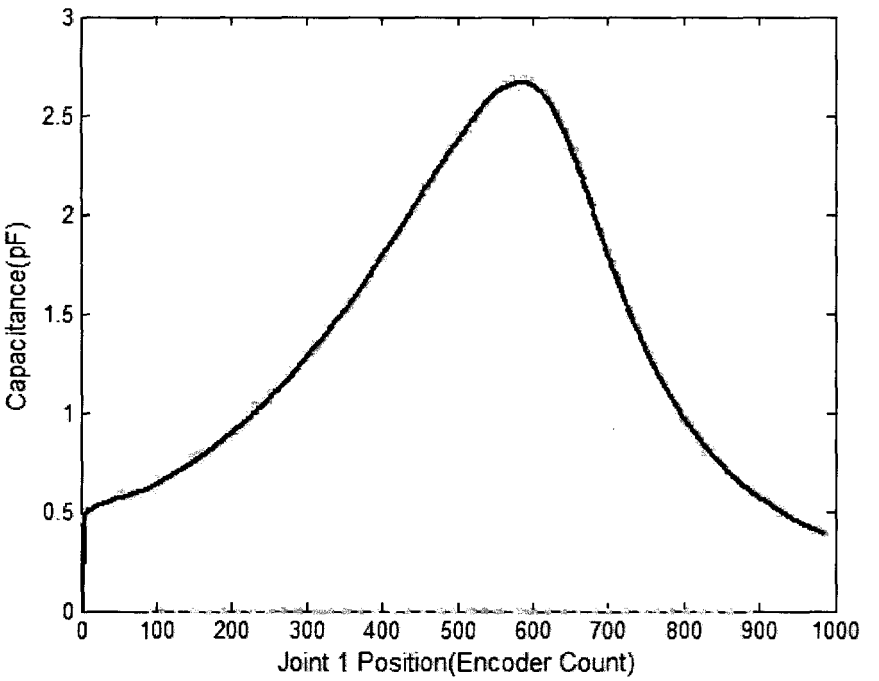

Figure 6-13: Plot of moving average filter and sample average

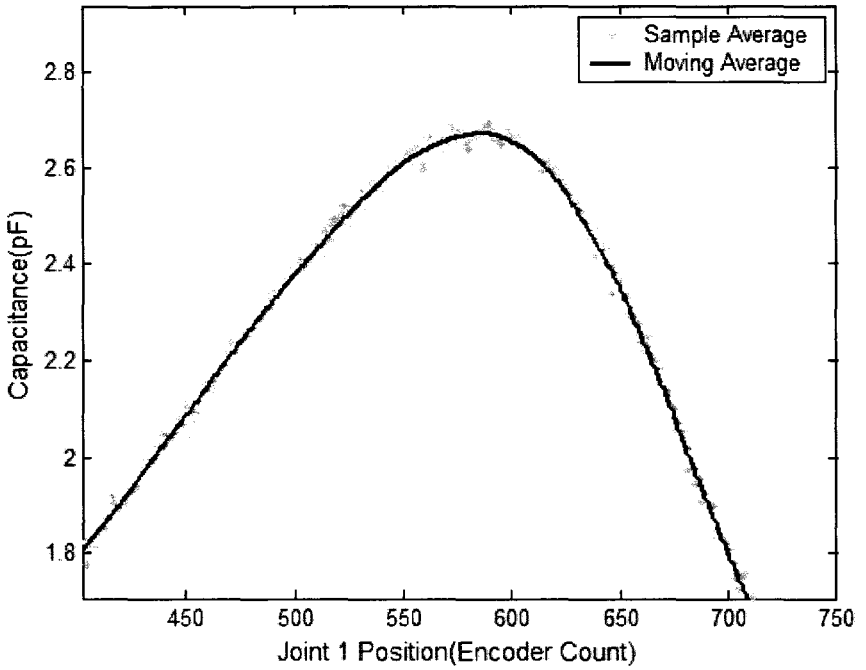

Figure 6-14: Close-up plot of the moving average and the sample average

6.5.4 Boundaries Based on Global Tolerance

In the previous sections, the direct use of the empirical data to establish the upper and lower boundaries was examined. It was evident that the suggested method requires a lengthy training time. This process is dependent on the range of data for each and every point. Therefore at points with a fewer samples, the reliability of the data was challenged. However, not every point suffers from this problem. If the entire range is considered, a more reliable estimation of the data scatter could be achieved. The maximum deviation from the mean at any point will be applied as the boundaries around the mean for the entire profile. In other words, the worst case of the data scatter observed anywhere in the entire range establishes the tolerances around the mean to find the boundaries. Figure 6-15 illustrates the limits found by relying on the global tolerance. Here the average is found by the moving average with the window of ±2 position. After that the maximum

deviation from the average is used is to establish the bounds. Figure 6-16 is the comparison of the boundaries with the entire dataset available. As seen, at no point in the 50 runs the limits are violated. Figure 6-17 is the close-up of the graph. While it validates the limits, it also indicates an excessive tolerance at some points.

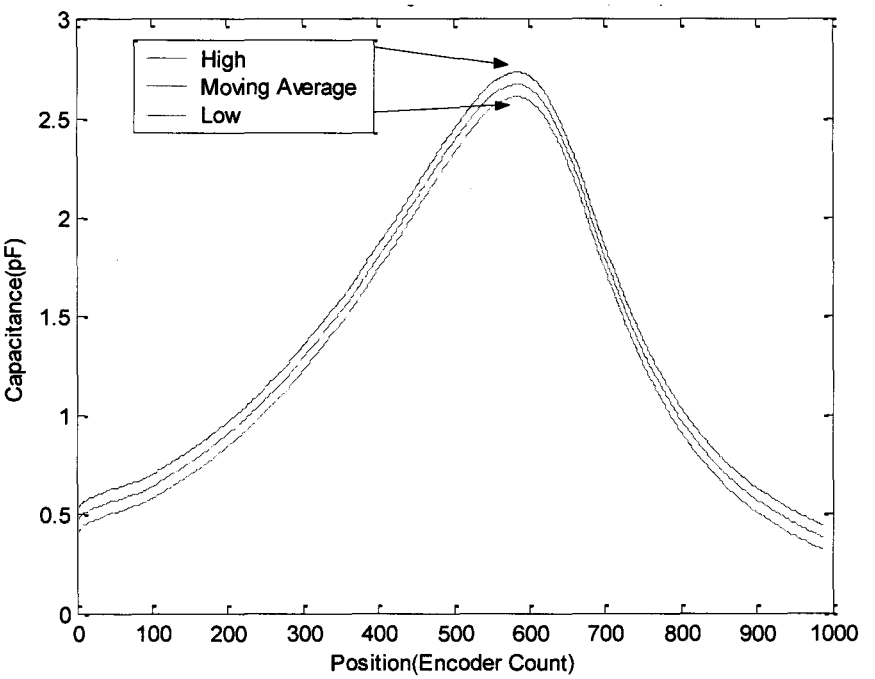

Figure 6-15: Boundaries obtained using global tolerance

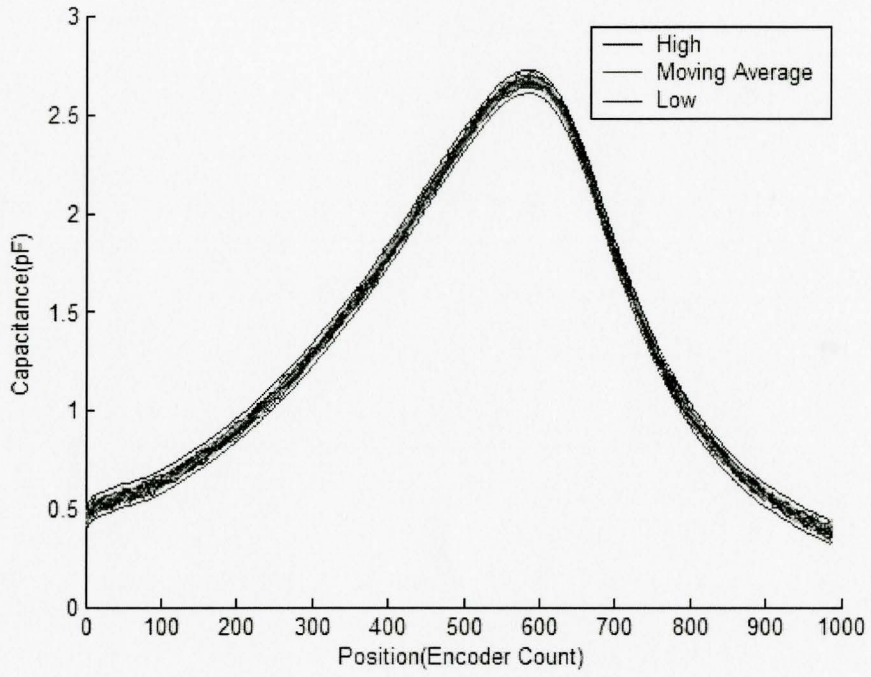

Figure 6-16: Confirmation that all samples are within the new boundaries.

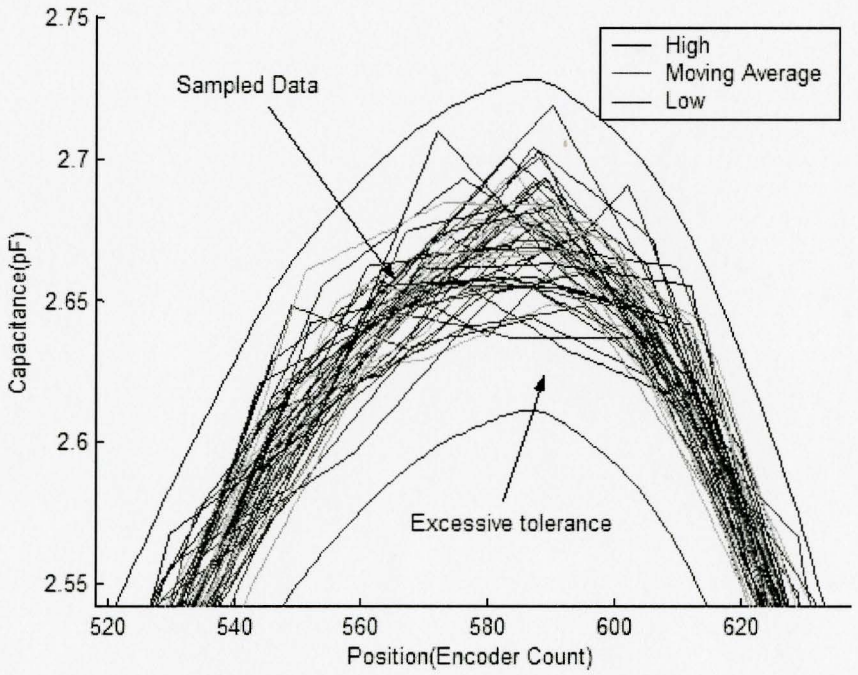

Figure 6-17: Close up of the data within the new boundaries

6.5.5 Boundaries Based on Localised Tolerances

In the preceding section, the global worst-case scatter was applied to the entire range. This resulted in potentially excessive tolerances in certain areas. The data scatter is dependent on the motion of the robot and the proximity of the plates and therefore it could change throughout the range. The previous method could be further improved by localising the tolerance boundaries. To this end a rolling maximum has been found for the points around each point of interest. In other words, for each point the boundaries are defined by the worst case of the neighbouring points. Figure 6-18 is obtained with a ±50 position window It is seen that tighter boundaries are formed. As expected this method is only applicable where a large amount of trial data is available. A study of the existing experimental data indicates window sizes of up to 300 are required at which point the boundaries are similar to those obtained using the global average method.

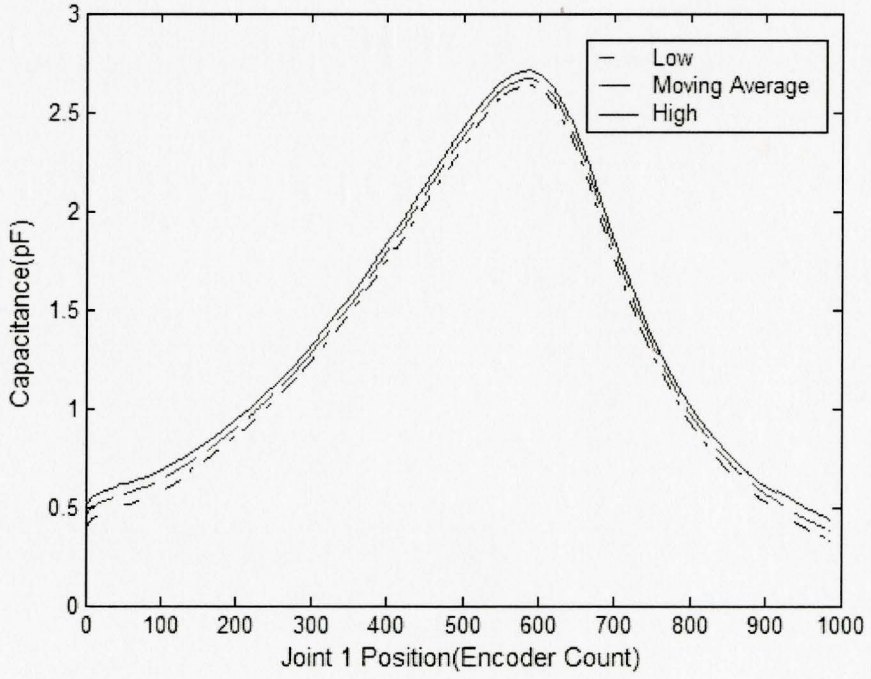

Figure 6-18: Local tolerance

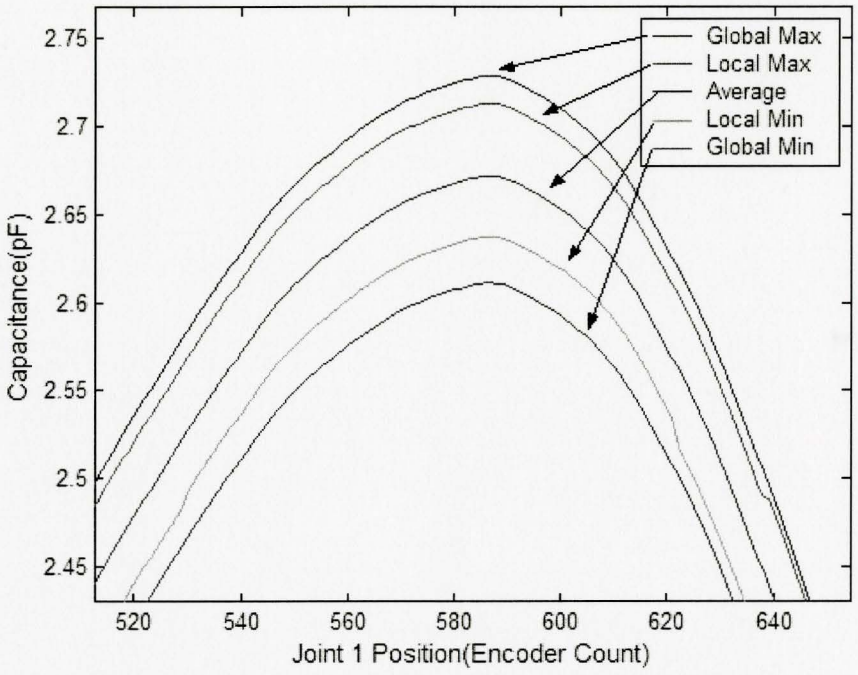

Figure 6-19: Comparison of boundaries obtained using the global and localised tolerances

6.6 Conclusion

In this chapter several methods for processing of the training data to obtain the operational boundaries were presented and compared. While it is possible to entirely rely on the experimental data from training to establish the true boundaries, the practical considerations call for a post-processing of the data to reduce the training time. It is obvious that an extended training requires costly downtime. While analysing the missing points, it was noticed that while the curve is non-linear, linear interpolation of the missing data provides a reasonable solution The direct interpolation method is applicable for very slow trainings or if extremely fast sampling is available to avoid sparse data sets. As background to this work, the author examined other methods including polynomial and

B-spline fit of the data; and none provided substantial enough improvements to justify their inherent complexity.

By using position averaging of the samples (*i.e.* moving average along the position dimension), the noise content could be substantially reduced. The offline nature of the processing enables this averaging technique to achieve this noise reduction without introducing any time or position shift. This creates a smooth signature around which the boundaries could be established. The local boundary determination was examined yet it was shown that it fails to be sufficient for a small trial size of 50. To overcome this issue, the global scatter of the data throughout the whole range will be used as the basis for the allowable range. The maximum deviation from the mean throughout the position range, indicates the extent of the potential deviation and is therefore used to create a region around the mean profile as the expected operational boundaries in the remainder of the thesis.

CHAPTER 7

Capacitive Collision Avoidance Runtime Module

7.1 Introduction

The first two components of the CAS are the sensing system and the training software module respectively. The training module generates the operational boundaries using the approaches described previously. The third component is the runtime software module. The runtime application is responsible for the real-time supervision of the robot(s) during its(their) operation. The software monitors the sensors and issues pause commands if abnormalities are found. The motion is only allowed to proceed if certain conditions are met. For multi-sensor systems, all channels are monitored and considered. The runtime module is to be executed independently of any control environment particular to the arms. In theory there is no limit on where this software should be hosted. A capable native robot controller could provide the virtual independent environment for this software. In the laboratory and for the industrial environments this research is tailored to, the module is run on a standalone PC.

All efforts have been made to simplify the runtime module. This is to ensure real-time effectiveness, portability between different environments, and improved reliability. To that end, input required by this module would be pre-processed by the training layer such that no further processing is required. A goal of this research is to make the CAS

easy to integrate with existing robot programmes. To accommodate the system, the robot or robots must accept a pause command that would cause an immediate stop of the work in progress. The controller(s) must also be able to proceed normally from the pause position to the completion of the task or a recovery state. The chapter begins with an overview of the main software algorithm. That is followed by a discussion of the decision-making steps in the CAS that pertain to the measurement errors. Next, the practical issue of the changes in the ambient condition is addressed. Finally, a brief list of the steps taken to further improve the software and a conclusion are provided.

7.2 Software Algorithm

The basis of the runtime software is a finite-state machine (FSM). The most basic form of this state machine is depicted in Figure 7-1. The connection between the runtime module and the robots ensures that the robots are commanded to stop when the software is in the *Paused* state. Conversely, the operation could continue when in the *Running* state. The initial state is set to be *Paused.* If safe conditions are found the software leaps to the *Running* state. The *Running* state is the continuous monitoring of the sensor input for all the cycle fraction points against the operational boundaries or limits.

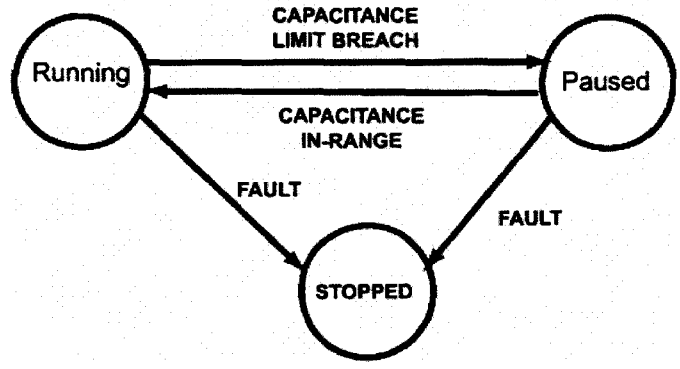

Figure 7-1: Basic CA runtime finite state machine

All unexpected fault conditions are to stop the operation indefinitely. That is, they do not cause a temporary pause but lead to the termination of the programme and the motion until the operator intervention. The following are some of the unexpected conditions:

- Out-of-range position

  When the position is utilised as the cycle fraction indicator, the margins of the operation must be well defined. If the position is found to breach these hard limits at any point this is an immediate cause for concern and should trigger a stop.

- Time-out

  If the robot fails to come out of the *Paused* state for a user-defined length of time, this is a fault condition. This could be an indication of a failed hardware component.

- Incomplete operational boundary data

  If the data provided is incomplete and contains points for which no limits are defined, the robot is stopped and the programme exits.

- Out-of-range sensor readings

  A reading that is out of range for the hardware indicates hardware failure. This is considered a fault condition leading to an immediate termination.

To implement the software in practice, and to accommodate the different states of the robot, minor modifications to the preceding FSM should be made. Two conditions are to be explicitly recognised that are not part of the collision avoidance scheme. One is the

initial homing phase of the robots. The other phase is an optional return phase. The main job does not necessarily need to end at the starting position. Therefore an end-of-cycle state is used to indicate that the robot is in the process of returning to the starting position. During this phase no monitoring is performed. If no unsupervised motion is permissible, the endpoint and start points could be at one physical point to eliminate the need for an unmonitored motion. The end-of-cycle indicator helps the runtime module to synchronise itself with the robot. The implemented version of the runtime FSM is shown in Figure 7-2.

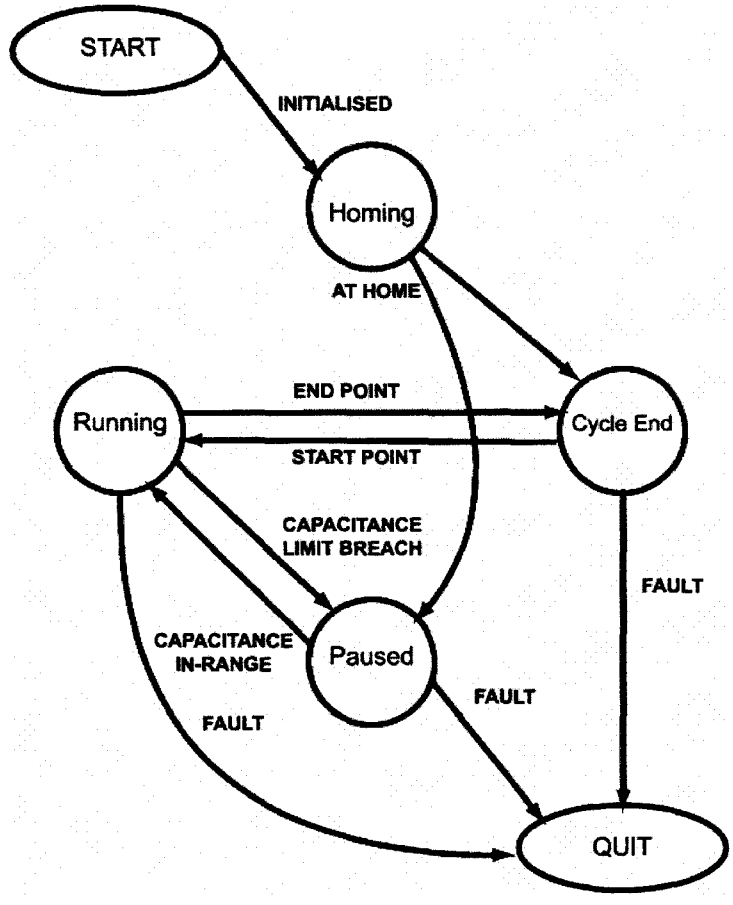

Figure 7-2: CAS runtime FSM

7.3 Ambient Change Compensation

It was discussed that the changing ambient factors could change the capacitance readings. The training data file contains the value of a known "reference" electrode to compensate for the ambient changes. The runtime module measures the capacitance of this reference electrode before entering the FSM cycle and uses this value to normalise all readings before comparing with the operational boundaries. This normalisation method was described in Section 5.7.

7.4 Software Optimisation

The runtime module has been developed in C. Certain steps have been taken to further optimise the basic software. Some of the notable steps are hereby listed:

- Pre-emptive electrode selection

  When more than one electrode channel is to be used with the multiplexer hardware, one method would be to select the desired channel just prior to acquisition. This would be followed by the comparison with the limits and decision-making. Knowing that the software is a loop, if the next channel is selected immediately after the polling and the time spent by the data processing is saved from the transient delay required for the next measurement. That is to say, the next sensor in line should be selected before moving forward with the decision-making.

- Position-indexed limits

  By arranging the operational boundaries in an array sorted based on the position, or the cycle fraction, the software requires the minimum time

accessing this data. Although this is arguably not the most memory-efficient method, it provides the quickest access time.

7.5 Conclusion

In this chapter, the basic algorithm for the runtime module of the CAS was presented. The algorithm is designed with simplicity and efficiency in mind. Therefore the response time of the system is almost entirely limited by the sampling rate and the sensor hardware[1]. More statistics regarding the reaction-time of the system and its performance is offered in the next chapter. The runtime component of the system is to have an unattended life cycle and therefore software robustness is of great importance. To improve the reliability the runtime module is spared of any processing. The runtime software constantly monitors the capacitive reading for collision protection. However, the system is designed to respond with a stop and exit for all unknown and known fault conditions. That includes cases indicative of collision avoidance hardware failure and/or software malfunction. This conservative approach is in line with the industrial application of the system. In the following chapter, the developed software is used to demonstrate the suitability of the system in a test environment.

[1] It should be noted that the reaction-time of the robot remains the primary source of latency.

CHAPTER 8

Experimental Results

8.1 Introduction

The operational theory of the proposed CAS was presented in the preceding chapters. In this chapter, the real-life performance of the system is analysed. The chapter starts with a more detailed look at the test workcell and the two tasks assigned to the robot for testing. Three methods are used to establish the performance. One is the analysis of data collected from 500 trial runs that are known to be collision-free. The profiles are compared against the proposed operational boundaries to verify if a reliable operation would have been achievable. Next is analysis of the data from multiple collision-like scenarios to verify if collisions would be detected. At last, the operability of the complete system is tested with the two test robots. The first two cases are exhaustive trials through which the CAS has no control over the robot. The measurements and the decisions of the system are recorded in log files. These cases are followed by collision avoidance experiments with the CAS system in control of the arms for both assigned tasks.

The testing has been performed on a workcell containing a CRS F3 arm on a C-500 controller and a secondary mock-up arm referred to as R2. The robot routine is developed in the native language to the C-500, RAPL-III. The runtime module is

developed in Microsoft Visual C++ 2005 Express Edition. It is hosted on a Pentium 4 workstation running Windows 2000 Professional. The communication between the PC, the sensor hardware, and the robot controller are through the PC printer port or the LPT Port. The LPT IO provides discrete IO to control and measure. The measurement hardware is accessed via an I^2C bus with a custom-made interface board. The driver software is based on an open source-code and tailored to the specifics of the chip.

8.2 The Workcell Arrangement and Assigned Robot Tasks

Figure 8-1 is the general view of the workcell. The robots perform two separate tasks. The start and end positions of the tasks are marked. As shown, the endpoint and the start point are physically separated and the robot has to travel back to the start point at the end of each cycle. This creates an opportunity to test the end-of-cycle state and is required for the use of the Joint 1 position as the cycle fraction.

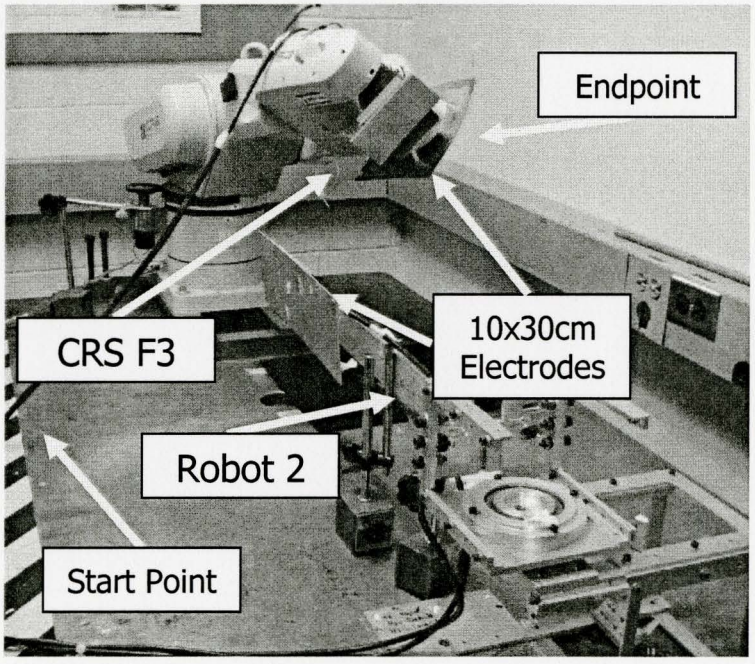

Figure 8-1: The Workcell

The second robot (Robot 2 or R2) is not self-actuated. It is a single joint revolute arm with a length of 75cm. Its position in the workcell is measured through its linear displacement at a point 30cm away from its pivot point as depicted in Figure 8-2. R2 rotates in the horizontal plane. The displacements are measured as deviations from the straight position (shown) to the left or right. Moving to the left has been noted as positive. For the small angles used, the displacement at the endpoint of R2 could be approximated as shown in Equation (8.1). For a 2cm measured displacement, the end of R2 moves 5cm.

$$d_{endpoint} = \frac{75}{30} \times d_{measured} \tag{8.1}$$

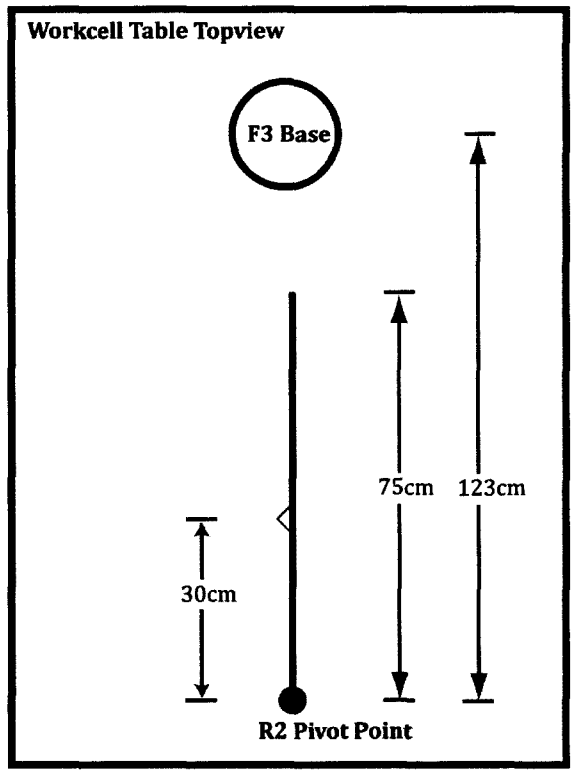

Figure 8-2: Workcell top view

The first task is a pick-and-place job for the F3 with no movement of R2 expected. The F3 starts with its end-effector on the left of R2, proceeds to pass overtop of R2 and ends the cycle on the right side of R2. The second task involves movement of both arms during a cycle. Since R2 is non-actuated, to create a scenario in which both arms are active, a plastic extension is attached to R2 to use the motion of the F3 to drive R2. At a known point in the cycle, the F3 drives the second robot and creates a synchronous motion. This is to represent cases where more than one robot are to manipulate a workpiece. A modification to, or removal of this extension would change the position of R2 as F3 approaches. The setup is shown in Figure 8-3

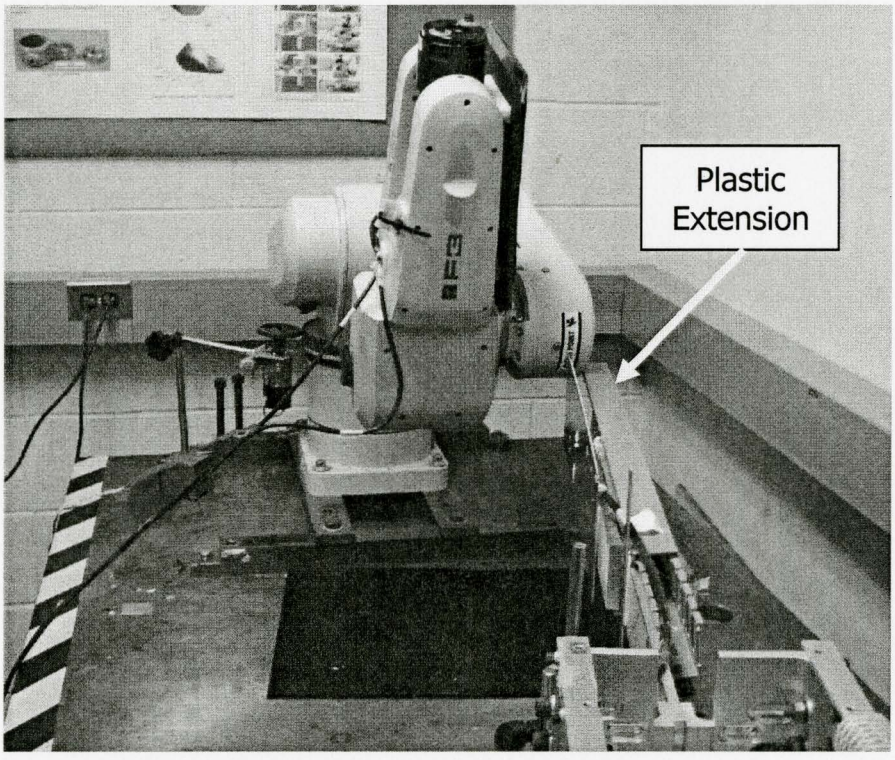

Figure 8-3: Second test-setup with moving R2

8.3 Numerical Test Case 1

The robustness of the system against measurement noise and other fluctuations is tested by comparing the data log of 500 test runs with no "collision" against the limits found for the task with a 50-run training. To test, the maxima and the minima for each and every point in the log were found. The results are depicted in Figure 8-4. The biggest dispersion is found to be 0.138pF and the greatest deviation from the average is 0.085pF. The data ranges from 0.326pF to 2.75pF. That is a signal-to-noise ratio of approximately 16.3.

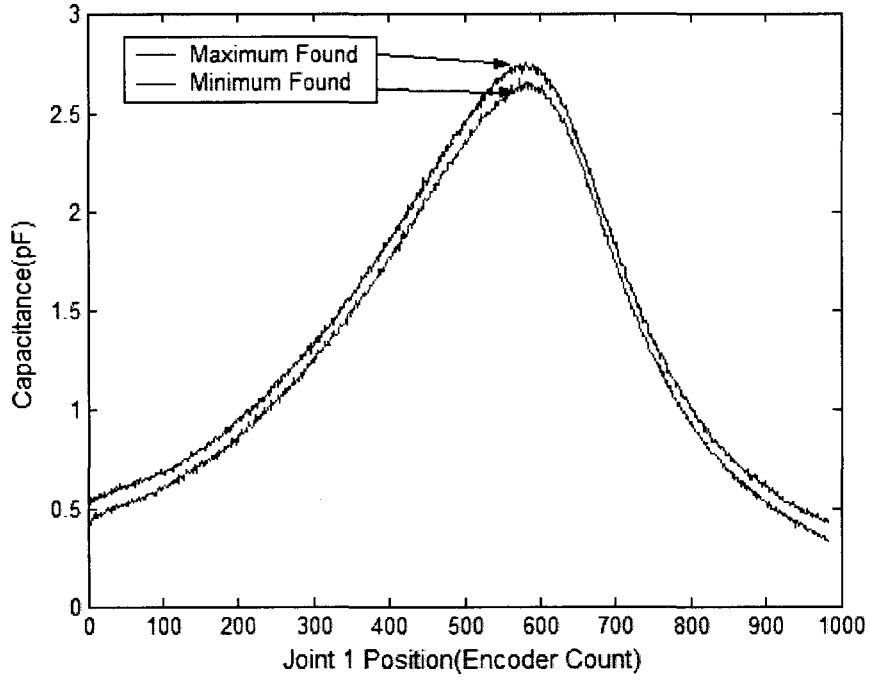

Figure 8-4: Minimum and maximum values for all points for 500 trials

Figure 8-5 is the illustration of the maxima and minima against the operational boundaries found in Chapter 6. As seen, the limits are not violated at any point. The five curves in the graph appear in the same top to bottom sequence as noted in the legend.

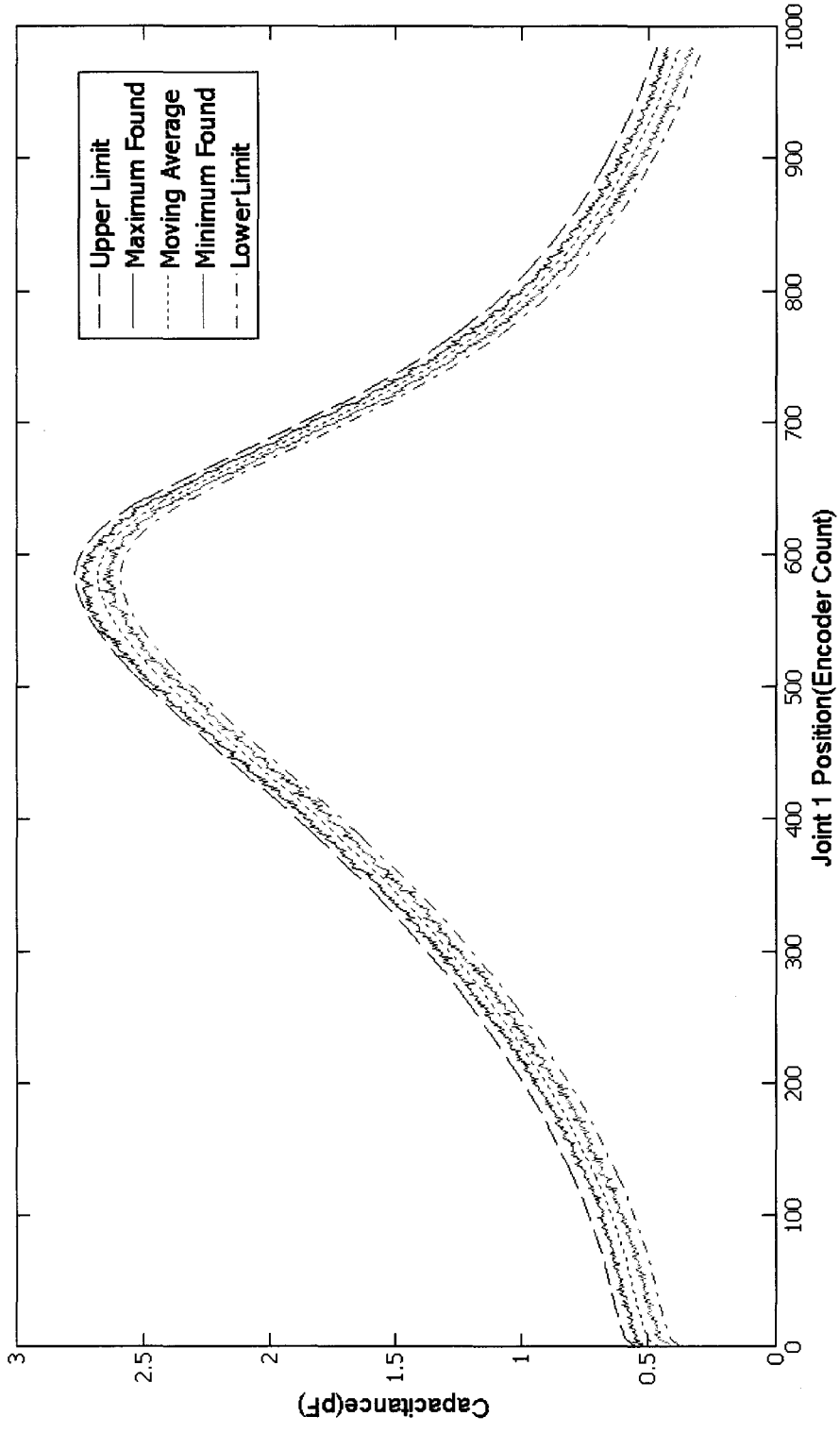

Figure 8-5: The operational boundaries (limits), runtime measurements, minima, and maxima

8.4 Numerical Test Case 2

The second test of the system is by numerical evaluation of multiple "collision" cases for the first task. The intention is to establish the sensitivity of the system and the smallest changes that are detected. The data for ±2cm deviations are shown here. Figure 8-6 shows the log of the data with the R2 arm moved to the left in Figure 8-2 or the approaching F3. From the geometry of the setup, no physical collision could occur. Yet in line with the design intentions, the system detects the irregularity and would have asserted a pause signal. Figure 8-7 is an example of data with R2 moved away from the robot. This leads to a lower limit breach and would have triggered a pause. Figure 8-6 is the test with R2 moved 2cm to the right.

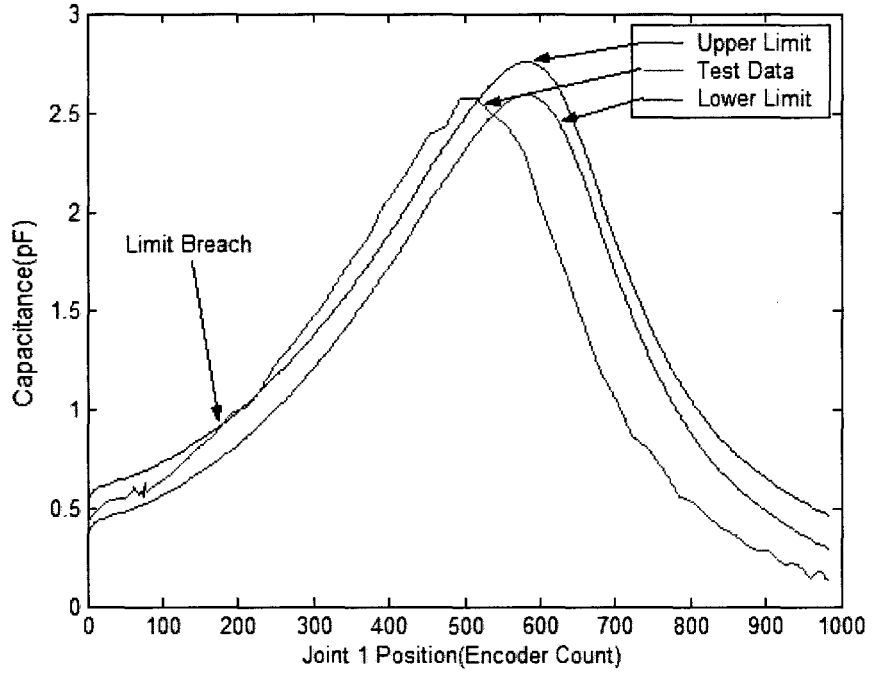

Figure 8-6: Test with R2 endpoint 2cm to the left (*i.e.* towards F3)

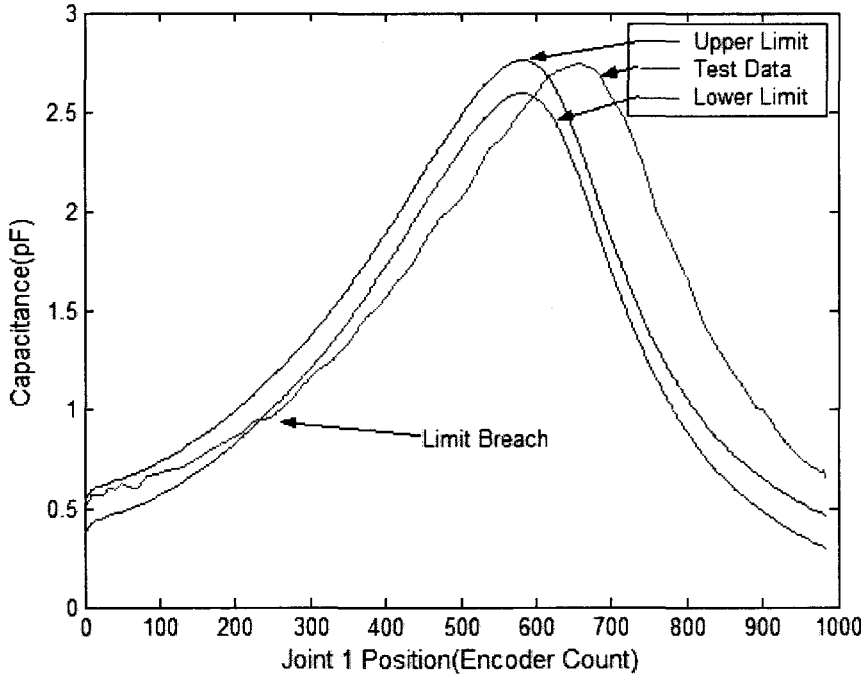

Figure 8-7: Test with R2 endpoint 2cm to the right (*i.e.* away from F3)

To further investigate the accuracy, the test was repeated for a more minute deviation. New limits shown in Figure 8-8 have been found based on a new training. In this case R2 is moved 2mm at the point of measurement. This translates to ±5mm of travel at the tip of the arm. As marked by the arrows, the shift is noticed by the algorithm at about a quarter of the way into the cycle. In the -2mm case, the displacement is observed later. The 5mm displacement of the sensor is only at the tip. The revolute motion of the non-actuated R2 reduces the overall impact of the change. Despite this, the displacement of 5mm is noticed. It should also be added that as seen in the setup pictures, the electrodes are not face-to-face and no real collision is possible. It is apparent that when the electrodes are aligned, a greater shift results and earlier detection should be possible.

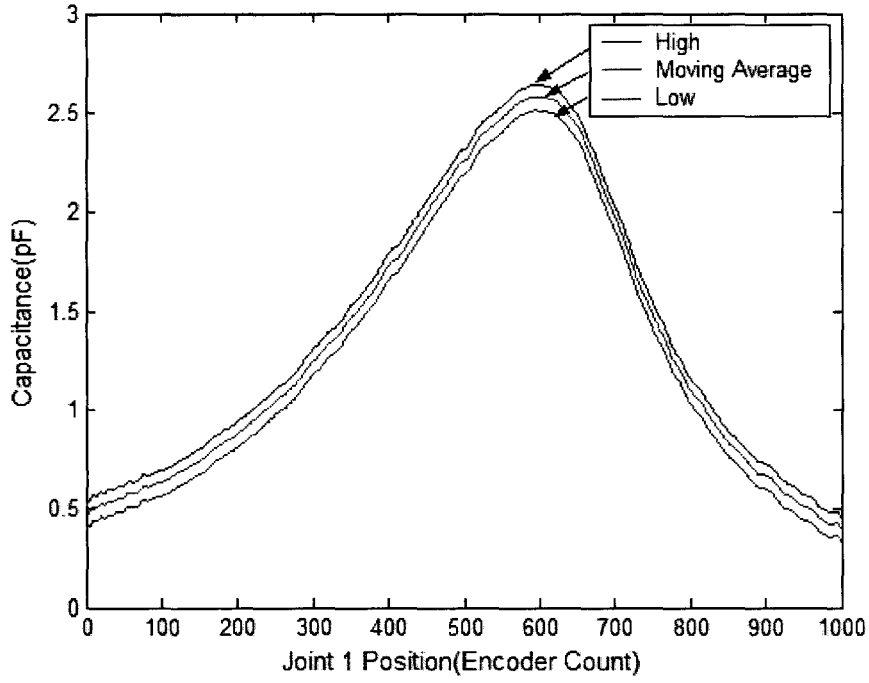

Figure 8-8: New boundaries used for the collision tests

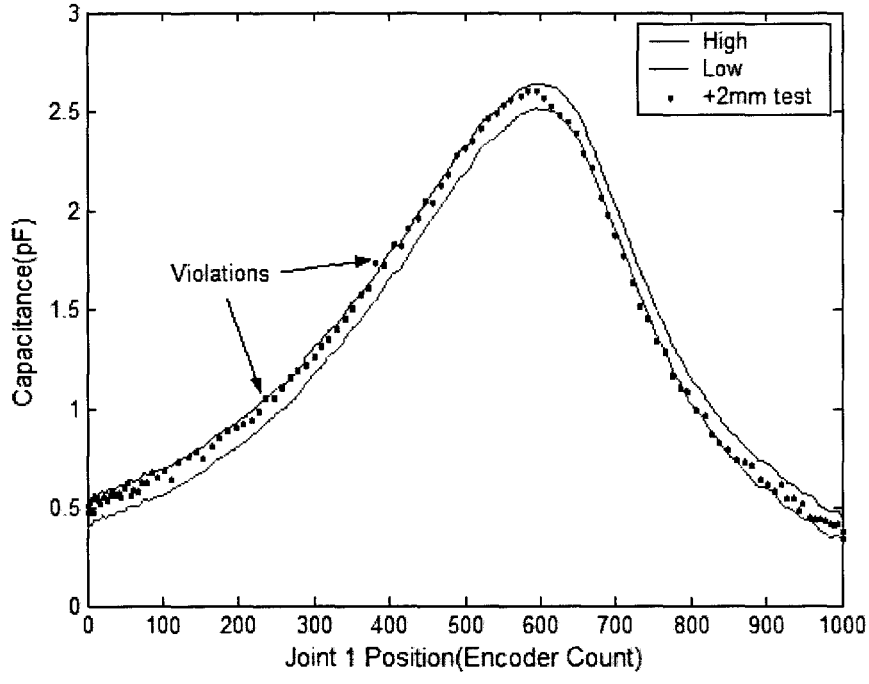

Figure 8-9: +2mm deviation test result

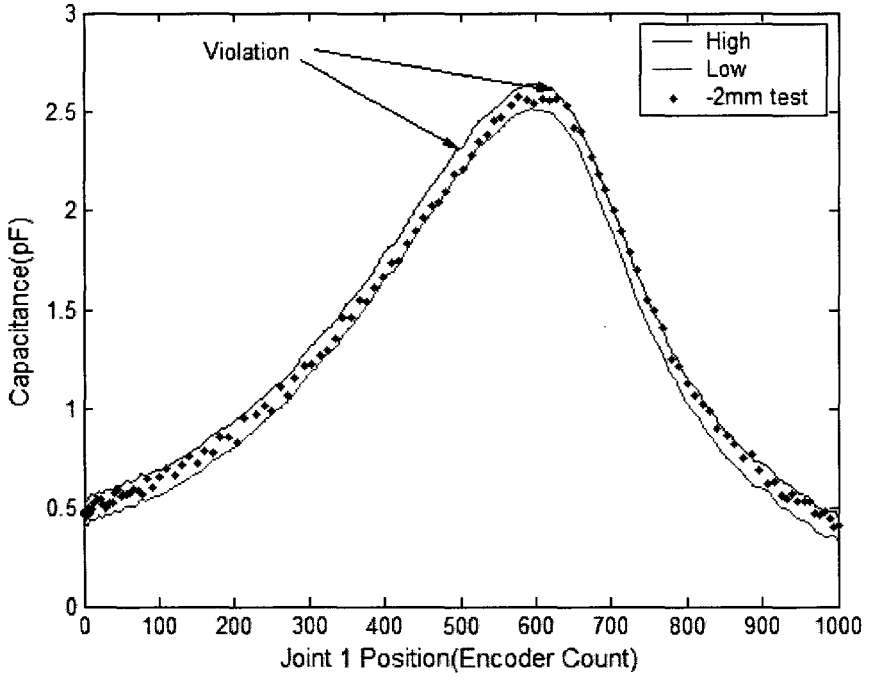

Figure 8-10: -2mm deviation test results

8.5 Collision Avoidance Experiments

Further assessment of the system is offered through experimental collision avoidance for both tasks. The cycle for the first task is as follows:

I. Time=0s: The F3 starts from the home position

II. Time=5.5s: The F3 reaches the destination point and announces the end-of-cycle

III. Time=8s: The F3 returns to the home position and starts a new cycle.

The F3 was set to a speed of 10. The normal cycle was disturbed by moving R2 to the left or right to verify the behaviour of the system. Figure 8-11 is the case of R2 moved to the left. At first the robot was allowed to proceed for a few cycles. At the time[1] t=2.57s into the test cycle, R2 was moved to the left, which resulted in the F3 pausing at

[1] As recorded by the supervisory PC

t=2.75s. At the time t=4.18s, R2 was returned to the original position. At t=5.01s the F3 continued on its path and finished its cycle at t=8.12s. A similar test was performed with R2 moved to the right to verify the lower limit functionality

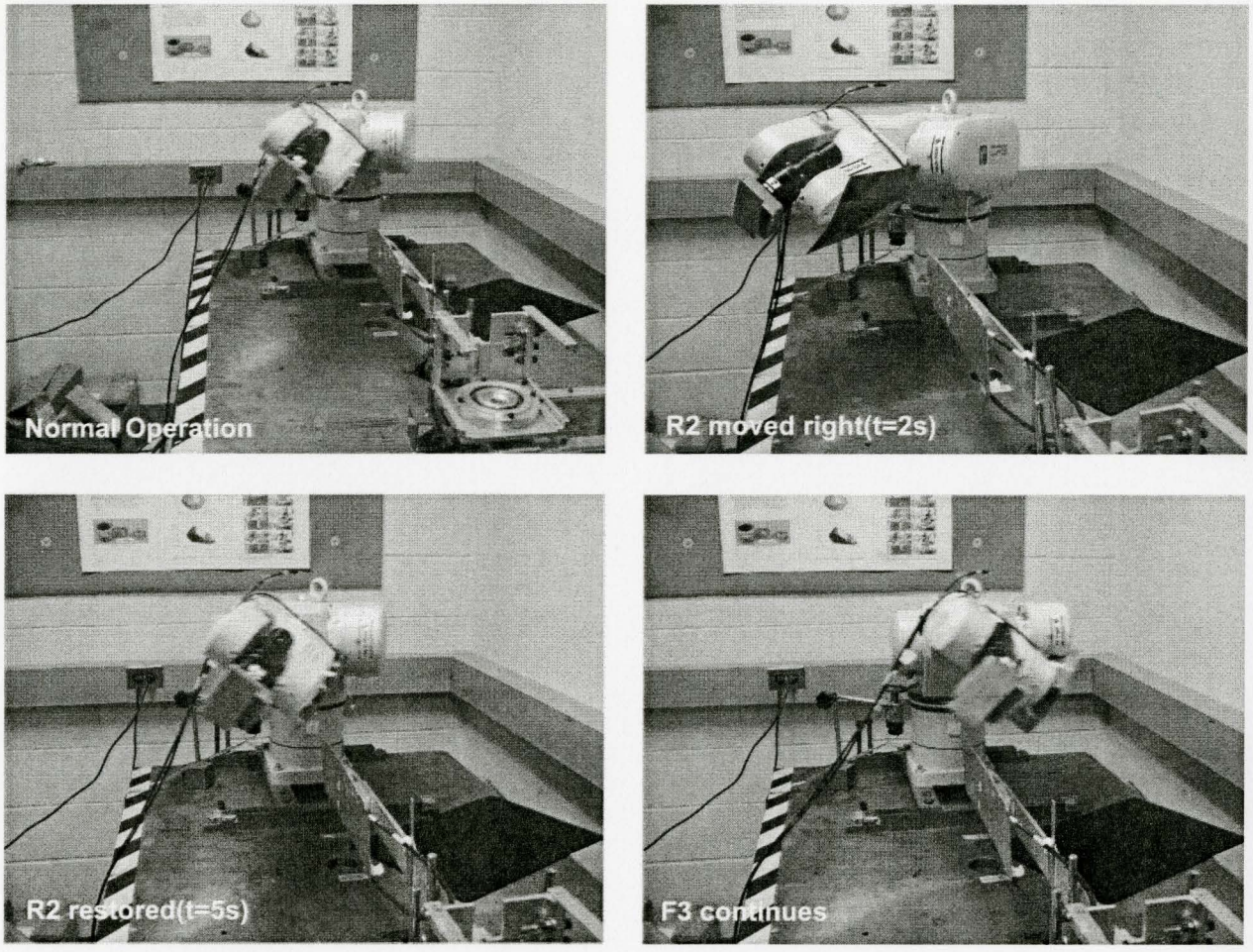

Figure 8-11: Still images of the collision avoidance demonstration

As previously explained, the second task involves a synchronous motion by both arms. Figure 8-12 to Figure 8-14 show the major events throughout the cycle. The uninterrupted cycle is as follows.

I. Time=0s: The F3 starts from the home position

II. Time=6s. The F3 comes in contact with the R2 plastic extension and starts to push it away, this is a planned part of the job and is not considered a collision.

III. Time=9.4s. The F3 reaches the end of its cycle while it is pushing away R2. The end-of-cycle flag is raised and the return to home portion begins.

IV Time=13.3s: The F3 is at home position and starts a new cycle.

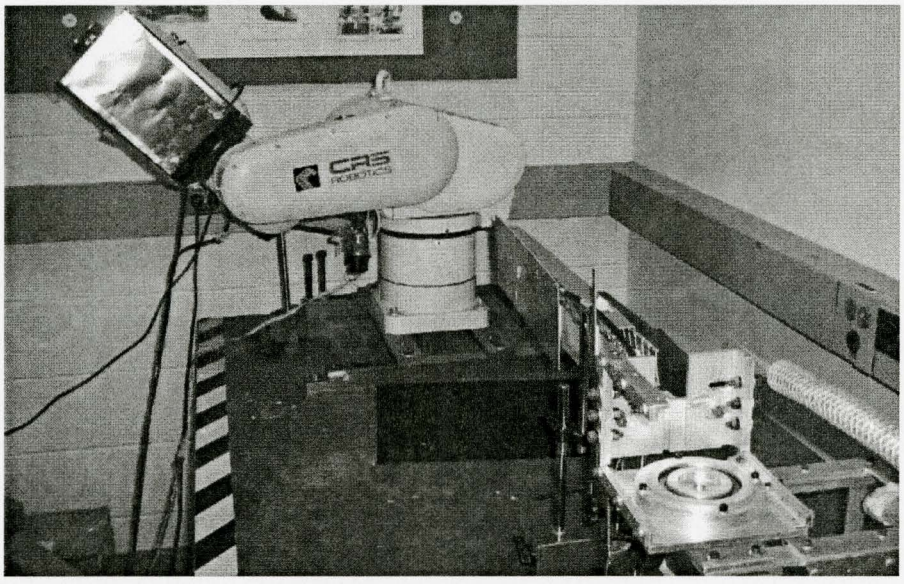

Figure 8-12: Second task, start position

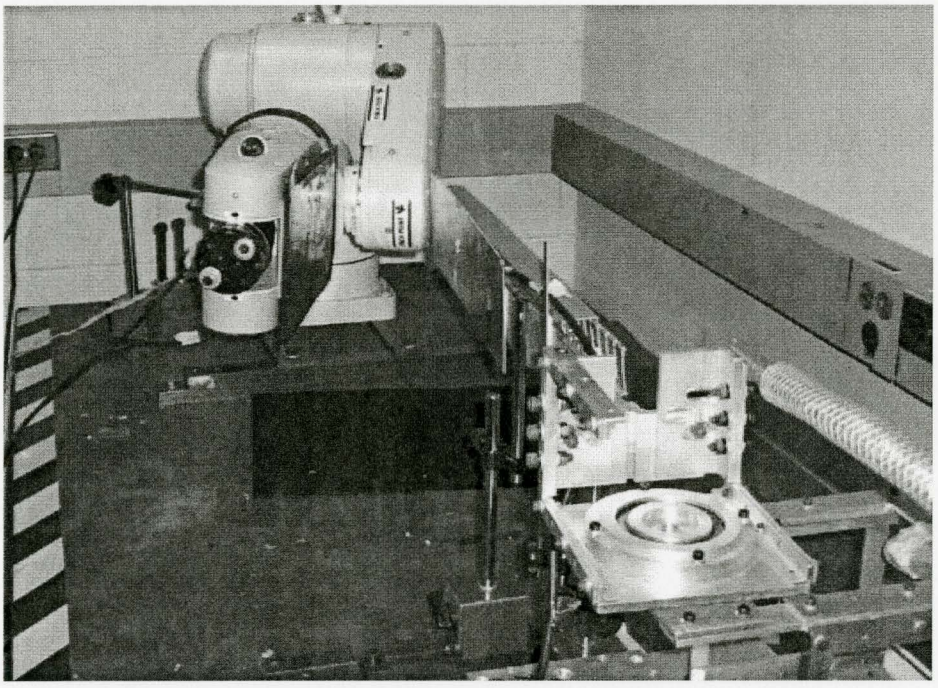

Figure 8-13: Second task, F3 pushing the extension

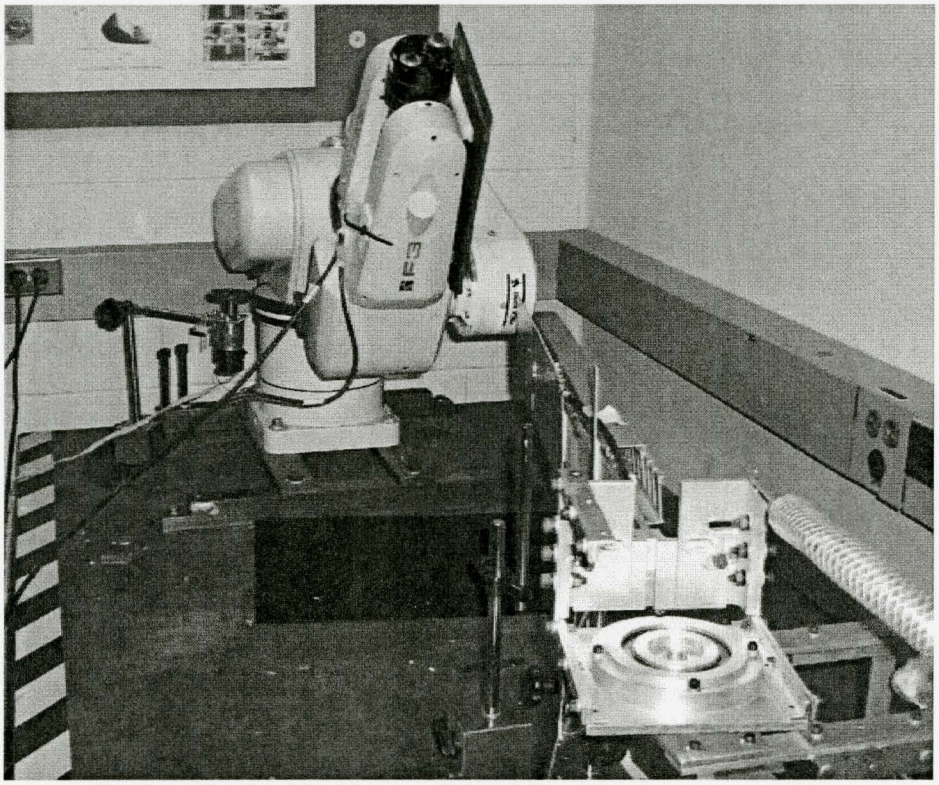

Figure 8-14: Second job, endpoint

Figure 8-15 is the capacitive signature of the second task plotted versus Joint 1 position. Figure 8-16 is the capacitance ratio plotted versus time for the cycle. It should be noted that in these, and in subsequent experiments, the ratio of capacitance to the reference capacitance is used rather than simply the capacitance as measured. The reasoning and details for this are described in Section 5.7. During the return portion, no measurement is made and the runtime module records the value of –10 for all the points for which no measurement exist.

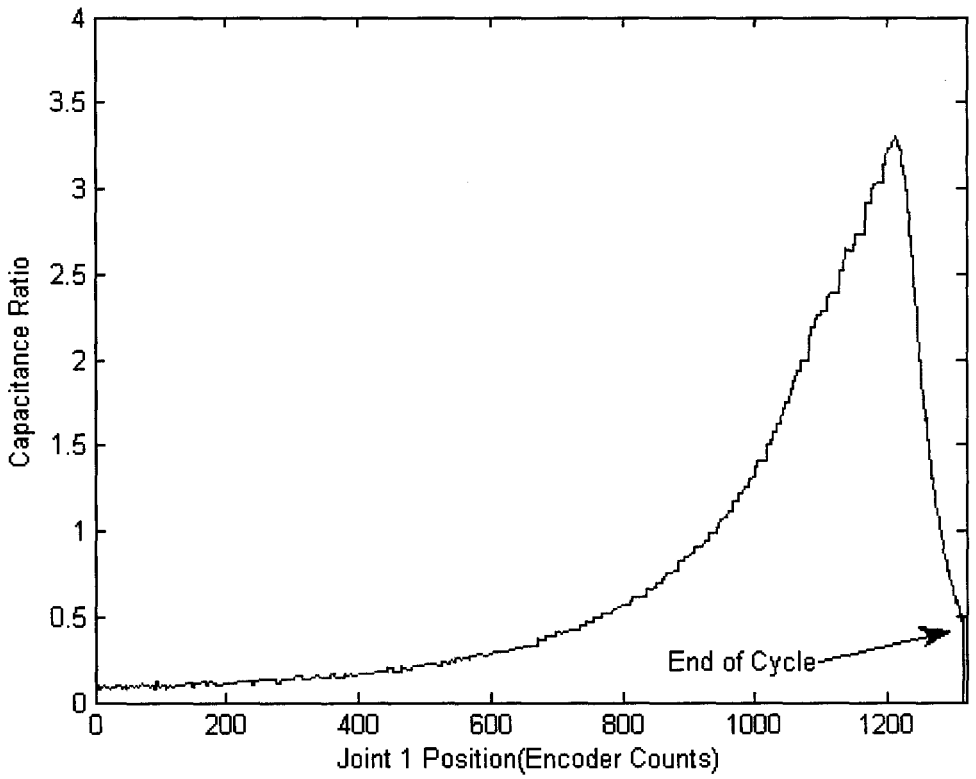

Figure 8-15: Capacitive signature of the second task

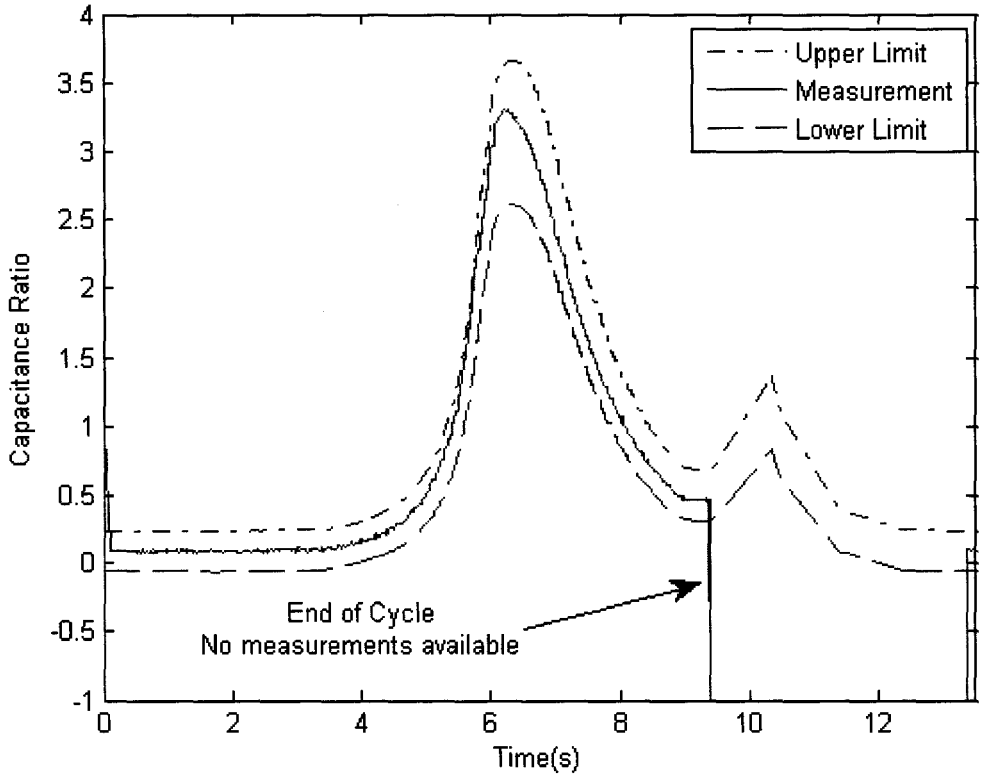

Figure 8-16: Capacitive ratio throughout the cycle

Figure 8-17 shows the capacitance ratio, the Joint 1 position and the pause and go decision of the system. A go command is indicated with a one while a zero indicates a pause command. This is an example of uninterrupted cycle and the go command is maintained throughout. Figure 8-18 shows a test with two cycles, with a potential collision during the second one. At t=17.82s, an unacceptably high value is measured, and the pause command is transmitted to the F3. The arm comes to stop at t=18.2s. The second robot is returned to its position and the measurement is back in range at t=20s and a go command is asserted. At t=21.5s the F3 starts to move again and completes its cycle. This pause/go sequence is enlarged in Figure 8-19. Based on numerous experiments, it could take up to 400ms for the C-500 controller (connected to the F3) to process the pause command and stop the robot

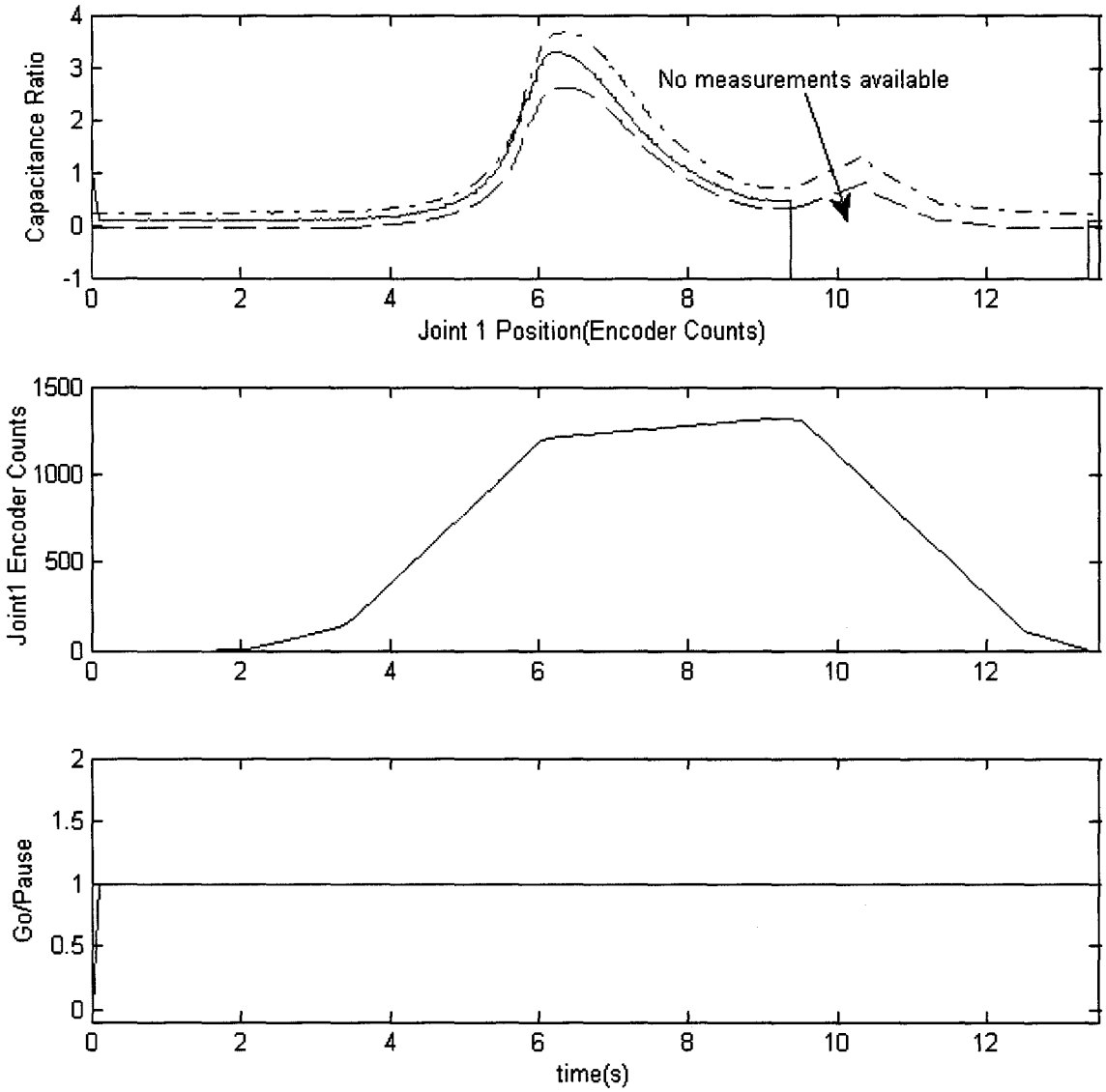

Figure 8-17: Experimental results showing capacitance ratio, Joint 1 position, and CA decision results for an uninterrupted cycle

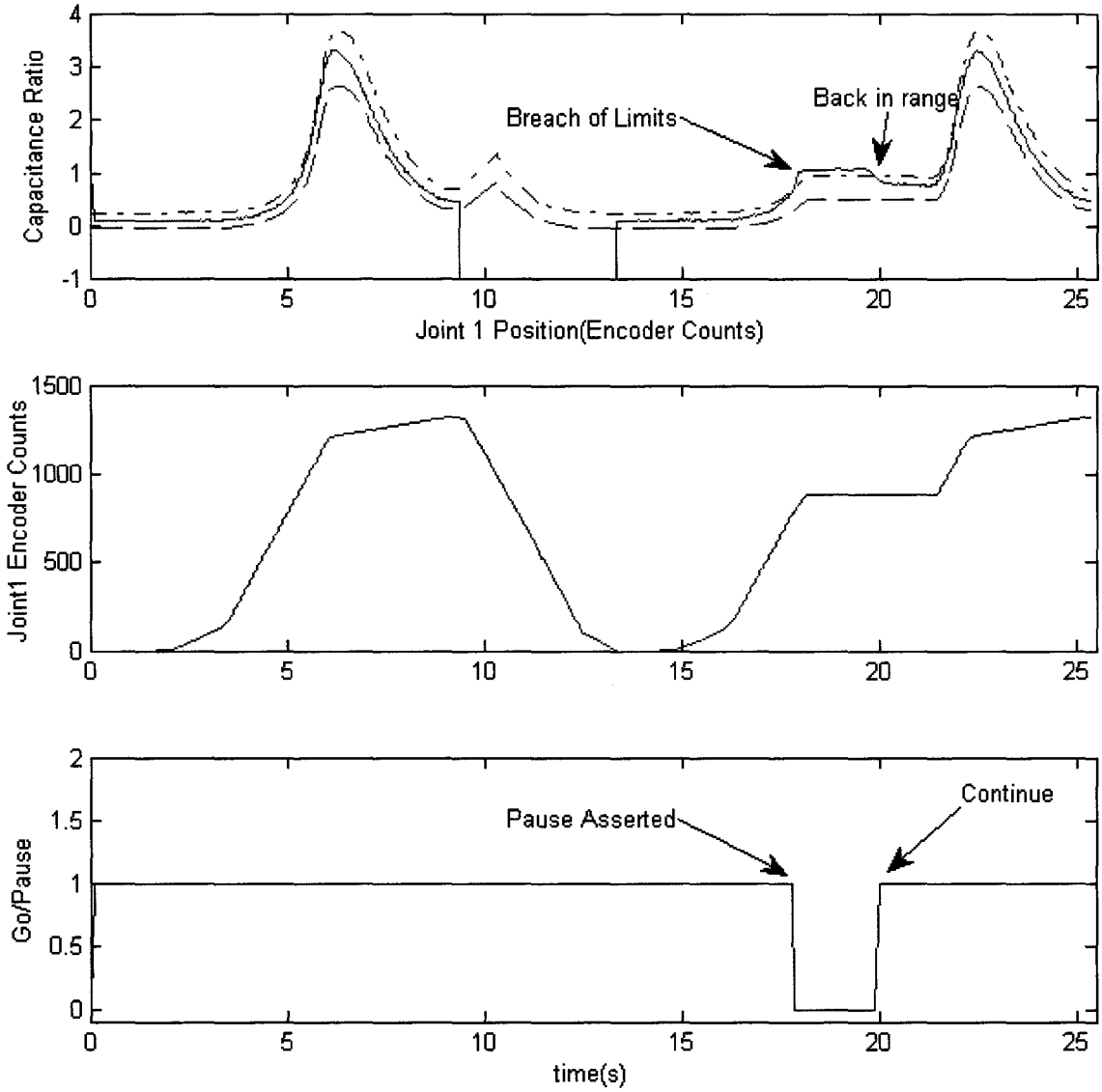

Figure 8-18: Experimental results with an uninterrupted cycle followed by a cycle with a potential collision

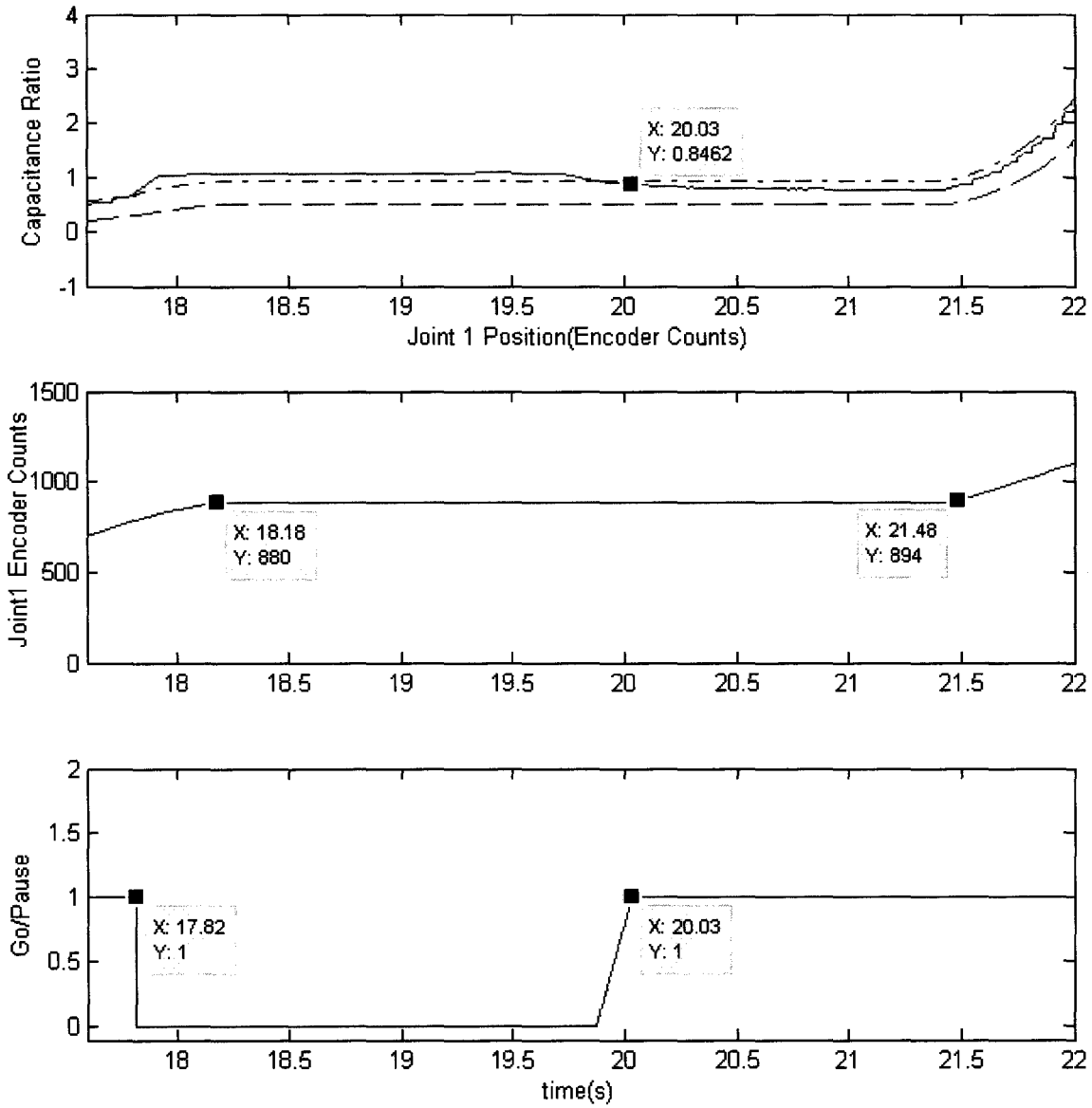

Figure 8-19: Close-up of a pause/go sequence from a cycle with a potential collision

Figure 8-20 is an example of the system's reaction to repetitive potential collisions. R2 has been moved out-of-place in each cycle. The second cycle is enlarged in Figure 8-21. In this cycle two possible collisions are encountered. The second abnormal condition is intentionally corrected quickly to inspect the reaction of the CAS and the F3 controller. Figure 8-22 is focused on the second fault.

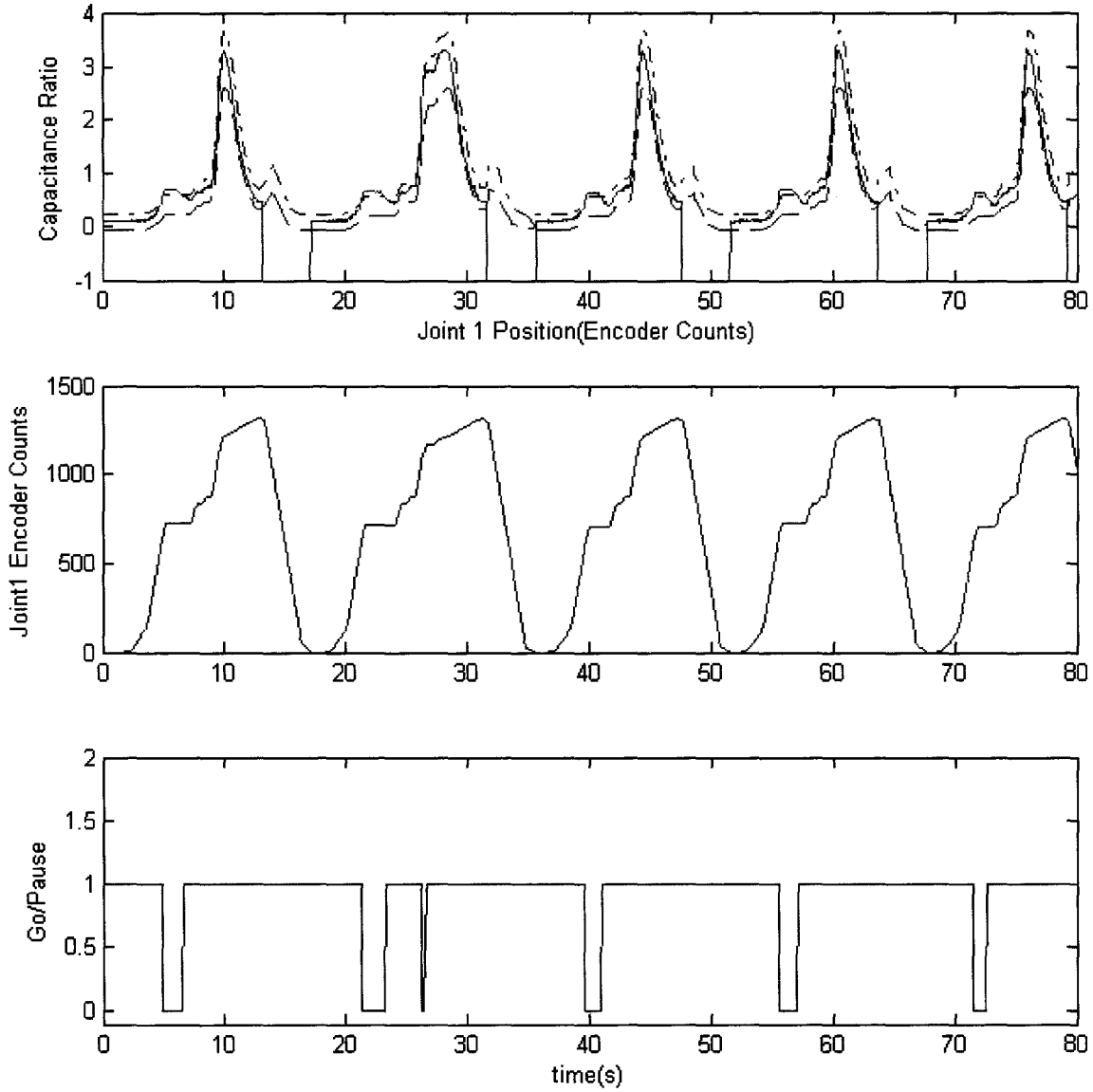

Figure 8-20: Experimental results with at least one potential collision per cycle

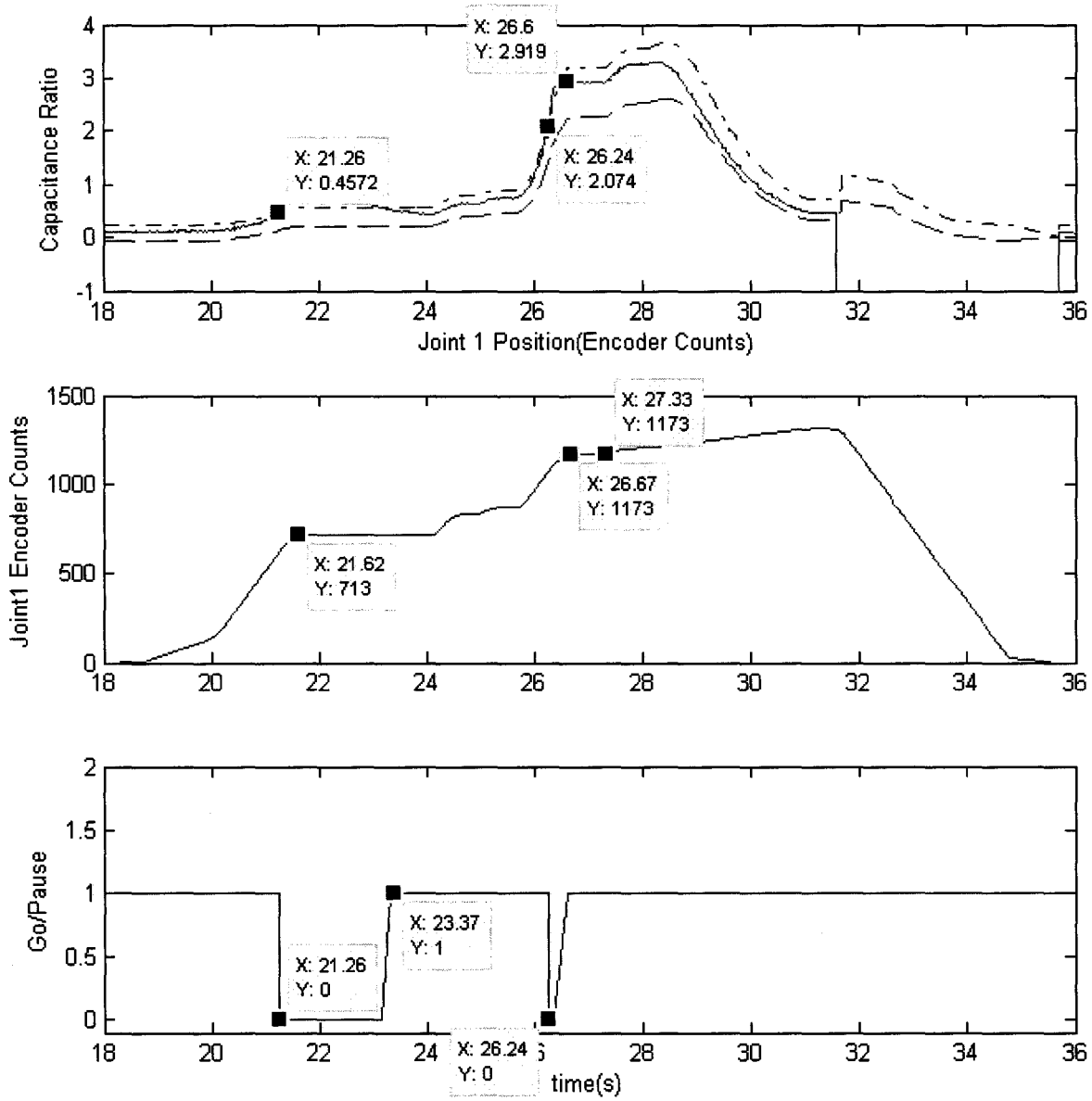

Figure 8-21: Close-up of a cycle with two potential collisions

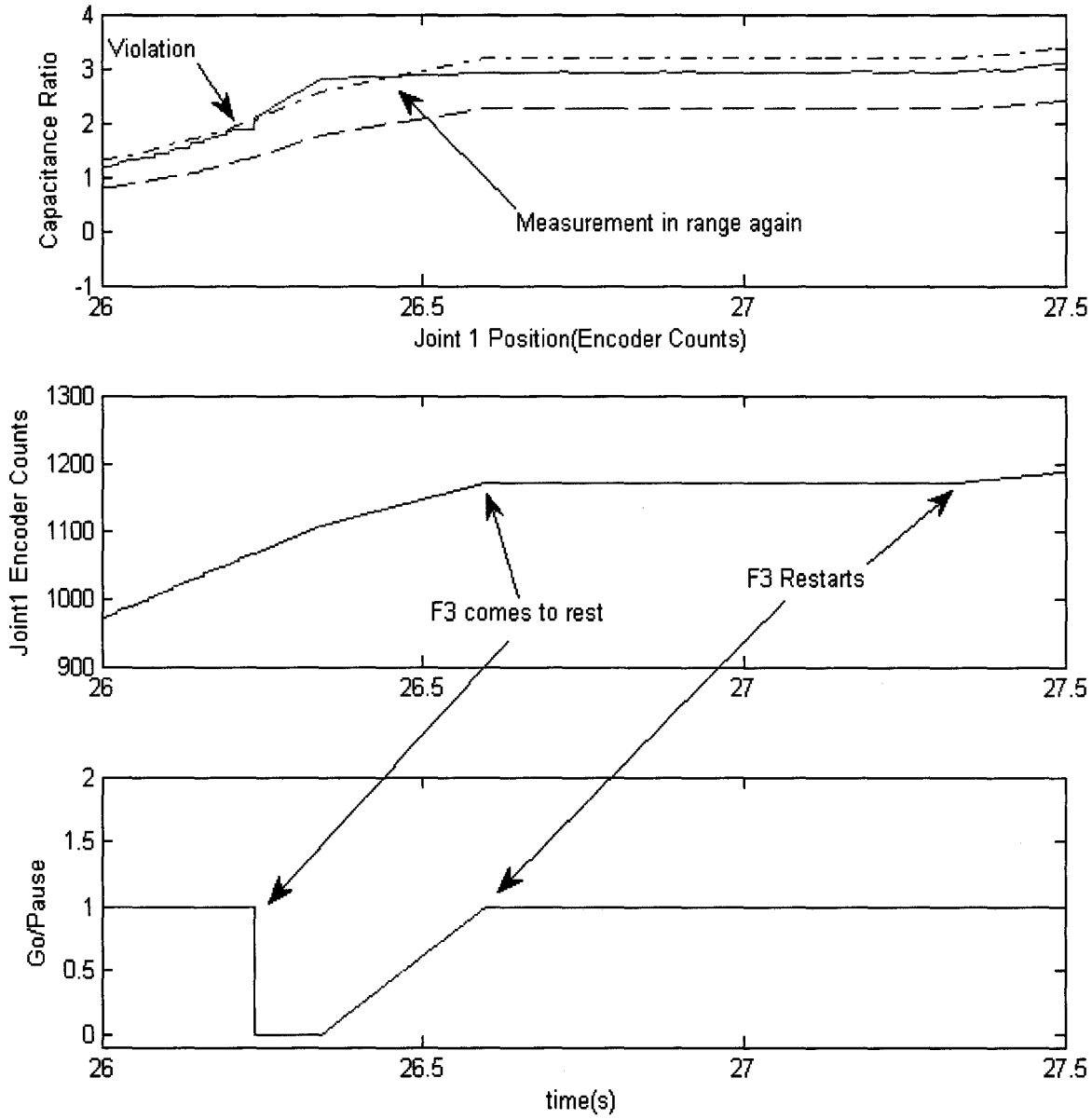

Figure 8-22: Close-up of the collision avoidance reaction to the second potential collision

The runtime module user-interface indicates the current state and the last state in the queue. An example of this user interface is available in Figure 8-23. The runtime module is also designed to provide a detailed log of the process saved automatically

based on the start time of the run. All decisions and readings based on which the decisions are made are recorded in the log file.

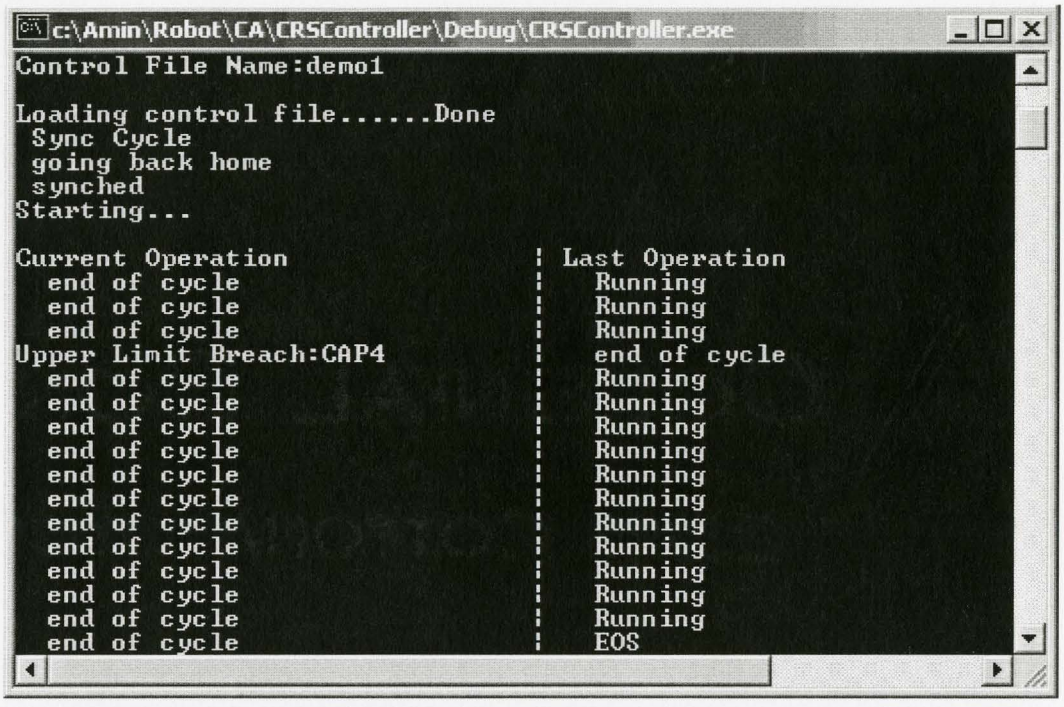

Figure 8-23: Runtime module user interface

8.6 Effect of the Robot Speed

The speed of the robot was found to have a profound effect on the collision avoidance system. Arm motions at higher speeds are likely to produce more vibrations and variations and therefore larger tolerances are required. While the exact values and the amount of the change is dependent on the geometry, it was noticed that at higher speeds larger limits are generated by the processing software. The shape of the upper and lower boundaries also changes somewhat. The following three figures show the boundaries found for the second task at three different speeds of the F3 arm.

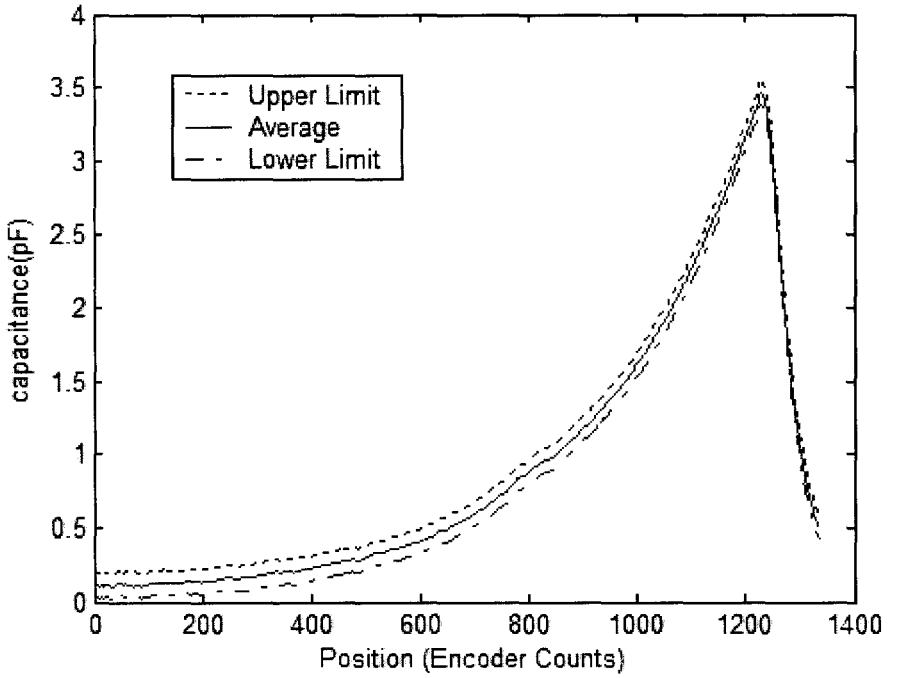

Figure 8-24: Limits with training done at a speed of 5

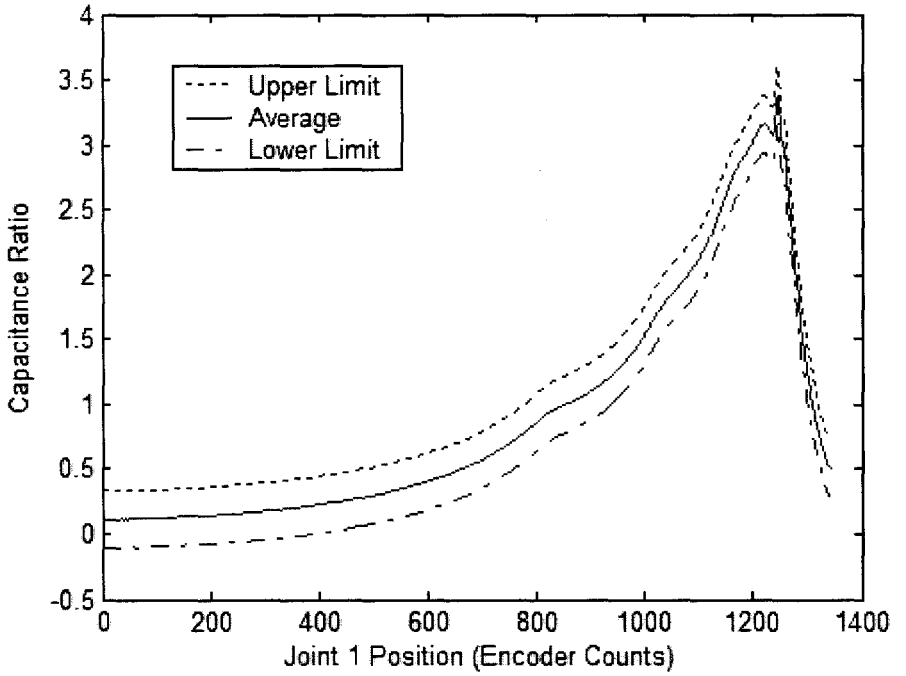

8-25: Limits with training done at a speed of 10

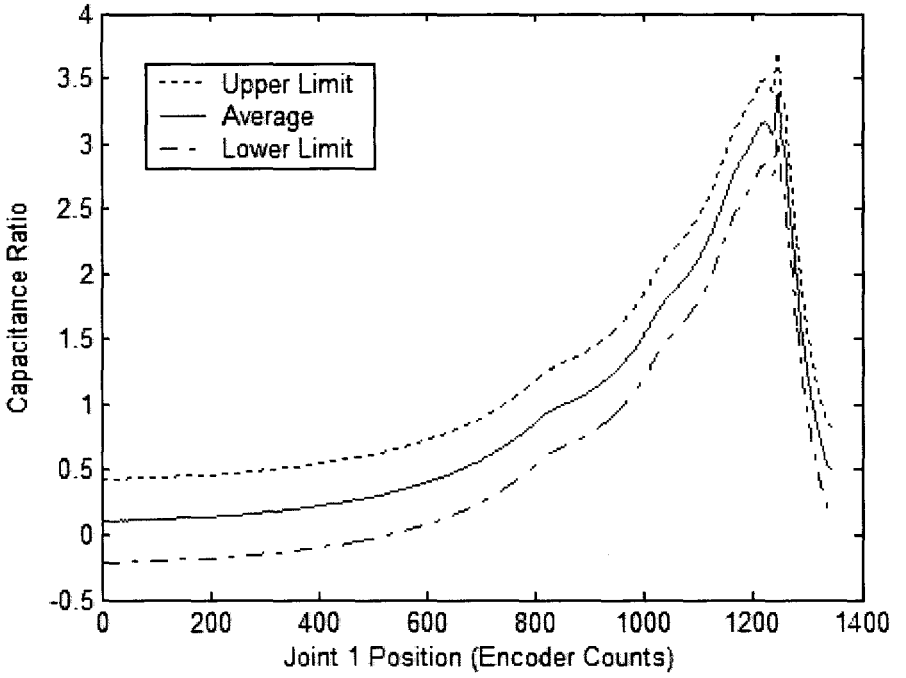

Figure 8-26: Limits with training done at a speed of 20

Based on this observed dependency, it is advisable that the training be done at or near the speed used for normal operation. The other issue that should be considered is that operating at higher speeds requires larger stopping distances at runtime. Larger limits on the other hand lead to a later detection of the abnormality further adding to the problem. The combination of the added momentum as well as the need for increased operational boundaries limits the maximum speed at which the supervised robots should operate. In case of the test F3 arm and the C-500 controller higher speeds lead to substantially longer reaction times before the controller would acknowledge the request and start to ramp down the speed. Such behaviour would further limit the collision avoidance performance.

8.7 Conclusion

The CAS was evaluated by conducting numerous experiments. It was shown that with the proposed operational boundaries, the CAS generated no false alarms and avoided potential collisions. While the 50-run training of the limits was recorded at only a F3 speed of 5, the minima and maxima of the capacitance signatures for 500 runs at speeds of 5 and 10 each were recorded and shown to be in agreement with these limits. The second phase of the testing process involved minute changes in the environment and the position of the obstructing robot to evaluate the sensitivity of the system. It is worth recalling that the testing was done in a flyby arrangement in which the electrodes were not aligned. It is evident from the physics of capacitance that this reduces the sensitivity and the practical cases with aligned electrodes will provide better sensitivity. Yet with this layout it was shown that with a 5mm motion of the second robot, the system could consistently detect the disturbance and would have stopped the robot. This was true for both the lower and upper bounds.

The last phase of the validation work was the testing of the full CAS. The runtime module was in total control of the robot and the results were visually inspected. After a one-cycle synchronisation of the runtime module and the robot sequence, the behaviour of the system was tested by moving R2. In addition to logging the data, the system provides feedback on the screen and an audible warning. Any violation of the limits immediately pauses the robot and generates a warning beep. The reaction-time was found to be mostly a function of the robot controller. All potential collisions were avoided using the CAS.

CHAPTER 9

Conclusion and Future Work

9.1 Summary

In this research, the application of capacitive sensing for robot arm collision avoidance for use in industrial environments was examined. After a look at the physics of the phenomenon, viable options for measurement were investigated. A selected number of analytical and numerical methods to estimate the mutual capacitance of two plates were discussed. The concept of capacitive signature of the robot's motions was introduced. It was established that for a given task and in a pre-defined environment, as in a production line workcell, the signature maintains a functional consistency. The notion of multiple electrode-pairs and its benefits in this application were also considered. The choice of electrical hardware and its performance were reviewed. The limitations of the hardware were empirically confirmed. The dynamic and common-mode range of this particular hardware were reviewed to achieve optimal operation. The collision avoidance method was based on monitoring the capacitance signature of the arms for a given task. The operational boundaries or the limits for normal operation were obtained using a non-parametric statistical approach. The collision avoidance runtime module sends a pause command whenever these limits are breached. The work also introduced an efficient software algorithm for the runtime module of the CAS. The

system was tested through rigorous testing and data logging. This included a large number of normal runs as well as cases with potential collisions. It was seen that the system is capable of confidently detecting deviations as small as 5mm and reacting accordingly. The system is capable of running at a sampling rate of 20ms with a single electrode-pair. The overall reaction-time of the system was dominated by the latency of the F3 robot used in the experiments.

9.2 Achievements

The primary achievements of this research work are as follows:

1) Comparison of the different methods for modeling mutual capacitance and their relevance to the robotic collision avoidance application.
2) A full range calibration of the chosen measurement chip through synthetic extension of the measurement range. By synthetic extension of the range, the calibration was achieved for the full range.
3) Development of the modular software and hardware for interfacing with the AD7746 Capacitance to Digital Converter chip. The software driver frees the programmer from the details of communication and low-level details of the chip.
4) Development of software for data logging with and without robot interaction. This facilitates unattended data logging of the test setup.
5) Identification of a method to generate the operational boundaries from a relatively small (*i.e.* less than 100) training process. This method is applicable to any robot task or environment.

6) Demonstration of the usability of the system in a typical robotic workcell. The system was evaluated for multiple unexpected conditions and its correct behaviour was demonstrated.

9.3 Recommendations and Future Work

Throughout this research and in background to the current work, a series of motivating issues were observed that leaves room for future studies. Some of which are as follows:

1) The method is fundamentally applicable to more than two robots. While this was not tested as a part of this thesis, further work could bring this to completion.
2) While only a single joint approach to the position of the robot was used, a multi-joint application leads to new challenges in computation of the arc length needed for data processing and runtime monitoring.
3) The intention of this research has been to recognise unsafe conditions and assert a pause. A system capable of suggesting corrective robot(s) action could minimise the possibility of deadlocks and should result in a more efficient use of time.
4) Prioritisation of the robots in the workcell would further improve the usability of the system. In other words, if in case of a foreseen danger, in certain cases it is preferable to allow the higher priority arm to proceed while stopping the secondary robots.

5) The current research implementation involves manual processing of the data in MATLAB. An end-user application is essential for industrial environments and wider use.

REFERENCES

[1] Duffy, N., Allan, D., Herd, J T., "Real-time collision avoidance system for multiple robots operating in shared work-space," IEEE Proceedings on Computers and Digital Techniques, vol. 136, no. 6, pp. 478-484, Nov 1989.

[2] Roach, J., Boaz, M., "Coordinating the motions of robot arms in a common workspace," IEEE Journal of Robotics and Automation, vol. 3, no. 5, pp. 437-444, Oct 1987

[3] Erlic, M., Jones, K., Lu, W.-S., "Hardware interface configuration for motion control of the PUMA-560 and the Mitsubishi RM-501 robots," IEEE Pacific Rim Conference on Communications, Computers and Signal Processing, vol. 1, no. 9-10 , pp. 266-269, May 1991.

[4] Ang, M H., Jr., Wei, L., Lim Ser Yong, "An industrial application of control of dynamic behavior of robots-a walk-through programmed welding robot," Proceedings of International Conference on Robotics and Automation, vol. 3, no. 9-10, pp. 2352-2357, 2000.

[5] Schutter, J. D., Torfs, D., Dutré, S., Bruyninckx, H., "Robot Force Control Experiments with an Actively Damped Compliant End Effector," Proceedings of 4th International Symposium on Experimental Robotics, 1995.

[6] Kavraki, L.E., Svestka, P., Latombe, J.-C., Overmars, M H., "Probabilistic roadmaps for path planning in high-dimensional configuration spaces," IEEE Transactions on Robotics and Automation, vol. 12, no. 4, pp. 566-580, Aug 1996.

[7] Balan, L., "Real-Time 3D Collision Avoidance Algorithm for Safe Human and Robot Coexistence," Ph.D. Thesis, McMaster University, Hamilton, Ontario, Canada, 2006.

[8] Lee, B., Chien, Y., "Time-varying obstacle avoidance for robot manipulators: Approaches and difficulties," Proceedings of IEEE International Conference on Robotics and Automation, vol. 4, pp. 1610-1615, Mar 1987

[9] Nakamura, T., Takamura, S., Asada, M., "Behaviour-based map representation for a sonar-based mobile robot by statistical methods," Proceedings of the 1996 IEEE/RSJ International Conference on Intelligent Robots and Systems , vol. 1, pp. 276-283, 4-8 Nov 1996.

[10] Cheung, E., Lumelsky, V., "Motion planning for robot arm manipulators with proximity sensing ," Proceedings of IEEE International Conference on Robotics and Automation, vol. 2, pp. 740-745, 24-29 Apr 1988.

[11] Lumelsky, V.J., Cheung, E., "Real-time collision avoidance in teleoperated whole-sensitive robot arm manipulators," IEEE Transactions on Man and Cybernetics Systems, vol. 23, no. 1, pp. 194-203, Jan/Feb 1993.

[12] Seraji, H., Steele R., Iviev R., " Sensor-based collision avoidance· Theory and Experiments ," Journal of Robotic Systems, vol. 13, no. 9, pp. 571-586, 1996.

[13] Gandhi, D., Cervera, E., "Sensor covering of a robot arm for collision avoidance," Proceedings of IEEE International Conference on Man and Cybernetics Systems, vol.5, pp. 4951-4955, 5-8 Oct. 2003.

[14] Heng, T.C.H., Kuno, Y., Shirai, Y., "Active sensor fusion for collision avoidance," Proceedings of the 1997 IEEE/RSJ International Conference on Intelligent Robots and Systems, vol. 3, pp. 1244-1249, 7-11 Sep 1997

[15] Morikawa, S., Senoo, T., Namiki, A., Ishikawa, M., "Realtime collision avoidance using a robot manipulator with light-weight small high-speed vision systems," IEEE International Conference on Robotics and Automation, pp. 794-799, 10-14 April 2007

[16] Jagiella, M., Fericean, S., "Miniaturized inductive sensors for industrial applications," Proceedings of IEEE on Sensors, vol. 2, pp. 771-778, 2002.

[17] Novak, J.L., Wiczer, J.J., "A high-resolution capacitive imaging sensor for manufacturing applications," Proceedings of IEEE International Conference on Robotics and Automation, vol. 3, pp. 2071-2078, 9-11 Apr 1991.

[18] Novak, J.L., Feddema, I.T., "A capacitance-based proximity sensor for whole arm obstacle avoidance," Proceedings of IEEE International Conference on Robotics and Automation, vol. 2, pp. 1307-1314, 12-14 May 1992.

[19] Ma, Y., "Sensor-based Real-time Collision Robot Avoidance", M.A.Sc. Thesis, McMaster University, Hamilton, Ontario, Canada, 2007

[20] Karlsson, N., Jarrhed, J.-O., "A capacitive sensor for the detection of humans in a robot cell," Proceedings of IEEE Instrumentation and Measurement Technology Conference, pp. 164-166, 18-20 May 1993.

[21] Cheung, E., Lumelsky, V., "Motion planning for robot arm manipulators with proximity sensing ," Proceedings of International Conference on Robotics and Automation, vol. 2, pp. 740-745, 24-29 Apr 1988.

[22] Boddy, C.L., Stobart, A., "Application of a hierarchical control structure in the implementation of a manipulator real-time collision avoidance system," Fifth International Conference on Advanced Robotics, vol. 2, pp. 1473-1476, 19-22 Jun 1991.

[23] Feddema, J T., Novak, J.L., "Whole arm obstacle avoidance for teleoperated robots," Proceedings of 1994 IEEE International Conference on Robotics and Automation, vol. 4, pp. 3303-3309, 8-13 May 1994.

[24] Xie, H.P., Patel, R.V., Kalaycioglu, S., Asmer, H., "Real-time collision avoidance for a redundant manipulator in an unstructured environment," Proceedings of IEEE/RSJ International Conference on Intelligent Robots and Systems, vol. 3, pp. 1925-1930, 13-17 Oct 1998.

[25] Xiang,Y, "The electrostatic capacitance of an inclined plate capacitor," Journal of Electrostatics, Vol. 64, Issue 1, pp. 29-34., January 2006

[26] Tipler, P.A., and Mosca, G, Physics for Scientists and Engineers, Volume 2B. Electrodynamics and Light, 5th ed. New York: W H. Freeman, July 2003.

[27] Freescale Semiconductor, Technical Data MC33794--Electric Field Imaging Device, Rev 9, Nov 2006.

[28] Analog Devices, AD7745/AD7746 Datasheet--24-Bit Capacitance-to-Digital Converter with Temperature Sensor, May 2005.

[29] Analog Devices, AD7152/AD7753 Datasheet--12-Bit Capacitance-to-Digital Converter, May 2008.

[30] Goddard Space Flight Center, National Aeronautics and Space Administration, "Capaciflector-based" Technology", April 11, 2005.

[31] Ansari, S.A., Baig, R., "A PC-based vibration analyzer for condition monitoring of process machinery," IEEE Transactions on Instrumentation and Measurement, vol. 47,

no. 2, pp. 378-383, Apr 1998.

[32] Bertone, G.A., Meiksin, Z.H., Carroll, N.L., "Noise analysis for the triaxial capacitive displacement transducer ," IEEE Transactions on Instrumentation and Measurement, vol. 39, no. 5, pp. 735-738, Oct 1990.

[33]Bertone, G.A., Meiksin, Z.H., Carroll, N.L., "Elimination of the anomalous humidity effect in precision capacitance based transducers," IEEE Transactions on Instrumentation and Measurement, vol. 40, no. 6, pp. 897-901, Dec 1991.

[34] Texas Instrument, Datasheet, "CD4067B, CD4097B Types Datasheet", June 2003,

[35]Jin Bao; Wang Shuguo; Yili Fu, "Sensor-based motion planning for robot manipulators in unknown environments," IEEE/RSJ International Conference on Intelligent Robots and Systems, pp. 199-204, 2-6 Aug. 2005.